

**MEMS Micro-Ribbons for Integrated Ground Plane
Microstrip Delay Line Phase Shifter**

By

Joe Yip

A Thesis

Submitted to the Faculty of Graduate Studies of the University of Manitoba
in Partial Fulfillment of the Requirements for the Degree of

Master of Science

Department of Electrical and Computer Engineering

University of Manitoba

Winnipeg, Manitoba, Canada

Copyright© 2008 by Joe Yip

ABSTRACT

A delay line phase shifter for the 30-70 GHz range is presented that uses an aluminum micro-ribbon array fabricated in the ground plane of a microstrip transmission line. Phase shift is achieved by changing the propagation velocity of an RF signal in the transmission line by controlling the effective permittivity of the substrate. This is done by actuating the micro-ribbons away from the substrate. This phase shifter has the benefits of analog phase shifts and high Figure of Merit. Simulations were done to model the micro-ribbon deflections, transmission line performance and phase shift. Arrays of 5, 10, and 20 μm wide micro-ribbons were fabricated and tested. At 40.80 GHz, the 20 μm wide micro-ribbons had a measured phase shift of 33° with an actuation voltage of 120 V. The corresponding Figure of Merit was a negative value indicating that there was no line loss due to ribbon deflection.

ACKNOWLEDGEMENTS

I would like to thank my advisor, Dr. Cyrus Shafai, for the years of funding and valuable discussion and encouragement that allowed me to complete this thesis. I also would like to thank all the lab technicians that kept the NSFL up and running.

I want to thank all my grad school friends, the ones that left before me and the ones that I'm leaving behind. Your friendship was greatly appreciated Jeremy Johnson, Kwan-yu Lai, Kar Mun Cheng, Alfred Lip and Jane Cao. Long live the LLS and DLS meetings. May they never come to an end.

I want to thank my friends and especially the PM group: Renzie Gonzales, Nelson Chan, Jennifer Chan, Juanita Chan, Greg Chan, Wilfred Wong, Jay Dong, Joe Ding, Hazel Cheng, Robert Yeung, and Andy Ng. Thanks for all the meals that we've shared together, the games of settlers, and beans. You guys have been great friends through out the years.

Last, but not least, I want to thank my family for constantly asking me when I will finally finish and for loving me from the beginning.

TABLE OF CONTENTS

Abstract	ii
Acknowledgements	iii
Table of Contents	iv
List of Tables	vi
List of Figures	viii
List of Copyrighted Material for Which Permission was Obtained	xiii
List of Acronyms	xiv
CHAPTER 1	1
Introduction	1
1.1 Motivation	1
1.2 Concept	3
1.3 Thesis Objectives	6
1.4 Organization of the Thesis	7
CHAPTER 2	8
MEMS and Micromachining	8
2.1 MEMS	8
2.2 Micromachining Techniques	9
2.2.1 <i>Method of Material Deposition: Sputtering</i>	9
2.2.2 <i>Lithography</i>	10
2.2.3 <i>Etching Methods</i>	12
CHAPTER 3	14
Background	14
3.1 Overview	14
3.2 Electrostatic Actuators	15
3.3 MEMS Phase Shifters	16
3.3.1 <i>Delay/switch Line Phase Shifters</i>	16
3.3.2 <i>Load line/distributed Line Phase Shifters</i>	19
3.3.3 <i>Defected Ground Plane Phase Shifters</i>	21
CHAPTER 4	24
Design and Modeling of Micro-Ribbons	24
4.1 Overview	24
4.2 Simulation Setup	25
4.3 Straight Micro-Ribbons	30
4.4 The Number of Segments in the Micro-ribbon	33
4.4.1 <i>Micro-ribbons with straight segments at the jogs</i>	37
4.5 Varying Jog Angles	38
4.6 Simulation of Different Complex Designs	42
4.7 Varying Separation Distances between Micro-ribbons	45
4.8 Summary	47
CHAPTER 5	49
Fabrication	49
5.1 Overview	49
5.2 Fabrication Geometries	50

5.3	General Fabrication.....	50
5.3.1	<i>Fabrication of the RF Substrate</i>	50
5.3.2	<i>Fabrication of the Transmission Line</i>	52
5.3.3	<i>Fabrication of the Micro-Ribbon Array</i>	54
5.4	Investigation of the Dry Release Process.....	56
5.4.1	<i>Dry etch process test mask</i>	58
5.5	XeF ₂ Gas Etch.....	59
5.6	Plasma Gas Etch.....	60
5.6.1	<i>CF₄ Gas Etch</i>	62
5.6.2	<i>SF₆ Gas Etch</i>	63
5.7	Fabricated Micro-ribbons.....	64
5.8	Summary.....	69
CHAPTER 6.....		70
Micro-ribbon Deflection: Testing and Model Verification.....		70
6.1	Overview.....	70
6.2	Deflection Test Setup.....	71
6.3	Deflection Measurements.....	72
6.4	Simulated Deflections.....	73
6.5	Comparison of Simulated and Measured Results.....	75
6.6	Thermal Expansion Effects on the Micro-Ribbon Array.....	79
6.7	Summary.....	82
CHAPTER 7.....		83
Phase Shift Testing and Model Verification.....		83
7.1	Overview.....	83
7.2	RF Background.....	84
7.3	HFSS Simulations Setup.....	85
7.4	Transmission Line Design.....	86
7.4.1	<i>Transmission Line of 37 Ω</i>	89
7.4.2	<i>Transmission Line of 50 Ω</i>	93
7.5	Measurements for the 20 μm wide Micro-Ribbons.....	97
7.6	Measurements for the 5 μm and 10 μm wide Micro-Ribbons.....	103
7.6.1	<i>5 μm wide micro-ribbons</i>	104
7.6.2	<i>10 μm wide micro-ribbons</i>	109
7.6.3	<i>10 μm wide micro-ribbon reproducibility of measurements testing</i>	114
7.7	Summary.....	115
CHAPTER 8.....		117
Conclusion and Future Work.....		117
8.1	Conclusion.....	117
8.2	Future Work and Recommendations.....	119
References.....		120
Appendix A – COMSOL Procedure.....		122
Appendix B – COMSOL Simulations.....		131
Appendix C – Dry Etch Tests Raw Data.....		133
Appendix D – HFSS Simulations.....		138
Appendix E – Phase Shift Measurement Data.....		143

LIST OF TABLES

Table 4-1: Boundary conditions for the electrostatic sub-module.....	26
Table 4-2: Boundary conditions for the mechanical-plane stress sub-module.....	26
Table 4-3: Bounding box dimensions in a typical simulation.	29
Table 4-4: Dimensions of the straight beams simulated.....	30
Table 4-5: Deflection and force on Beam 1 with voltages ranging from 1-6 V.	31
Table 4-6: Deflection and force on Beam 1 with voltages ranging from 5-30 V.	31
Table 4-7: Deflection and force on Beam 2 with voltages ranging from 5-30 V.	31
Table 4-8: Deflection and force on Beam 1 with voltages ranging from 5-30 V.	32
Table 4-9: Simulated spring constant for micro-ribbons of differing number of segments.....	34
Table 4-10: Simulated spring constant for 3 mm long and 1 μm thick aluminum micro-ribbons of differing number of segments with uniform pressure resulting in an electrostatic force = 1×10^{-7} N.	36
Table 4-11: Simulated spring constant for 3 mm long and 1 μm thick aluminum micro-ribbons of differing number of segments with uniform pressure resulting in an electrostatic force = 5×10^{-7} N.....	36
Table 4-12: Volume of air present above a micro-ribbon for various ribbon geometries when deflected by a 14 V potential.	45
Table 4-13: Simulated electrostatic force between a 3 mm long and 1 μm thick micro-ribbon and a pull-down electrode as a function of inter-ribbon spacing. The electrode is 100 μm from the ribbon and is biased to 50 V.....	46
Table 4-14: 2D simulation showing the force increase with increasing separation distance between 3 mm long and 1 μm thick micro-ribbons. Ribbons are located 100 μm from the pull-down electrode biased to 50 V.	47
Table 5-1: Aluminum sputtering recipe.....	53
Table 5-2: Lithography process parameters.....	54
Table 5-3: Plasma etch parameters for dry release.	56
Table 5-4: Plasma etch parameters for test pattern sample.....	61
Table 5-5: Plasma etch recipes for CF_4	62
Table 5-6: Plasma etch CF_4 results.....	62
Table 5-7: Plasma etch recipes for SF_6	63
Table 5-8: Plasma etch SF_6 results.....	63
Table 6-1: Deflection vs. voltage measurements for the 20 μm ribbon array. The result for the ribbons at the left and right side of the array are shown.....	73
Table 6-2: Simulated behaviour of 20 μm wide and 1 μm thick aluminum micro- ribbons with the “large deformation” option turned off in COMSOL.....	74
Table 6-3: Simulated behaviour of 20 μm wide and 1 μm thick aluminum micro- ribbons with the “large deformation” option turned on in COMSOL.	75
Table 6-4: Calculated resonant frequency for the 20 μm wide, 3 mm long, and 1 μm thick aluminum micro-ribbon at different deflections.	79
Table 6-5: Thermal expansion deflections for 3 mm long, 1 μm thick aluminum micro-ribbon assuming all deflection in the z direction.....	81

Table 7-1: Performance measurements for 20 μm wide micro-ribbons set 1 below a 37 Ω , 3.5 cm long transmission line.....	100
Table 7-2: Performance measurements for 20 μm wide micro-ribbons set 2 below a 37 Ω , 3.5 cm long transmission line.....	100
Table 7-3: Figure of merit for 20 μm wide micro-ribbons set 1 for phase shifts from a 120 V actuation voltage.....	102
Table 7-4: Figure of merit for 20 μm wide micro-ribbons set 2 for phase shifts from a 120 V actuation voltage.....	103
Table B-1: Simulations done investigating longer micro-ribbons and different thicknesses.	132
Table C-1: CF_4 etch recipes.	133
Table C-2: CF_4 oxide thickness and oxide etch rate.....	133
Table C-3: CF_4 under cut and under cut rate.	134
Table C-4: CF_4 silicon etch depth and silicon etch rate.....	134
Table C-5: Overall Rates for the CF_4 recipes.	134
Table C-6: SF_6 Etch Recipes and the raw data.	135

LIST OF FIGURES

Fig. 1.1: Diagram of a transmission line and a transmission line with a phase shifter. The phase shifter delays the signal by θ degrees.	2
Fig. 1.2: A 2x1 phased array antenna illustrating how the addition of a phase shifter on one of the lines can be used to cause constructive and destructive interference that allows for beam steering.....	3
Fig. 1.3: Illustration of the micro-ribbon array concept.....	3
Fig. 1.4: Top view of the phase shifter showing the orientation of the transmission line over micro-ribbons.....	4
Fig. 1.5: Photograph of a micro-ribbon array that spans a length of 3 mm.....	4
Fig. 1.6: Schematic showing the thickness of the stacked dielectrics in the phase shifter setup.	5
Fig. 1.7: Plot of the effective permittivity of stacked dielectrics (silicon and air) ranging from 0% - 100% air to silicon ratio.	6
Fig. 2.1: Schematic of a sputter system showing the parallel-plate reaction chamber, and the target and wafer positions.....	10
Fig. 2.2: Flow chart of a typical lithography process.	11
Fig. 2.3: Etch profiles for different types of etches. (a) Isotropic etch typical of wet etch processes, (b) anisotropic KOH etch profile due to etching of a <100> silicon wafer, (c) vertical anisotropic etch possible in RIE etch systems.	12
Fig. 3.1: Delay line phase shifter that uses micro-switches to re-route the RF signal to different transmission line segments [14].....	17
Fig. 3.2: Photograph of a 5-bit phase shifter with a die size of 7 mm x 4 mm [17].	18
Fig. 3.3: SEM photograph of a MEMS bridge in a DMTL [20].....	20
Fig. 3.4: Photograph of a 3-bit W-band DMTL [19].	21
Fig. 3.5: Schematic of the corrugated membrane based phase shifter of [5].....	22
Fig. 3.6: Photograph of corrugated membrane used in the reconfigurable ground plane of [5].	22
Fig. 4.1: Illustration of the COMSOL simulation bounding box.....	27
Fig. 4.2: Illustration of the fringing fields on a micro-ribbon, showing the field extension beyond the ribbon width.	27
Fig. 4.3: Illustration of the simulation setup with adjacent rigid grounds.	28
Fig. 4.4: Graph showing the effects of having the option “Large Deformation” enabled. The spring constant of a beam increases as the beam is deflected.	33
Fig. 4.5: Top view of geometries of micro-ribbons at 22.5° angle to the longitudinal with 2, 3 and 4 segments. Each micro-ribbon spanned a length of 3 mm. The actual length of the micro-ribbons varied.....	34
Fig. 4.6: Simulation of ribbon deflection as a function of voltage for different numbers of segments with the “large deformation” option enabled.	35
Fig. 4.7: Geometries of 4 segment micro-ribbons with and without straight segments at the jogs.	37

Fig. 4.8: Simulated deflection as a function of voltage for 4 segment micro-ribbons with and without straight segments at the jogs. Both 22.5° and 45° geometries are shown. The two 22.5° lines overlap each other.	38
Fig. 4.9: Illustration of the jog angle.	38
Fig. 4.10: Illustration of the 4-segment geometries at 22.5°, 45°, and 67.5° with each segment being 500 μm in length.	39
Fig. 4.11: Simulated deflection as a function of voltage for the micro-ribbons in Figure 4.10 for jog angles of 22.5°, 45° and 67.5°.	40
Fig. 4.12: Simulated resonant frequency vs. jog angle for a 4 segment beam.	41
Fig. 4.13: Simulated spring constant vs. jog angle for a 4 segment beam.	41
Fig. 4.14: Illustrations of the more complex geometries simulated.	43
Fig. 4.15: Simulated deflection as a function of voltage of the various micro-ribbon geometries of Fig. 4.14.	44
Fig. 4.16: Schematic of the 3D simulation of the micro-ribbon with adjacent rigid grounds used to determine the effect of fringing capacitance on the electrostatic force.	45
Fig. 4.17: Schematic of the 2D simulation of 11 micro-ribbons used to model the effect of the fringing capacitance on the electrostatic force in an array situation.	46
Fig. 4.18: Simulated electrostatic force as a function of micro-ribbon separation distance for 3 mm long and 1 μm thick micro-ribbon. Ribbons are located 100 μm from the pull-down electrode biased to 50 V.	47
Fig. 5.1: Fabrication steps to attain a rectangular wafer from a round wafer. (a) original wafer. (b) spin on photoresist and do lithography. (c) etch the silicon oxide. (d) Etch in KOH solution to achieve the “V” grooves.	51
Fig. 5.2: Cleaved wafer with top and bottom intact to prevent shorting of top and bottom metal deposited in subsequent sputter deposition steps.	52
Fig. 5.3: Fabrication of the transmission line and the micro-ribbon array. (a) aluminum for the transmission is deposited and patterned. (b) aluminum for the micro-ribbons is sputtered and patterned. (c) the micro-ribbons are released using a gas etch process.	53
Fig. 5.4: Photograph showing unetched portions in the micro-ribbon array with 10 μm wide ribbons and 10 μm spacing.	55
Fig. 5.5: Diagram illustrating vertical etch, lateral etch and the peak that forms underneath a micro-ribbon in an isotropic etch process.	57
Fig. 5.6: Photo of a peak forming underneath a micro-ribbon. It can be clearly seen that the center micro-ribbon is being released and is bending over the peak.	58
Fig. 5.7: Test pattern for testing dry release recipes.	59
Fig. 5.8: Diagram showing that in a XeF ₂ gas etch process more gas atoms can approach from the side resulting in trenching.	60
Fig. 5.9: Profile of an etched feature in an XeF ₂ gas etched wafer. An etch profile that is deeper on the edges due to trenching is visible.	60
Fig. 5.10: Etch profile for plasma etched test wafer. The plasma gas etch process is a more uniform process than XeF ₂ gas etching, resulting in an etch profile that is more uniform in depth.	62

Fig. 5.11: Geometry of the 20 μm wide fabricated micro-ribbon.....	64
Fig. 5.12: Geometries of the 5 μm and 10 μm micro-ribbons.	65
Fig. 5.13: Photograph of 10 μm wide micro-ribbons with 10 μm spacing. Released ribbons are out of plane and no longer in focus.....	66
Fig. 5.14: Photographs of the 5 μm wide micro-ribbons with 10 μm spacing for the “Both Up” geometry showing overlapping micro-ribbons. (a) at 50x and (b) 100x.	67
Fig. 5.15: Photographs of the “8 Segment” geometries. (a) 5 μm wide micro- ribbons with 10 μm spacing at 50x. (b) 5 μm wide micro-ribbons with 5 μm spacing at 100x.	68
Fig. 6.1: Diagram of the deflection measurement setup showing the placement of the microscope, micro-ribbon array and the glass with a conducting surface used as the pull-down electrode.....	72
Fig. 6.2: Geometry of the simulated 20 μm wide micro-ribbon.	73
Fig. 6.3: Graph showing the simulated and measured deflections of the 20 μm ribbon array showing both the left and right side measurements with error bars due to the microscope micrometer.....	75
Fig. 6.4: Simulated force required for a specific deflection at the center for the 20 μm wide micro-ribbon fabricated from 1 μm thick aluminum.	77
Fig. 6.5: Simulated force as a function of actuation voltage for the 20 μm wide micro-ribbons at varying ground heights.	78
Fig. 6.6: Illustration of worst case deflection in z direction due to thermal expansion of the micro-ribbon.	80
Fig. 6.7: Deflection caused by thermal expansion of a 3 mm long, 1 μm thick aluminum micro-ribbon assuming all deflection is in the z direction.....	81
Fig. 7.1: A generic 2-port RF network indicating the input and output port voltages.	84
Fig. 7.2: Simulation geometry for the flat membranes in HFSS.	86
Fig. 7.3: Line impedance vs. deflection for a 37 Ω transmission line for the case of having no initial air gap and 20 μm initial air gap due to the ribbon release process [22].	87
Fig. 7.4: HFSS simulation results showing the expected phase shift vs. deflection for a fabrication process with no initial air gap and an initial air gap of 20 μm at 50 GHz for a 3 mm long membrane.	88
Fig. 7.5: Simulated S_{11} magnitude for a 37 Ω line for a 6 mm long line and 3 mm long membrane.	89
Fig. 7.6: Simulated S_{21} magnitude for a 37 Ω line for a 6 mm long line and 3 mm long membrane.	90
Fig. 7.7: S_{11} magnitude for a 37 Ω line at 50 GHz. Note how with membrane deflection, the line impedance increases and is matched at 50 Ω around 5 μm deflection.	91
Fig. 7.8: Simulated differential S_{21} phase for a 37 Ω line for different air gaps vs. deflection at 50 GHz.	92
Fig. 7.9: Simulated S_{21} magnitude for a 37 Ω line for different air gaps vs. deflection at 50 GHz.	92

Fig. 7.10: Simulated S_{11} magnitude for a 50Ω line with no initial air gap and no deflection.	93
Fig. 7.11: Simulated S_{21} magnitude for a 50Ω line with no initial air gap and no deflection.	94
Fig. 7.12: Simulated S_{11} magnitude for a 50Ω line at 50 GHz. Note how with membrane deflection, the line impedance increases and is no longer matched.	95
Fig. 7.13: Simulated differential S_{21} phase for a 50Ω line for different air gaps vs. deflection at 50 GHz.	96
Fig. 7.14: Simulated S_{21} magnitude for a 50Ω line for different air gaps vs. deflection at 50 GHz.	96
Fig. 7.15: Simulated differential S_{21} phase for a 50Ω line with an initial air gap of $5 \mu\text{m}$ for different frequencies.	97
Fig. 7.16: Photograph of the phase shifter in the test fixture with V-connectors. The pull down electrode can be seen running vertically underneath the phase shifter which is propped up by foam.	98
Fig. 7.17: Diagram of the pull-down electrode with the tape as an insulator. Two layers of 3M scotch tape is used to form the $120 \mu\text{m}$ gap between the micro-ribbon array and 1 layer is used as the insulator.	99
Fig. 7.18: Measured differential phase as a function of voltage for the $20 \mu\text{m}$ wide micro-ribbon array (set 2) underneath a 37Ω transmission line at 49.65 GHz.	101
Fig. 7.19: (a) Measured S_{21} phase shift, (b) S_{21} magnitude for $5 \mu\text{m}$ wide micro-ribbons with $5 \mu\text{m}$ spacing in the “8 Segment” geometry.	105
Fig. 7.20: (a) Measured S_{21} phase shift, (b) S_{21} magnitude for $5 \mu\text{m}$ wide micro-ribbons with $10 \mu\text{m}$ spacing in the “8 Segment” geometry.	106
Fig. 7.21: Comparison of measured phase shift results for micro-ribbon arrays with ribbons $5 \mu\text{m}$ in width with two different ribbon separation distances.	108
Fig. 7.22: Photographs of the $5 \mu\text{m}$ wide micro-ribbons after phase shift tests. It is clear that many micro-ribbons were damaged in the testing process.	109
Fig. 7.23: (a) Measured S_{21} phase shift, (b) S_{21} magnitude for $10 \mu\text{m}$ wide micro-ribbons with $5 \mu\text{m}$ spacing in the “8 Segment” geometry.	110
Fig. 7.24: (a) Measured S_{21} phase shift, (b) S_{21} magnitude for $10 \mu\text{m}$ wide micro-ribbons with $10 \mu\text{m}$ spacing in the “8 Segment” geometry.	111
Fig. 7.25: Photographs of the $10 \mu\text{m}$ wide micro-ribbons after phase shift tests. (a) $5 \mu\text{m}$ spacing, some micro-ribbons do seem to have distorted, (b) $10 \mu\text{m}$ spacing, ribbons seem to all be in good shape.	112
Fig. 7.26: Comparison of measured phase shift results for micro-ribbon arrays with ribbons $10 \mu\text{m}$ in width with two different ribbon separation distances.	113
Fig. 7.27: Reproducibility of measurement experiment done on the $10 \mu\text{m}$ wide micro-ribbons with $5 \mu\text{m}$ spacing actuating the ribbons from 0 V, 150 V, 0 V, 0 V, 150 V, and 0 V.	114

Fig. 7.28: Reproducibility of measurement experiment done on the 10 μm wide micro-ribbons with 10 μm spacing actuating the ribbons from 0 V, 150 V, 0 V, 150 V, and 0 V.	115
Fig. D.1: Simulated 30 Ω transmission line S_{11}	138
Fig. D.2: Simulated 30 Ω transmission line S_{11} for different deflections at 50 GHz.	139
Fig. D.3: Simulated 30 Ω transmission line differential S_{21} phase for different air gaps.	140
Fig. D.4: Simulated 30 Ω transmission line differential S_{21} phase for a 5 μm initial air gap for different deflections for different frequencies.....	140
Fig. D.5: Simulated S_{21} for an initial air gap of 5 μm for different frequencies vs. deflection.....	141
Fig. D.6: Simulated S_{11} for an initial air gap of 5 μm for different frequencies vs. deflection.....	141
Fig. D.7: Simulated S_{21} differential phase for an initial air gap of 5 μm for different frequencies vs. deflection.....	142
Fig. E.1: Measured return loss (S_{11}), insertion loss (S_{21}) for a reference transmission line with no micro-ribbon array.	143
Fig. E.2: Set1 - The measured return loss (S_{11}), insertion loss (S_{21}) and insertion phase (S_{21}) of the single membrane phase shifter with the electrostatic actuation at the electrode from (a) 0 V, (b) 30 V, (c) 40 V, (d) 50 V, (e) 60 V, (f) 70 V, (g) 80 V, (h) 90 V, (i) 100 V, (j) 110 V, (k) 120 v, and (l) Reversed 0 V cases.....	150
Fig. E.3: Set2 - The measured return loss (S_{11}), insertion loss (S_{21}) and insertion phase (S_{21}) of the single membrane phase shifter with the electrostatic actuation at the electrode from (a) 0 V, (b) 30 V, (c) 40 V, (d) 50 V, (e) 60 V, (f) 70 V, (g) 80 V, (h) 90 V, (i) 100 V, (j) 110 V, (k) 120 v, and (l) Reversed 0 V cases.....	156

**LIST OF COPYRIGHTED MATERIAL FOR WHICH PERMISSION WAS
OBTAINED**

Image of a delay line phase shifter taken from:
Pillans, B., Eshelman, S., Malczewski, A., Ehmke, J., Goldsmith, C.:
“Ka-band RF MEMS phase shifters” Microwave and Guided Wave
Letters, IEEE, Vol. 9, Issue 12, Dec. 1999, pp. 520 – 522.....17

Image of a delay line phase shifter taken from:
Jian, Z., Yuanwei, Y., Le, L., Chen, C., Yong, Z., and Naibin, Y.:
“A 3-port MEMS switch for MEMS Phase Shifter Application”,
Proceedings of 1st IEEE International Conference on Nano/Micro
Engineered and Molecular Systems, January 18-21, 2006, Zhuhai China,
pp. 611-614.....18

Image of a distributed MEMS phase shifter taken from:
Qing, J., Shi, Y., Li, W., Lai, Z., Zhu, Z., and Xin, P.: “Ka-band
Distributed MEMS Phase Shifters on Silicon Using AlSi Suspended
Membrane”, Journal of Microelectromechanical Systems, Vol. 13,
No. 3, June 2004, pp. 542-549.....20

Image of a distributed MEMS phase shifter taken from:
Hung, J.-J., Dussopt, L., Rebeiz, G.M.: “Distributed 2- and 3-bit W-band
MEMS Phase Shifters on Glass Substrates”, IEEE Transactions on
Microwave Theory and Techniques, Vol. 52, No. 2, February 2004,
pp. 600-606.....21

Images of a corrugated membrane and reconfigurable ground plane taken from:
Shafai, C., Sharma, S.K., Shafai, L., and Chrusch, D.D.: “Microstrip Phase
Shifter Using Ground-Plane Reconfiguration”, IEEE Transactions on
Microwave Theory and Techniques, Vol. 52, No. 1, January 2004,
pp. 144-153.....22

LIST OF ACRONYMS

COMSOL – FEM program

CVD – Chemical Vapour Deposition

DMTL – Distributed MEMS transmission line

FEM – Finite element modeling

FET – Field Effect Transistor

FOM – Figure of Merit

HFSS – High Frequency Structure Simulator

IC – Integrated circuits

ITO – Indium Tin Oxide

MEMS – Micro-electro-mechanical systems

RF – Radio frequency

RIE – Reactive Ion Etching

sccm – standard cubic centimeter per minute

UV – Ultraviolet light

VNA – Vector Network Analyzer

CHAPTER 1

INTRODUCTION

1.1 Motivation

Phase shifters are important components in large-phased array antenna systems used for beam steering applications [1]. Modern phase shifters are mainly based on p-i-n diodes, field emitting transistors (FET) and ferromagnetic materials. However, as the applications move up in frequency (GHz), the insertion loss in the current systems becomes more significant [2]. In recent years, microelectromechanical-based (MEMS) solutions have been developed and presented [3]. These phase shifters are usually based on FET designs. However, instead of utilizing FETs for the switches, researchers have used MEMS switches. Some of these devices are discussed in Chapter 3.

A phase shifter is a component that can be inserted in series with a transmission line in order to obtain a phase shift in the signal as can be seen in Figure 1.1.

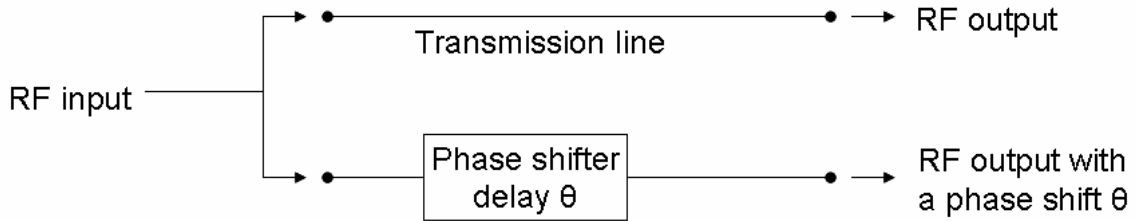


Fig. 1.1: Diagram of a transmission line and a transmission line with a phase shifter. The phase shifter delays the signal by θ degrees.

As shown in Figure 1.1, with the addition of a phase shifter in the transmission line, the output signal of the system at the reference plane is the original signal with a phase shift.

The ability to obtain a phase shift is important in large-phased array antenna systems. Figure 1.2 shows a simple 2x1 array antenna system. By controlling the phase of the signal on one of the antennas, it is possible to use constructive and destructive interference to create a focused beam. The amount of phase shift required for a phase shifter in a beam steering application depends on the application in question [1]. For instance, a satellite system would only need to be able to adjust the direction of the beam by a few degrees to maintain its directionality. However, a missile tracking system on a naval ship would need to be able to track the whole sky so a phase shifter that allows for 360° of phase shift would be required [2].

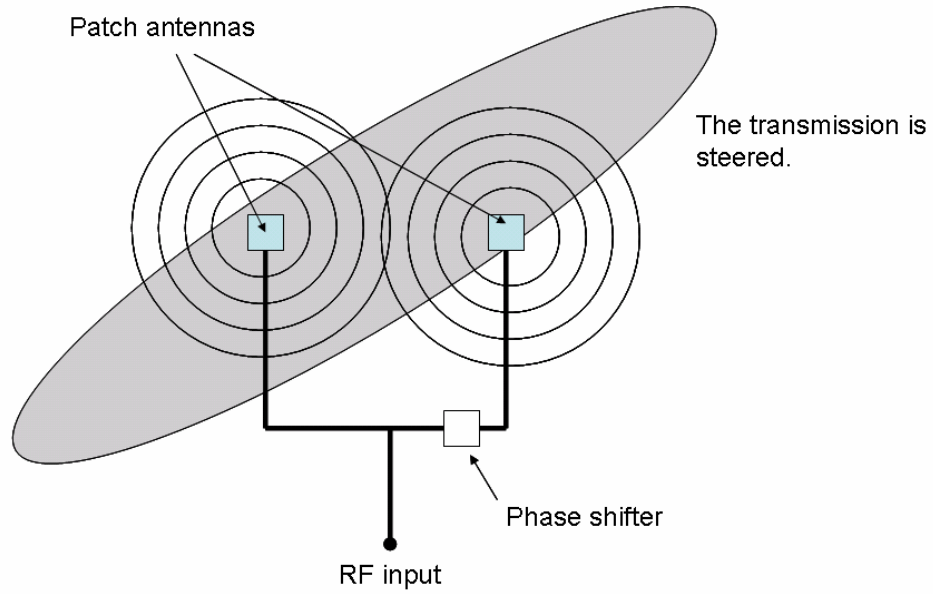


Fig. 1.2: A 2x1 phased array antenna illustrating how the addition of a phase shifter on one of the lines can be used to cause constructive and destructive interference that allows for beam steering.

1.2 Concept

In this thesis, a microstrip delay line phase shifter is described, which uses conducting flexible aluminum micro-ribbons as a means of bridging a ground plane slot.

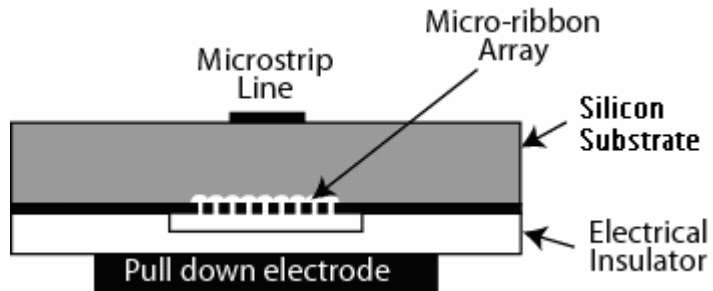


Fig. 1.3: Illustration of the micro-ribbon array concept.

Figure 1.3 illustrates the concept with the transmission line fabricated running parallel to the ribbon-shortened ground plane slot. A pull-down electrode placed below the ribbons is used to deflect the micro-ribbons away from the radio frequency (RF) substrate, introducing a controllable air gap between the ribbons and the RF substrate. This in turn controls the effective dielectric constant of the substrate in the micro-ribbon region, and so introduces a phase shift between the input and output signals. Figure 1.4 illustrates the orientation of the transmission line and the micro-ribbon array. Figure 1.5 is a photograph of a micro-ribbon array.



Fig. 1.4: Top view of the phase shifter showing the orientation of the transmission line over micro-ribbons.

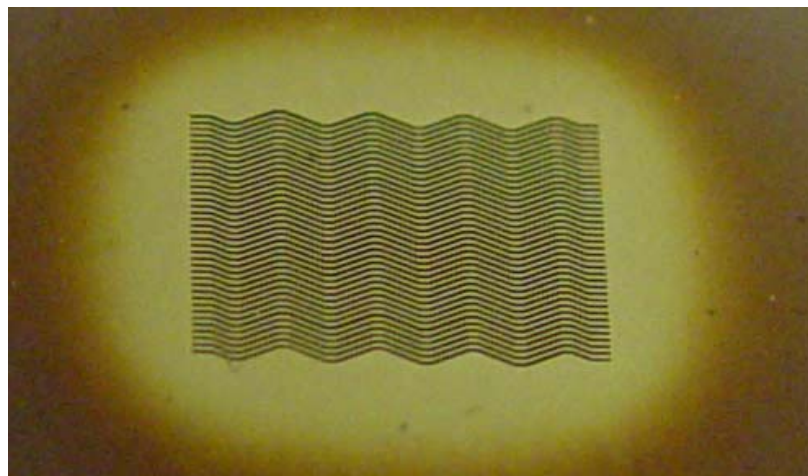


Fig. 1.5: Photograph of a micro-ribbon array that spans a length of 3 mm.

The phase velocity of an electromagnetic wave in a microstrip line is given by:

$$velocity = \frac{1}{\sqrt{\epsilon_r \epsilon_0 \mu_r \mu_0}} \quad (1.1)$$

where μ_r is the permeability of the substrate ($\mu_r = 1$ for non-magnetic materials), and $\epsilon_r = \epsilon_{eff}$ is the effective permittivity of the dielectrics [4]. In this case, the effective permittivity is a function of the thickness of the stacked air gap (d_2) and silicon (d_1) as is seen in Figure 1.6.

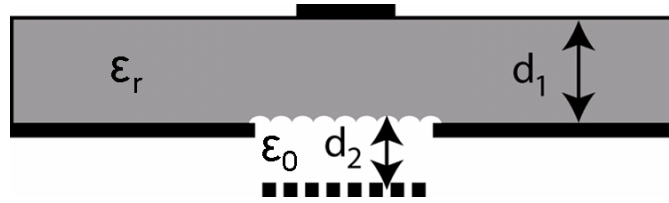


Fig. 1.6: Schematic showing the thickness of the stacked dielectrics in the phase shifter setup.

The phase shift occurs because the permittivity of the region between the transmission line and ground plane is being changed as the air gap is introduced. The effective permittivity ϵ_{eff} can be derived approximately from adding the dielectric capacitances in series:

$$\epsilon_{eff} = \frac{\epsilon_r \epsilon_0 (d_1 + d_2)}{\epsilon_r d_2 + \epsilon_0 d_1} \quad (1.2)$$

where ϵ_r and d_1 are the permittivity and the thickness of the silicon, and ϵ_0 and d_2 are the permittivity and the thickness of the air gap, respectively. Figure 1.7 shows the effective permittivity for a stacked dielectric of silicon and air as a function of the fraction of air in

the total thickness of the stacked dielectric. It should be noted that the initial introduction of air into the stacked dielectrics is significant because it introduces the largest gradient change in the effective permittivity and thus it is where the largest gradient change in phase shift occurs.

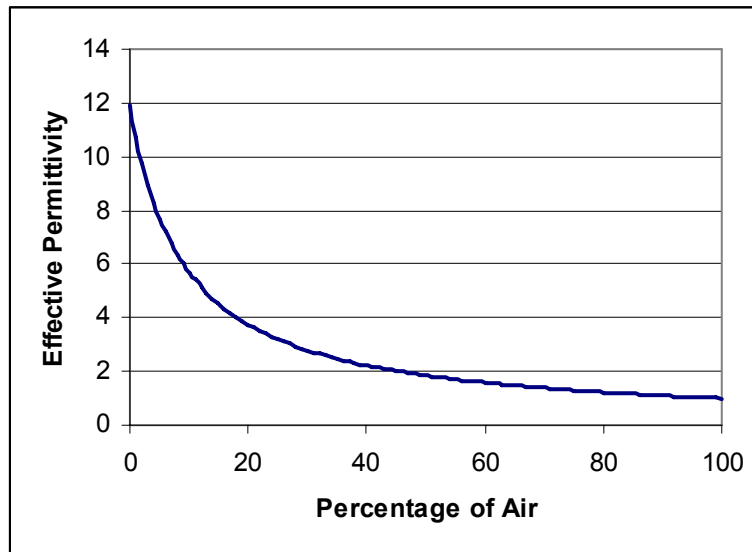


Fig. 1.7: Plot of the effective permittivity of stacked dielectrics (silicon and air) ranging from 0% - 100% air to silicon ratio.

1.3 Thesis Objectives

The first goal of this phase shifter project was to have a simple fabrication process. This means limiting the number of masks required to create the device. The second goal of the phase shifter design was to reduce the pull-down voltage required in the electrostatic actuation in comparison to a previous design by Shafai [5] discussed in section 3.3.3. Lastly, the phase shifter should be capable of analog phase shifts.

The fabrication of this phase shifter was done entirely in the Nanosystems Fabrication Laboratory (NSFL) located at the University of Manitoba. Through this

process, my goal was to gain experience in a nanosystems fabrication laboratory as well as learn to use simulation tools in order to design and characterize the phase shifter.

1.4 Organization of the Thesis

Chapter 2 is a brief overview of MEMS and micromachining techniques. Applicable material deposition and etching techniques are also discussed. In Chapter 3, the theory for electrostatic actuators and MEMS-based phase shifters are presented. Examples of delay line and distributed line phase shifters are also presented.

Chapter 4 is where the design and modeling of the micro-ribbons is presented. This chapter focuses on the simulations done in a program called COMSOLTM [6] in order to finalize the micro-ribbon geometry. In Chapter 5, the fabrication of the micro-ribbons is discussed. This includes the general fabrication of the overall system as well as a more focused discussion of the fine-tuning of the dry release process which involved different plasma etch recipes. In Chapter 6, the deflection testing of the micro-ribbon is discussed, and the results are compared to the results obtained through the simulations. Chapter 7 contains the phase shift simulations done in HFSSTM [7] and the actual phase shift measurements. Finally, in Chapter 8, the conclusions of this work are discussed and future work and recommendations are also presented.

CHAPTER 2

MEMS AND MICROMACHINING

2.1 MEMS

Micro-electro-mechanical systems (MEMS) is a field in which micro-mechanical structures are fabricated typically using integrated circuit (IC) fabrication processes. By using IC fabrication techniques, researchers have been able to build small, accurate mechanical structures that can be built on the same chip as their electrical control/sensing components. Specific MEMS devices will be presented in Chapter 3.

2.2 Micromachining Techniques

Some micromachining techniques will be explained briefly here because they are relevant to the fabrication process used in this thesis. Readers unfamiliar with micromachining techniques are directed to [8] for a broad background of MEMS techniques and devices.

2.2.1 Method of Material Deposition: Sputtering

Sputtering was the only deposition technique used in this work, although there are many different techniques to deposit materials in the field of MEMS, such as chemical vapour deposition (CVD), thermal evaporation, and electroplating.

Sputtering is a method of depositing material onto a wafer where a target, usually a round disc of the desired material to be deposited, is located in proximity to the substrate inside a parallel-plate plasma reactor chamber [9] (Fig. 2.1). The chamber is then evacuated of the ambient air and a small quantity of argon gas is flowed into the chamber typically at pressures on the order of 50 mTorr. The argon gas is ionized and the high energy ions bombard the target and knock off material, which is then deposited onto the wafer.

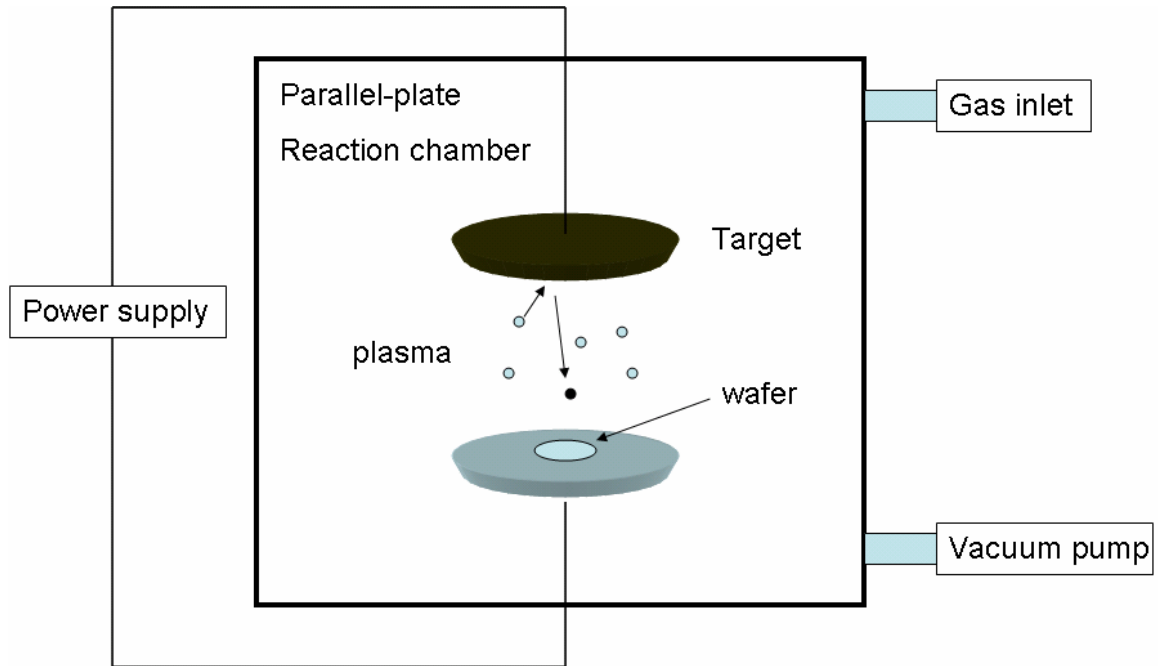


Fig. 2.1: Schematic of a sputter system showing the parallel-plate reaction chamber, and the target and wafer positions.

Two of the parameters that affect sputter deposition film quality are chamber pressure and ion energy. By controlling the chamber pressure, the mean free path of sputtered target atoms is controlled. The ion energy on the other hand, is controlled by the voltage applied to the target. The higher the voltage, the more energy the ions will have. By adjusting these two parameters, both the deposition rate and the characteristics of the deposited layer can be controlled.

2.2.2 Lithography

Lithography is the process used to transfer a mask image to a photoresist coated wafer. The patterned photoresist is then used to mask specific areas on the wafer for subsequent etching procedures. Photoresist is a special polymer that is sensitive to UV light. When the photoresist is exposed to UV light, the exposed area chemically changes

and, in the case of positive photoresist, can be easily washed away in a developer solution. Subsequent to developing, the photoresist is baked in an oven (hard bake), making it more durable for subsequent etch processes. Figure 2.2 is a flow chart of the typical lithography process.

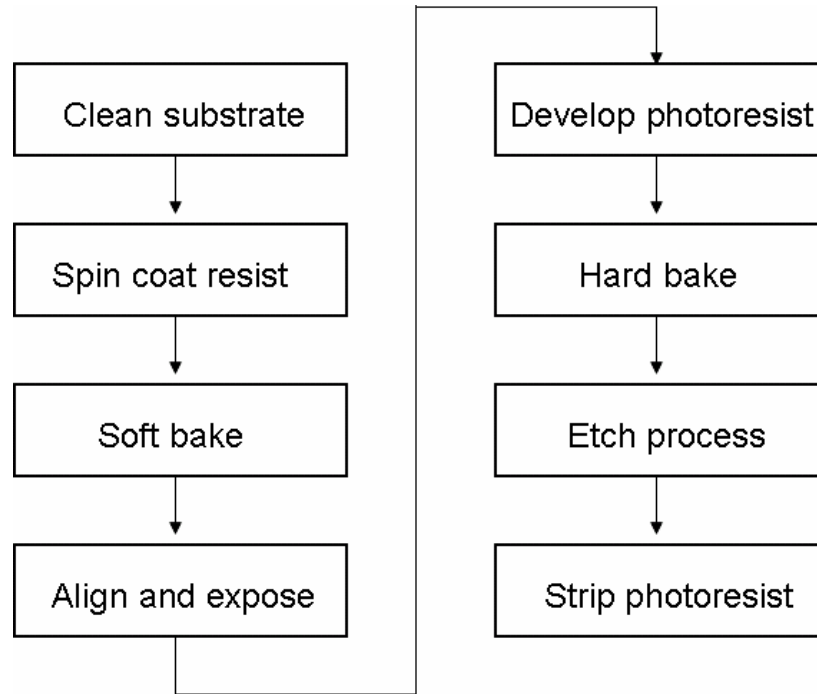


Fig. 2.2: Flow chart of a typical lithography process.

There are several parameters that need to be considered when doing lithography. One parameter is the thickness of the photoresist, which is controlled by choosing the appropriate spin rate for the wafer when the photoresist is applied. Specific thicknesses of photoresist correspond to different rotation rates of the photoresist spinner. The thickness of the photoresist layer determines how long the photoresist needs to be exposed to the UV light. The length of exposure is the second parameter that needs to be considered. If the photoresist is thicker, it will require a longer exposure time.

2.2.3 Etching Methods

Etch methods can be broken up into two basic groups: wet etching and dry etching. The type of etch method chosen depends on what material is to be removed and also what etch profile is desired.

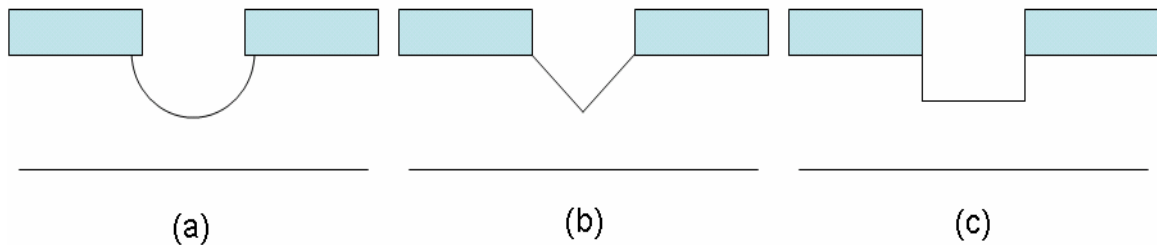
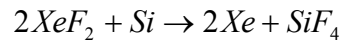


Fig. 2.3: Etch profiles for different types of etches. (a) Isotropic etch typical of wet etch processes, (b) anisotropic KOH etch profile due to etching of a $\langle 100 \rangle$ silicon wafer, (c) vertical anisotropic etch possible in RIE etch systems.

In a wet etch process, the wafer is immersed usually in an acid/base which chemically attacks the material to be removed. Most wet etch processes typically result in an isotropic etch (etches laterally as it etches vertically) (Fig. 2.3(a)). Some etchants, however, can anisotropically etch materials. In an anisotropic etch, the etch rate is not the same in all directions. For example, potassium hydroxide (KOH), etches the silicon $\langle 111 \rangle$ crystal plane much slower than the $\langle 100 \rangle$ plane. Therefore, when etching a $\langle 100 \rangle$ silicon wafer, sloped sides at the etch boundary occur, resulting in a side wall slope of 54.74° relative to the surface (Fig. 2.3(b)).

There are several dry etch methods. One example is XeF_2 gas etch which is an isotropic silicon etch which etches according to the following chemical reaction.



Another dry etch method involves bombarding the surface with high energy ions, where the material to be removed is eroded. Ion bombardment-based etches can result in uniform vertical etch profiles (Fig. 2.3(c)). By selecting the appropriate gases and power levels, Reactive Ion Etching (RIE) can result in etches that are mainly chemical or in etches that are mainly due to physical bombardment. Further discussion on dry etching can be found in Chapter 5 in the fabrication process.

CHAPTER 3

BACKGROUND

3.1 Overview

In this chapter, the theory behind electrostatic actuators is discussed. Several types of phase shifters such as delay line, distributed line, and defected ground plane based phase shifters will be presented, and the phase shifting mechanisms will be explained.

3.2 Electrostatic Actuators

Electrostatic actuation has been used for cantilevers [10], electrostatic comb drives [11], and rotary micromotors [12]. Electrostatic actuators act on the basic principle that opposite charges are attracted to each other. These actuators are simple to fabricate because they are essentially made of two conducting plates with a small gap in between them. Electrostatic actuation has the benefit of requiring no holding power. However, the force to voltage relationship is nonlinear.

To estimate the electrostatic force in these actuators, Coulomb's Law can be used to determine the force between two charges,

$$F_{elec} = \frac{1}{4\pi\epsilon_r\epsilon_o} \frac{q_1q_2}{x^2} \quad (3.1)$$

where q_1 and q_2 are the two charges in coulombs and x is the distance separating them. With more than two charges, it becomes necessary to determine the force between each pair of charges and use the principle of superposition to find the total resultant force. Finite element methods are one way to do these more complex calculations.

A first order approximation of the force can be found by assuming a parallel plate capacitor with no fringing fields [8]. These approximations are only good for small deflections where the two surfaces are still parallel. For a parallel plate capacitor, the energy stored at a given voltage, V , is given by,

$$W = \frac{1}{2}CV^2 = \frac{1}{2} \frac{\epsilon_r\epsilon_oAV^2}{x} \quad (3.2)$$

where A is the plate area of the capacitor and x is the distance between the two plates. The attractive force between the plates is then,

$$F_x = \frac{dW}{dx} = + \frac{1}{2} \frac{\epsilon_r \epsilon_o AV^2}{x^2} \quad (3.3)$$

From equation 3.3, it is clear that the relationship between the applied voltage and the force exerted is non-linear.

3.3 MEMS Phase Shifters

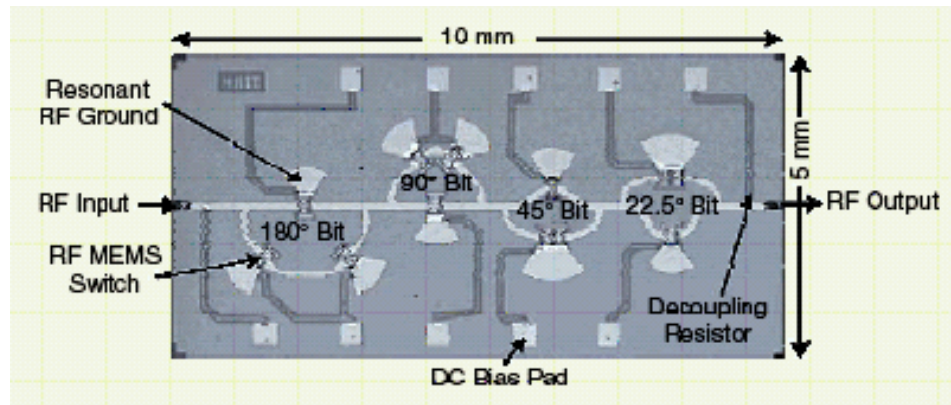
Recently, many different MEMS-based phase shifters have been demonstrated [13-20]. These phase shifters can be classified into 3 main groups: delay/switch line, load line/distributed line and phase shifters based on a defected ground plane. In reference [13], Rebeiz discussed many different MEMS-based phase shifter designs and their corresponding advantages and disadvantages.

There are a number of different metrics that can be used to compare different MEMS phase shifter designs. One metric would be the footprint of the MEMS phase shifter on a chip. Secondly, the actuation voltages required can be discussed. Lastly, the Figure of Merit (FOM) of the phase shifters can be compared. The FOM is defined as the ratio between the phase shift and the loss in dB's. These losses include the insertion losses of any micro-switches being employed and line losses. The FOM of a good phase shifter should be greater than 100°/dB. This indicates that for a full 360° phase shift, the signal is still better than 3 dB.

3.3.1 Delay/switch Line Phase Shifters

In delay line or switch line phase shifters, MEMS micro-switches are used to route the RF signal along transmission lines of different lengths. By selecting the desired

path of the RF signal, the total length of the transmission line is changed and large, discrete phase shifts can be achieved [14]. The different transmission line lengths are chosen by selecting certain “bits” which corresponding to switches that route the RF signal.

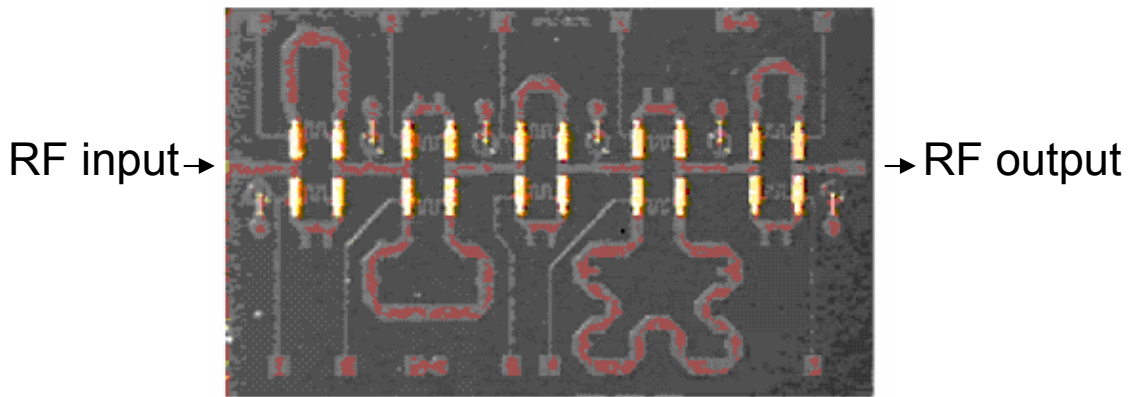


Pillans, B. *et al.*, “Ka-band RF MEMS phase shifters”
 Microwave and Guided Wave Letters, IEEE
 © (1999) IEEE. All rights reserved. Used with permission.

Fig. 3.1: Delay line phase shifter that uses micro-switches to re-route the RF signal to different transmission line segments [14].

Figure 3.1 shows a 4-bit phase shifter designed for the Ka band (40 GHz). For switch-line phase shifters, the phase shift is linear with frequency. The key component to the delay line phase shifter is the design of the RF MEMS switches. These switches need to be low-loss. They need to be designed so that they have low insertion loss when “on” and high isolation when “off”. The micro-switches in this design had an average loss of 0.25 dB/switch over the different line configurations. At 34 GHz, to achieve a 315° phase shift, the insertion loss was 2.2 dB which translates to a Figure of Merit of 143°/dB of insertion loss. The actuation voltage for the individual switches was 45 V, and the switch times were 3-6 μ s. As can be seen in the figure, the 4-bit phase shifter’s area is 5 mm x 10 mm.

Current work in the switch-line phase shifter area involves improving the MEMS micro-switches to decrease signal loss [15, 16]. The 3-port MEMS switch discussed in [16], is used in a 5-bit switched-line phase shifter [17] shown in Figure 3.2. The footprint of the phase shifter is 7 mm x 4 mm. The actuation voltage for the micro-switch is 25 V. The 3-port MEMS switch has an insertion loss of 0.66 dB at 10 GHz. With an average of 3.6 dB insertion loss for the entire system, assuming a phase shift of 300°, the Figure of Merit would be 83°/dB of insertion loss. Note how the geometry of the delay lines is designed in order to minimize the area required for the phase shifter.



Jian, Z., *et al.*, "A Compact 5-bit Switched-line Digital MEMS Phase Shifter"
 Proceedings of 1st IEEE International Conference on Nano/Micro Engineered and Molecular Systems
 © (2006) IEEE. All rights reserved. Used with permission.

Fig. 3.2: Photograph of a 5-bit phase shifter with a die size of 7 mm x 4 mm [17].

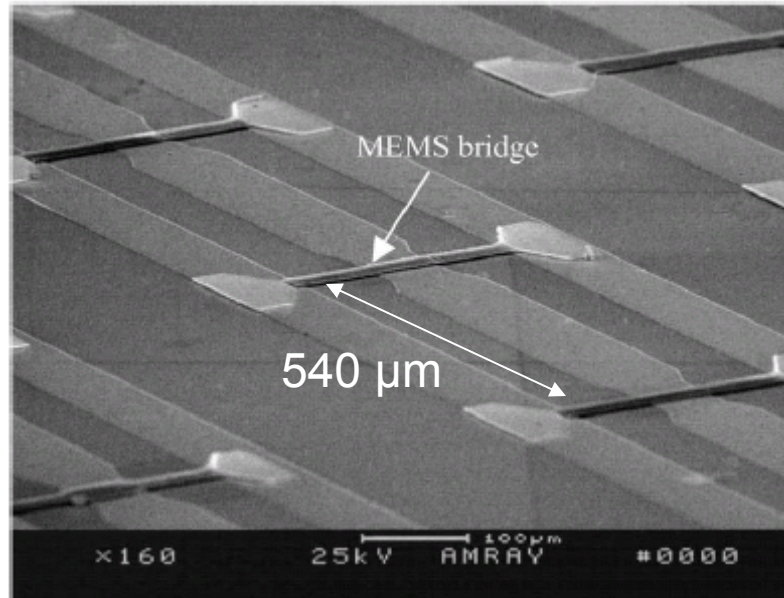
A disadvantage of switched, delay-line phase shifters is that if one of the micro-switches fails, the whole phase shifter fails. These phase shifters are also limited to discrete phase shifts due to the limited possible signal paths. Also, since the RF signal is routed through the MEMS micro-switches, there are necessary device power limitations

to prevent micro-switch failures. Power levels over a few milliwatts typically are enough to damage the switches.

3.3.2 Load line/distributed Line Phase Shifters

Barker and Rebeiz were among the first to do extensive work on distributed MEMS transmission lines (DMTL) [18]. The DMTL is made of a high impedance line ($>50 \Omega$) that is periodically loaded by MEMS bridges that act as capacitors. By controlling the load impedance of the transmission line, a phase shift can be achieved. The FOM of DMTL phase shifters is slightly worse in terms of line loss compared to those of switch-line phase shifters for frequencies up to 30 GHz, but DMTL phase shifters become competitive and even surpass switch-line phase shifters at frequencies of 40 GHz and above [19].

In reference [20], Hung et al. demonstrated a Ka-band DMTL phase shifter on a silicon substrate using AlSi bridges. The phase shifter used 13 MEMS bridges at a spaced 540 μm apart (Fig. 3.3). The bridges were fabricated out of an AlSi alloy in order to increase flexibility. The actuation voltage of the MEMS bridges was 27 V.



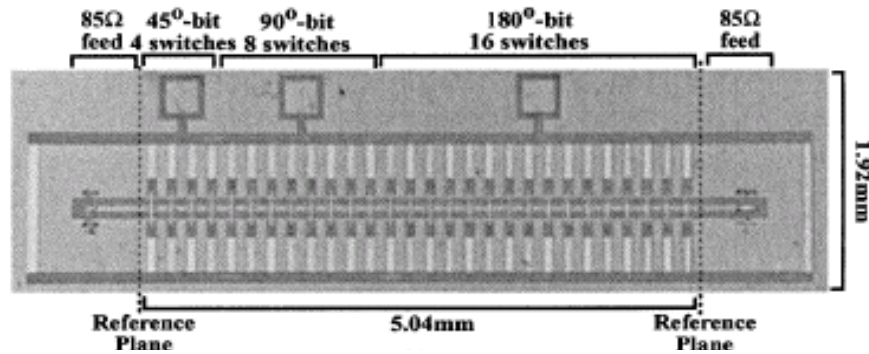
Qing, J., *et al.*, “Ka-band Distributed MEMS Phase Shifters on Silicon Using AlSi Suspended Membrane”
 Journal of Microelectromechanical Systems
 © (2004) IEEE. All rights reserved. Used with permission.

Fig. 3.3: SEM photograph of a MEMS bridge in a DMTL [20].

As can be inferred from the figure, the DMTL fabrication process requires multiple metal layers. Also, the transmission line length needs to be long in order to accommodate all the MEMS bridges, 7.56 mm in this example. However, DMTL phase shifters are capable of operating over larger bandwidths than the switch-line phase shifters. At 36 GHz, a phase shift of 286° was achieved with an insertion loss of 1.75 dB. This translates to a Figure of Merit of $163^\circ/\text{dB}$ of insertion loss.

In reference [19], a 2- and 3-bit W-Band DMTL phase shifter on a glass substrate was demonstrated. The 3-bit version used a total of 32 bridges. The 45° -bit used 4 bridges, the 90° -bit was made up of 8 bridges, and the 180° -bit was made up of 16 bridges (Fig. 3.4). More bridges are required to achieve larger phase shifts. This phase shifter had an area of 1.92 mm x 5.04 mm and the measured pull-down voltage was 30 V.

The phase shifter performed well for a wide frequency range. Reported FOM were 93°/dB – 100°/dB of insertion loss at 75-110 GHz.

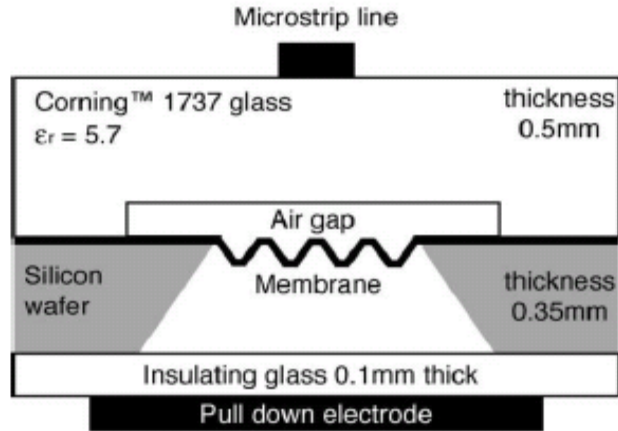


Hung, J.-J., *et al.*, “Distributed 2- and 3-bit W-band MEMS Phase Shifters on Glass Substrates”
 IEEE Transactions on Microwave Theory and Techniques
 © (2004) IEEE. All rights reserved. Used with permission.

Fig. 3.4: Photograph of a 3-bit W-band DMTL [19].

3.3.3 Defected Ground Plane Phase Shifters

A reconfigurable ground plane based phase shifter was demonstrated in reference [5]. The use of corrugated membranes in the ground plane allows for a phase shift to occur when the membrane is electrostatically deflected away from the RF substrate (Fig. 3.5). An example of a corrugated membrane can be seen in Figure 3.6.



Shafai, C., *et al.*, “Microstrip Phase Shifter Using Ground-Plane Reconfiguration”
 IEEE Transactions on Microwave Theory and Techniques
 © (2004) IEEE. All rights reserved. Used with permission.

Fig. 3.5: Schematic of the corrugated membrane based phase shifter of [5].



Shafai, C., *et al.*, “Microstrip Phase Shifter Using Ground-Plane Reconfiguration”
 IEEE Transactions on Microwave Theory and Techniques
 © (2004) IEEE. All rights reserved. Used with permission.

Fig. 3.6: Photograph of corrugated membrane used in the reconfigurable ground plane of [5].

A series of five 4.3 mm diameter circular membranes was used to achieve a phase shift of 30° at 12.08 GHz and 32° at 15.00 GHz. A 10.4 mm diameter membrane showed a phase shift of 56° at 14.25 GHz. Even though the membranes were corrugated to improve flexibility, the actuation voltage, 405 V, was still quite large due to the 0.45 mm separation distance between the corrugated membranes and the pull-down electrode. In these phase shifters, the insertion loss is not dependent on the membrane deflection, so

high Figures of Merit can be achieved. With a single membrane 10.4 mm in diameter, the Figure of Merit at 11 GHz was 708°/dB of line loss for a 37° phase shift, and at 14.25 GHz, the Figure of Merit was 612°/dB of line loss for a 55° phase shift. Also, the RF power limitations that occur in switch-line phase shifters do not apply to this device.

The micro-ribbon arrays presented in this thesis operate under the same principles as the corrugated membrane phase shifter just described. The required actuation voltage could be reduced since the micro-ribbon array was more flexible than the corrugated membranes. The actuation voltage was also reduced because the micro-ribbon arrays could be fabricated in such a way that reduced the separation distance between the ground and the pull-down electrode.

CHAPTER 4

DESIGN AND MODELING OF MICRO-RIBBONS

4.1 Overview

This chapter of the thesis describes the finite-element modeling (FEM) of the micro-ribbons using the software tool, COMSOL™[6]. These simulations were carried out in order to investigate the mechanical properties of the micro-ribbons. The evolution of the simulation setup is explained and discussed. This includes the explanation of the adjacent ground planes in the simulations that were introduced to decrease computation time and yet model the environment accurately. Different micro-ribbon geometries are presented and compared with each other.

4.2 Simulation Setup

The simulator COMSOL Multiphysics™ [6] is a finite-element modeling (FEM) program that allows for a variety of multiphysics simulations. It is an appropriate software tool to model the electrostatic actuation of the micro-ribbon array because it allows for mechanical and electrostatic modeling in the same simulation. COMSOL was used to simulate the electrostatic fields that exist between the grounded micro-ribbons and the pull-down electrode. It then applied the calculated electrostatic forces to the structure in order to simulate the corresponding micro-ribbon deflection.

The MEMS module of COMSOL was used with the “Electrostatics” and “Structural Mechanical – solid, stress-strain” sub-modules. The multiphysics simulations were done in 3D. For the electrostatic part of the simulation, the micro-ribbon was grounded while an “electric potential” boundary condition was applied to the pull-down electrode. Next, a problem space was defined around the model, and the boundary condition on this space was “zero symmetry”. For the mechanical section of the multiphysics simulation, only the micro-ribbon being simulated was active in that domain. The ends of the micro-ribbons were constrained, and the corresponding electrostatic force was applied to the other edges of the micro-ribbons (Table 4-1 and Table 4-2). Appendix A presents a step by step procedure for the COMSOL simulation set up.

Table 4-1: Boundary conditions for the electrostatic sub-module.

Simulation Component	Boundary Condition
bounding box	Zero charge/symmetry
micro-ribbon	ground
pull-down electrode	electric potential

Table 4-2: Boundary conditions for the mechanical-plane stress sub-module.

Simulation Component	Boundary Condition
Micro-ribbon ends	Constrained in x, y, and z
Remaining micro-ribbon surfaces	$F_x = -0.5V_x * nD_{es}^*$ $F_y = -0.5V_y * nD_{es}^*$ $F_z = -0.5V_z * nD_{es}$ <p><i>(where V_x, V_y, V_z, and nD_{es} (charge density) are values calculated by the electrostatics module)</i></p>
	<p>*F_x and F_y are 12 or 13 orders of magnitude smaller than F_z in the simulations presented.</p>

During the initial simulations, it was noted that the width of the bounding box (Fig. 4.1) affected the force on the micro-ribbon being simulated. In these simulations, a single micro-ribbon was simulated rather than simulating an entire array of micro-ribbons in order to reduce computation time. A problem with this technique was that for simulations that required a larger bounding box, a larger electrostatic force was observed on the micro-ribbon. The large force resulted in different deflections for a constant applied voltage that was dependent on the bounding box dimensions.

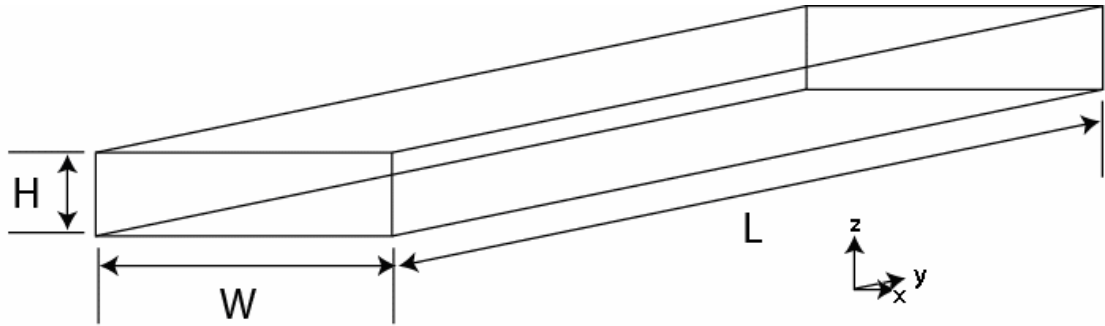


Fig. 4.1: Illustration of the COMSOL simulation bounding box.

One solution to this problem would be to choose a width large enough to include most of the fringing capacitance due to the fringing fields (Fig. 4.2). However, this would not be an accurate simulation with regard to the actual final experimental setup. A typical micro-ribbon in the array would have adjacent ribbons that would reduce the actual electrostatic force that was applied to the micro-ribbon.

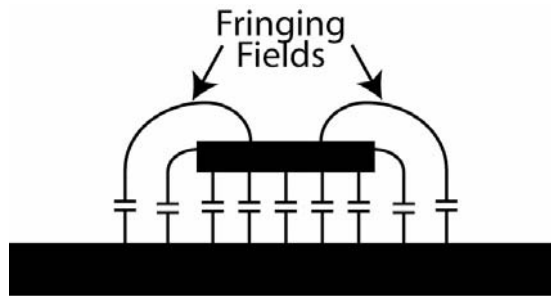


Fig. 4.2: Illustration of the fringing fields on a micro-ribbon, showing the field extension beyond the ribbon width.

In order to solve the problem mentioned above, adjacent rigid ground strips were introduced in the simulation. In this simulation setup, one micro-ribbon was simulated with air gaps to represent the separation distance between ribbons in the array and rigid grounds adjacent to the micro-ribbon (Fig. 4.3).

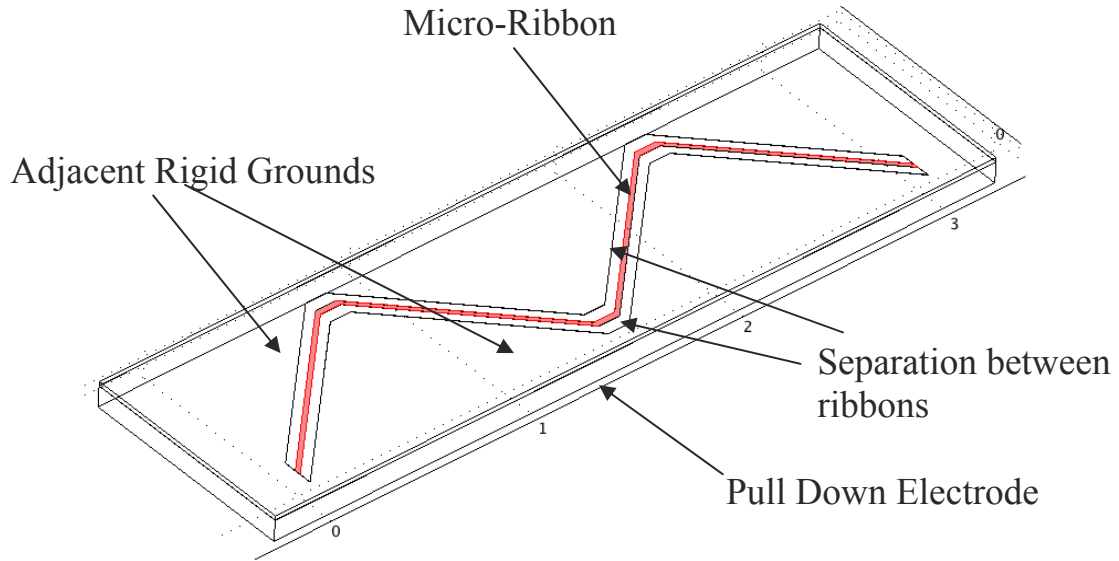


Fig. 4.3: Illustration of the simulation setup with adjacent rigid grounds.

This setup was the solution to a few problems. Firstly, with the rigid grounds in place, the electrostatic force was no longer dependent on the width of the ground plane being simulated. Secondly, the addition of the rigid ground planes helped to reduce computation times. Since the majority of the computation time was used to determine the mechanical deflection of the micro-ribbon, having the adjacent grounds being rigid it did not increase the computation time. Also, the rigid ground sections allowed for an accurate simulation of a single micro-ribbon with the correct fringing capacitance without having to simulate the entire micro-ribbon array for small deflections.

For most of the simulations, the problem box was defined to be 3.5 mm x 1 mm x 120 μm (Table 4-3). These dimensions were chosen after several simulations were done with smaller and larger bounding boxes. Typical simulations had ~ 60000 mesh elements with 130000+ degrees of freedom.

Table 4-3: Bounding box dimensions in a typical simulation.

Bounding box	Dimension
length	3.5 mm
width	1 mm
height	120 μm

The majority of the simulations discussed in this chapter and thesis were done as described above. These simulations were useful for relating specific electrostatic forces with their corresponding micro-ribbon deflection. However, it should be noted that even though the voltage was set for the simulations, the corresponding micro-ribbon deflection would be underestimated, because the meshing was not dynamic. i.e., the electrostatic force that produced the deflection was only calculated for the initial zero-deflection. In practice, as the micro-ribbon gets closer to the pull-down electrode, the electrostatic force would increase because the separation distance between the micro-ribbon and pull-down electrode had decreased. Simulations of this type will always be denoted as simulations with adjacent rigid grounds.

A second type of simulation was also done on a few occasions. These simulations were not multiphysics simulations. They only used the structural mechanics – solid, stress-strain module. In these simulations, only the micro-ribbon was represented, and a uniform pressure was applied to the micro-ribbon. These simulations were useful to enable quick comparisons of different micro-ribbon geometries to determine differences in spring constant and resonant frequencies.

4.3 Straight Micro-Ribbons

It would be beneficial to study the behaviour of a simple straight beam before simulations of more complex micro-ribbon designs are discussed. A few simulations were therefore carried out using the dimensions for the straight beams found in Table 4-4.

Table 4-4: Dimensions of the straight beams simulated.

Beam	Length (μm)	Width (μm)	Thickness (μm)	Separation from adjacent ribbons (μm)
1	3000	20	1	50
2	3000	50	1	50

Two simulations were done using Beam 1 with the adjacent rigid grounds. The first simulation was for voltages ranging from 1-6 V. The second simulation was for voltages ranging from 5-30 V. The results can be seen in Table 4-5 and Table 4-6. A similar simulation was done for Beam 2 (a beam that is 2.5 times wider than Beam 1) for voltages ranging from 5-30 V with adjacent rigid grounds (Table 4-7). These tables show the voltages, maximum deflection, electrostatic force (in the z-direction), and spring constant, where,

$$\text{Spring Constant, } k = \frac{\text{Total Electrostatic Force}}{\text{Maximum Deflection At Ribbon Centre}} \quad (4.1)$$

The total electrostatic force was determined by doing a boundary integration across the entire micro-ribbon in order to find the total F_z .

Table 4-5: Deflection and force on Beam 1 with voltages ranging from 1-6 V.

Voltage (V)	Maximum Deflection (m)	Electrostatic Force (N)	Spring Constant (N/m)
1	3.2×10^{-8}	5.5×10^{-11}	1.7×10^{-3}
2	1.3×10^{-7}	2.2×10^{-10}	1.7×10^{-3}
3	2.9×10^{-7}	4.9×10^{-10}	1.7×10^{-3}
4	5.2×10^{-7}	8.7×10^{-10}	1.7×10^{-3}
5	8.1×10^{-7}	1.4×10^{-9}	1.7×10^{-3}
6	1.2×10^{-6}	2.0×10^{-9}	1.7×10^{-3}

Table 4-6: Deflection and force on Beam 1 with voltages ranging from 5-30 V.

Voltage (V)	Maximum Deflection (m)	Electrostatic Force (N)	Spring Constant (N/m)
5	8.1×10^{-7}	1.4×10^{-9}	1.7×10^{-3}
10	3.2×10^{-6}	5.5×10^{-9}	1.7×10^{-3}
15	7.3×10^{-6}	1.2×10^{-8}	1.7×10^{-3}
20	1.3×10^{-5}	2.2×10^{-8}	1.7×10^{-3}
25	2.0×10^{-5}	3.4×10^{-8}	1.7×10^{-3}
30	2.9×10^{-5}	4.9×10^{-8}	1.7×10^{-3}

Table 4-7: Deflection and force on Beam 2 with voltages ranging from 5-30 V.

Voltage (V)	Maximum Deflection (m)	Electrostatic Force (N)	Spring Constant (N/m)
5	6.0×10^{-7}	2.5×10^{-9}	4.1×10^{-3}
10	2.4×10^{-6}	9.9×10^{-9}	4.1×10^{-3}
15	5.4×10^{-6}	2.2×10^{-8}	4.1×10^{-3}
20	9.6×10^{-6}	4.0×10^{-8}	4.1×10^{-3}
25	1.5×10^{-5}	6.2×10^{-8}	4.1×10^{-3}
30	2.2×10^{-5}	8.9×10^{-8}	4.1×10^{-3}

From the above tables, it can be seen that Beam 2 has a higher spring constant compared to Beam 1. The calculated spring constant is ~ 2.5 times larger than the narrower beam which was expected because the beam was 2.5 times wider. However, the electrostatic force is only ~ 1.8 times larger. This was also expected, because the

thinner beam focused the fringe capacitance so even though the spring constant scales linearly with width, the electrostatic force on a micro-ribbon in an array setting does not.

Something interesting to note about the above tables is that the spring constant is a constant for the respective micro-ribbons no matter how much the micro-ribbon was deflected. This is not the case in a real system. The more a material is deflected, the harder it should be to continue to deflect it. In COMSOL, there is an option in the plain stress module to account for “large deformation” and thus the spring constant that it calculates is non-constant. The more the micro-ribbons are deflected, the harder it becomes to deflect them. This difference becomes significant when the deflection is more than the thickness of the beam. A simulation of Beam 1 was done using this option, and the results are found in Table 4-8. Figure 4.4 shows the nonlinear spring constant with “large deformation” on compared to the simulations done with “large deformation” off. The rest of the simulations presented will have large deformation enabled unless otherwise stated.

Table 4-8: Deflection and force on Beam 1 with voltages ranging from 5-30 V.

Voltage (V)	Maximum Deflection (m)	Electrostatic Force (N)	Spring Constant (N/m)
5	4.5×10^{-7}	8.7×10^{-10}	1.9×10^{-3}
10	8.0×10^{-7}	2.0×10^{-9}	2.5×10^{-3}
15	1.1×10^{-6}	3.5×10^{-9}	3.2×10^{-3}
20	1.4×10^{-6}	5.5×10^{-9}	4.0×10^{-3}
25	1.6×10^{-6}	7.9×10^{-9}	4.9×10^{-3}
30	1.9×10^{-6}	1.3×10^{-8}	5.8×10^{-3}

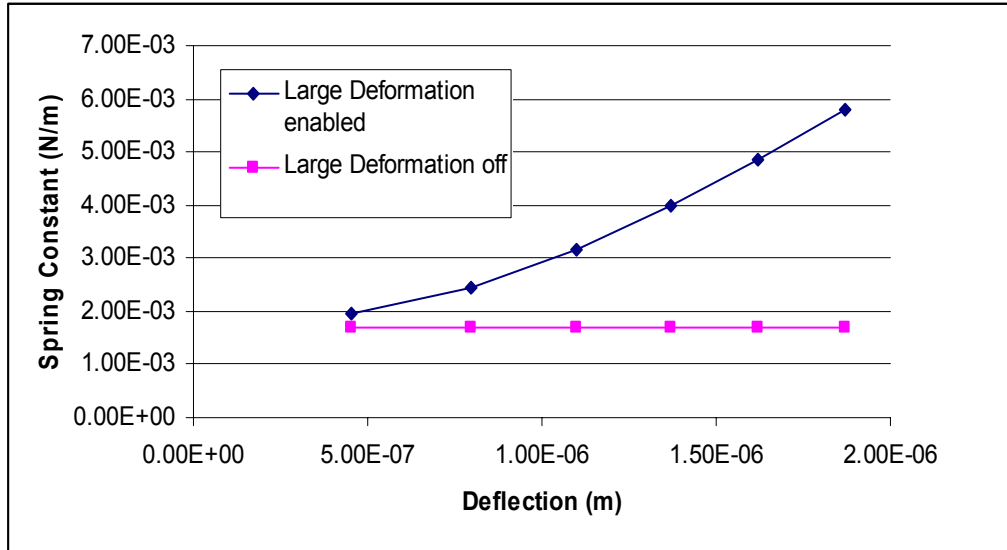


Fig. 4.4: Graph showing the effects of having the option “Large Deformation” enabled. The spring constant of a beam increases as the beam is deflected.

4.4 The Number of Segments in the Micro-ribbon

Simulations were next carried out for different micro-ribbon designs. Flexibility of the micro-ribbons was enhanced by adding bends to the ribbon creating an in-plane spring which increased flexibility. An investigation was carried out to see what would happen with the introduction of more and more jogs or bends. An arbitrary angle of 22.5° was chosen for the first set of simulations. Figure 4.5 shows the geometries of the micro-ribbons simulated.

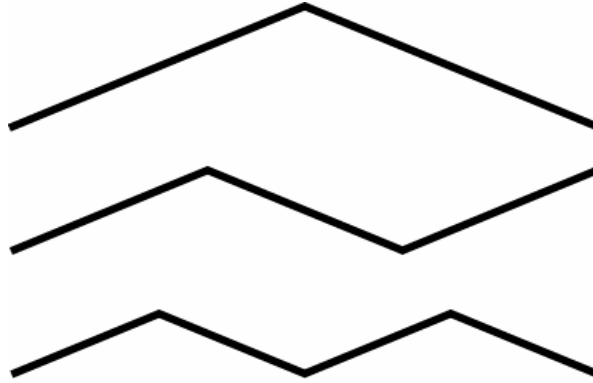


Fig. 4.5: Top view of geometries of micro-ribbons at 22.5° angle to the longitudinal with 2, 3 and 4 segments. Each micro-ribbon spanned a length of 3 mm. The actual length of the micro-ribbons varied.

Simulations were first done without the “large deformation” option enabled, because these were faster to run computationally. The micro-ribbons were 20 μm in width, 1 μm thick and spanned a length of 3 mm. The micro-ribbons were 100 μm above the pull-down electrode. The results can be seen in Table 4-9.

Table 4-9: Simulated spring constant for micro-ribbons of differing number of segments.

Segments	Spring Constant (N/m)
2	1.1×10^{-3}
3	1.5×10^{-3}
4	1.6×10^{-3}
5	1.6×10^{-3}
6	1.5×10^{-3}
7	1.6×10^{-3}

From these simulations, one cannot draw significant conclusions about how the number of segments affected the spring constant of the micro-ribbon, other than the 2 segment micro-ribbons being the most flexible. Another set of simulations were carried

out with the “Large Deformation” option enabled. The following figure shows the results of those simulations (Fig. 4.6).

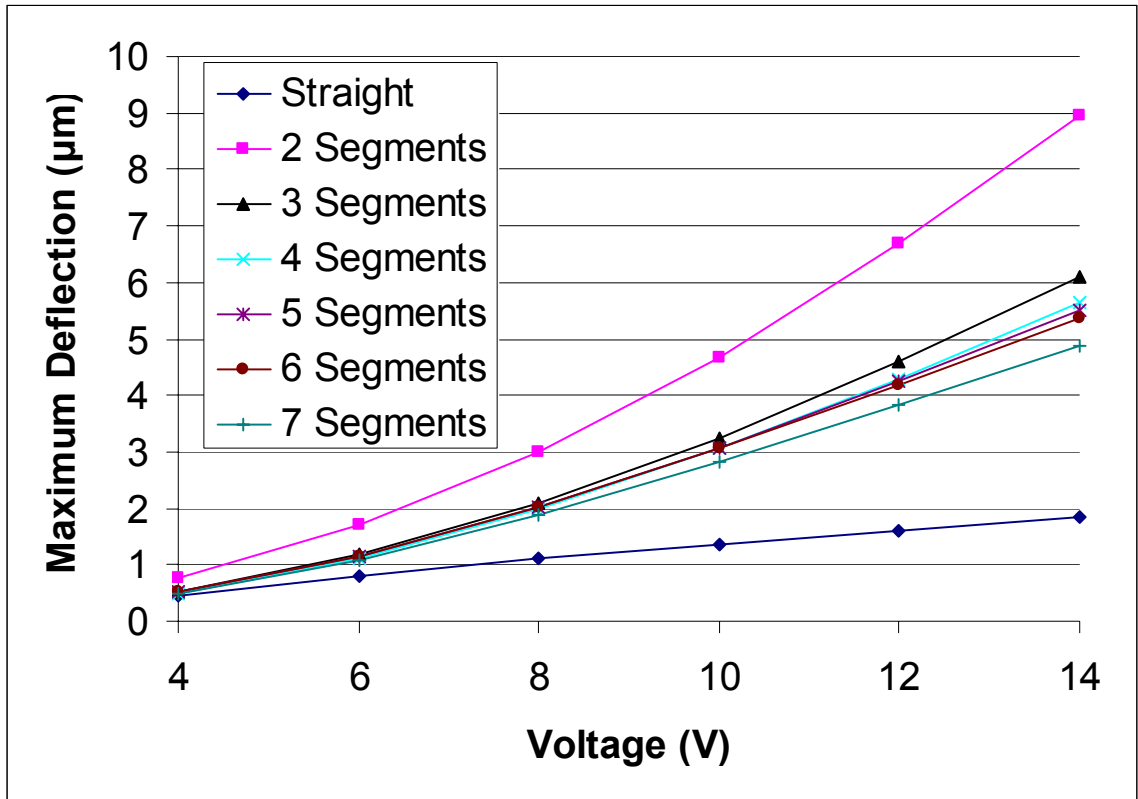


Fig. 4.6: Simulation of ribbon deflection as a function of voltage for different numbers of segments with the “large deformation” option enabled.

With the results from these simulations, the 2 segment ribbon again is seen as being the most flexible. The micro-ribbon clearly became stiffer and stiffer as more segments were added. It would appear that as more and more segments are added, the micro-ribbon would eventually be equivalent to the straight beam case. However, these simulations only accounted for small deflections ($<10 \mu\text{m}$). In the final application, the micro-ribbons were expected to deflect $60 \mu\text{m}$.

Another set of simulations was carried out for the same micro-ribbons but this time without rigid adjacent grounds and with uniform pressures applied to the micro-ribbon resulting in total electrostatic forces of 1×10^{-7} N and 5×10^{-7} N (Table 4-10, Table 4-11). This was done because the simulations with the rigid adjacent grounds underestimate the deflection for a given voltage, as previously discussed. The simulations with a uniform pressure more accurately model the deflection as a function of force. For these simulations, the “large deformation” option was enabled.

Table 4-10: Simulated spring constant for 3 mm long and 1 μ m thick aluminum micro-ribbons of differing number of segments with uniform pressure resulting in an electrostatic force = 1×10^{-7} N.

Segments	Maximum Deflection (m)	Spring Constant (N/m)
Straight	4.3×10^{-6}	2.3×10^{-2}
2	5.2×10^{-5}	2.0×10^{-3}
3	2.9×10^{-5}	3.5×10^{-3}
4	2.3×10^{-5}	4.4×10^{-3}
5	2.1×10^{-5}	4.8×10^{-3}
6	2.0×10^{-5}	5.2×10^{-3}
7	1.7×10^{-5}	5.9×10^{-3}

Table 4-11: Simulated spring constant for 3 mm long and 1 μ m thick aluminum micro-ribbons of differing number of segments with uniform pressure resulting in an electrostatic force = 5×10^{-7} N.

Segments	Maximum Deflection (m)	Spring Constant (N/m)
Straight	7.5×10^{-6}	6.7×10^{-2}
2	1.4×10^{-4}	3.7×10^{-3}
3	5.8×10^{-5}	8.7×10^{-3}
4	4.4×10^{-5}	1.2×10^{-2}
5	4.0×10^{-5}	1.3×10^{-2}
6	3.7×10^{-5}	1.4×10^{-2}
7	3.2×10^{-5}	1.6×10^{-2}

These simulations clearly show that the spring constant increases with the number of segments. With the larger, more relevant deflections, it is seen that the 2 segment

ribbon is the most flexible and the spring constant increases with the number of segments.

4.4.1 *Micro-ribbons with straight segments at the jogs*

Other simulations were carried out using a further slight variation in the design. For the sake of discussion, only the 4 segment geometries will be discussed even though more simulations were carried out. The modification to the geometry consisted of adding a straight segment at the jogs. This segment was 100 μm in length. Simulations were also carried out for a 4 segment micro-ribbon with a jog angle of 45° to the length axis, and for the same micro-ribbon with a straight segment at the jogs. The geometries are shown in Figure 4.7.

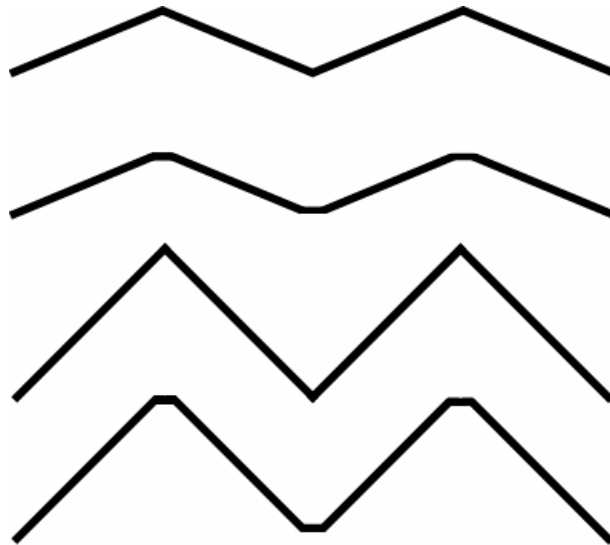


Fig. 4.7: Geometries of 4 segment micro-ribbons with and without straight segments at the jogs.

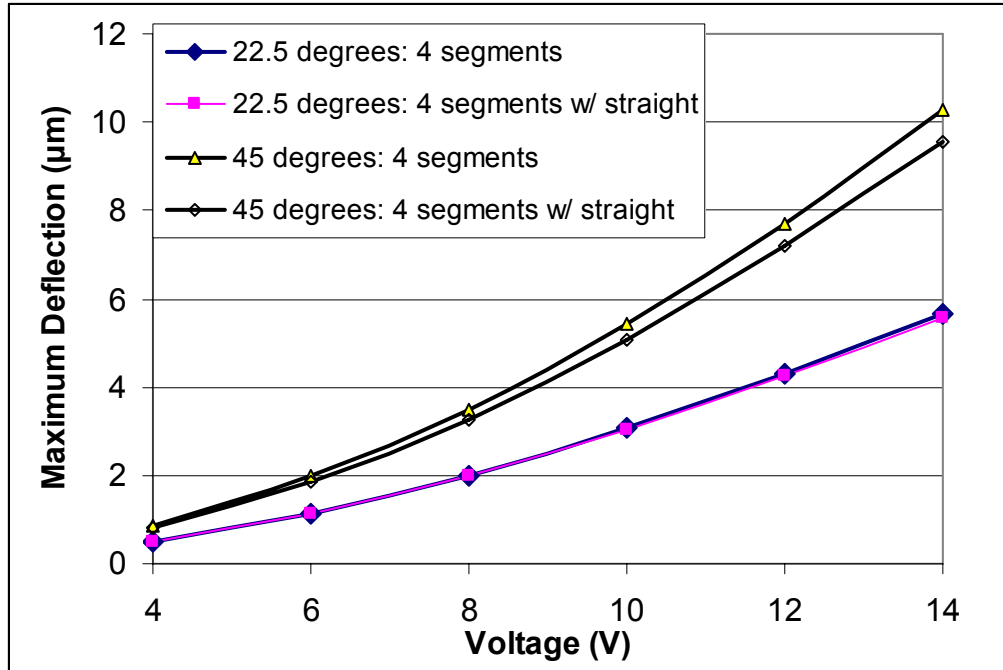


Fig. 4.8: Simulated deflection as a function of voltage for 4 segment micro-ribbons with and without straight segments at the jogs. Both 22.5° and 45° geometries are shown. The two 22.5° lines overlap each other.

The result of these simulations can be seen in Figure 4.8. It can be seen that adding the straight segments does not make a large difference to the flexibility of the micro-ribbons. The straight segments actually made the micro-ribbons slightly stiffer.

4.5 Varying Jog Angles

The jog angle discussed in this thesis refers to the angle the micro-ribbon bends off the length axis (Fig. 4.9).

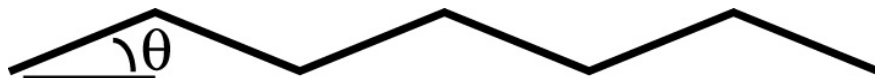


Fig. 4.9: Illustration of the jog angle.

In the above simulations (Fig. 4.8), it appears that the 45° geometry micro-ribbon is significantly more flexible than the 22.5° geometry. However, it is not clear whether the angle makes it more flexible, or whether the change in the surface area accounts for the increase in flexibility, because the 45° geometry micro-ribbon has $\sim 30\%$ more surface area. To further investigate this question, another set of simulations was done to compare 22.5° , 45° , and 67.5° geometries. The surface area was held constant by varying the span length of the micro-ribbon. The 4 segment geometry was used with each segment being $500\ \mu\text{m}$ in length as seen in Figure 4.10.



Fig. 4.10: Illustration of the 4-segment geometries at 22.5° , 45° , and 67.5° with each segment being $500\ \mu\text{m}$ in length.

The results of the simulation can be seen in Figure 4.11 which shows the maximum deflection vs. voltage. In these simulations, the electrostatic forces were very comparable, since in all cases the micro-ribbons had approximately the same surface area.

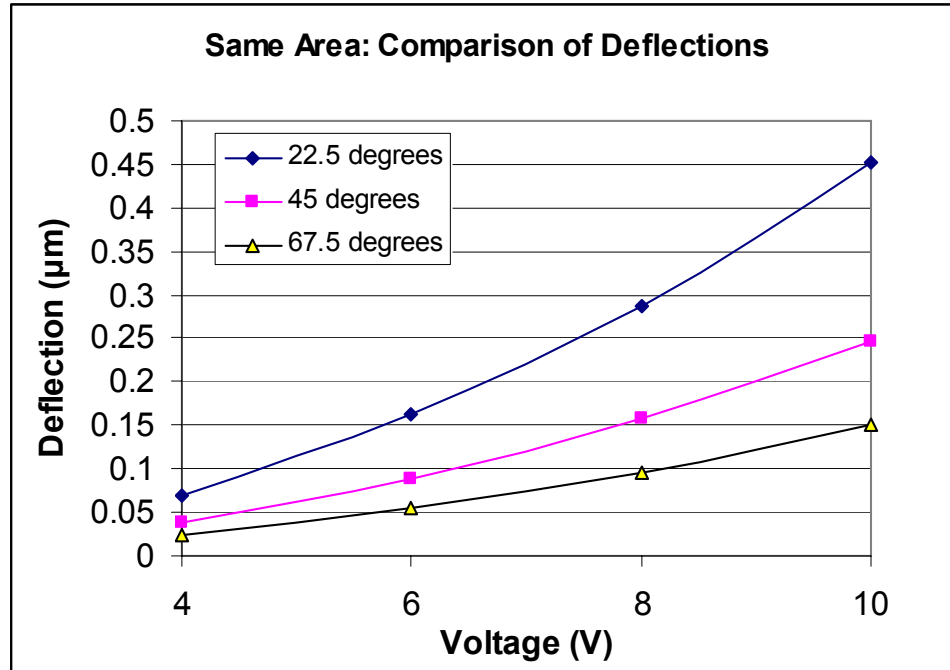


Fig. 4.11: Simulated deflection as a function of voltage for the micro-ribbons in Figure 4.10 for jog angles of 22.5°, 45° and 67.5°.

From these results, the 22.5° geometry is visually more flexible compared to the larger angles. However, for a given span, the larger the angle the more flexible the micro-ribbon would be due to the increase in electrostatic force due to the larger surface area.

Resonant Frequency:

Simulations were carried out to investigate the fundamental mechanical resonant frequency and spring constant as a function of jog angle. The following graphs show jog angles from 5-45° for a 4 segment beam that spans a length of 3 mm. The beams were 20 µm wide and 1 µm thick aluminum. Smaller angles lead to stiffer beams and therefore had a higher resonant frequency. A device with a resonant frequency of 400 Hz is

acceptable for applications that do not require fast switching between different phase shifts.

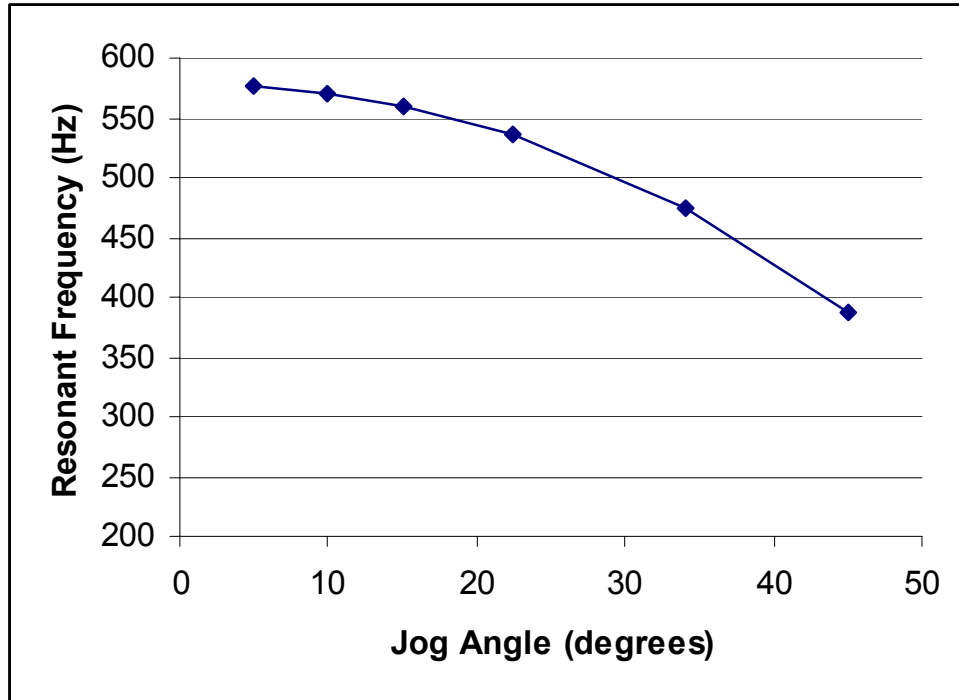


Fig. 4.12: Simulated resonant frequency vs. jog angle for a 4 segment beam.

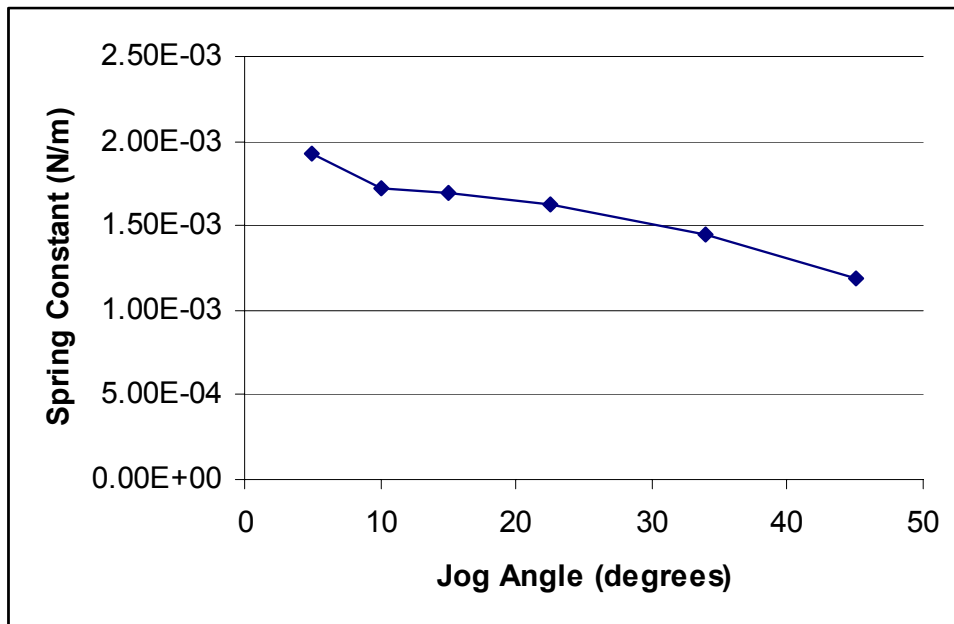


Fig. 4.13: Simulated spring constant vs. jog angle for a 4 segment beam.

4.6 Simulation of Different Complex Designs

It would be beneficial for the final application if there was a straight section in the middle of the micro-ribbon. This straight section should ideally remain relatively flat and thus behave better as a ground plane in the phase shifter setup. Four different geometries were simulated. Again, the 4 segment geometry was used with a straight beam in the middle. The straight section accounted for half the length of the entire micro-ribbon. The geometries can be seen in Figure 4.14. The geometries are referred to as “both up” indicating both angled ends are in the same direction, “up/down” indicating that the angled ends are in the opposite directions, and “complex 1” and “complex 2” to describe the other two geometries accordingly. There is also one micro-ribbon that has 8 segments. This micro-ribbon was used as a comparison.

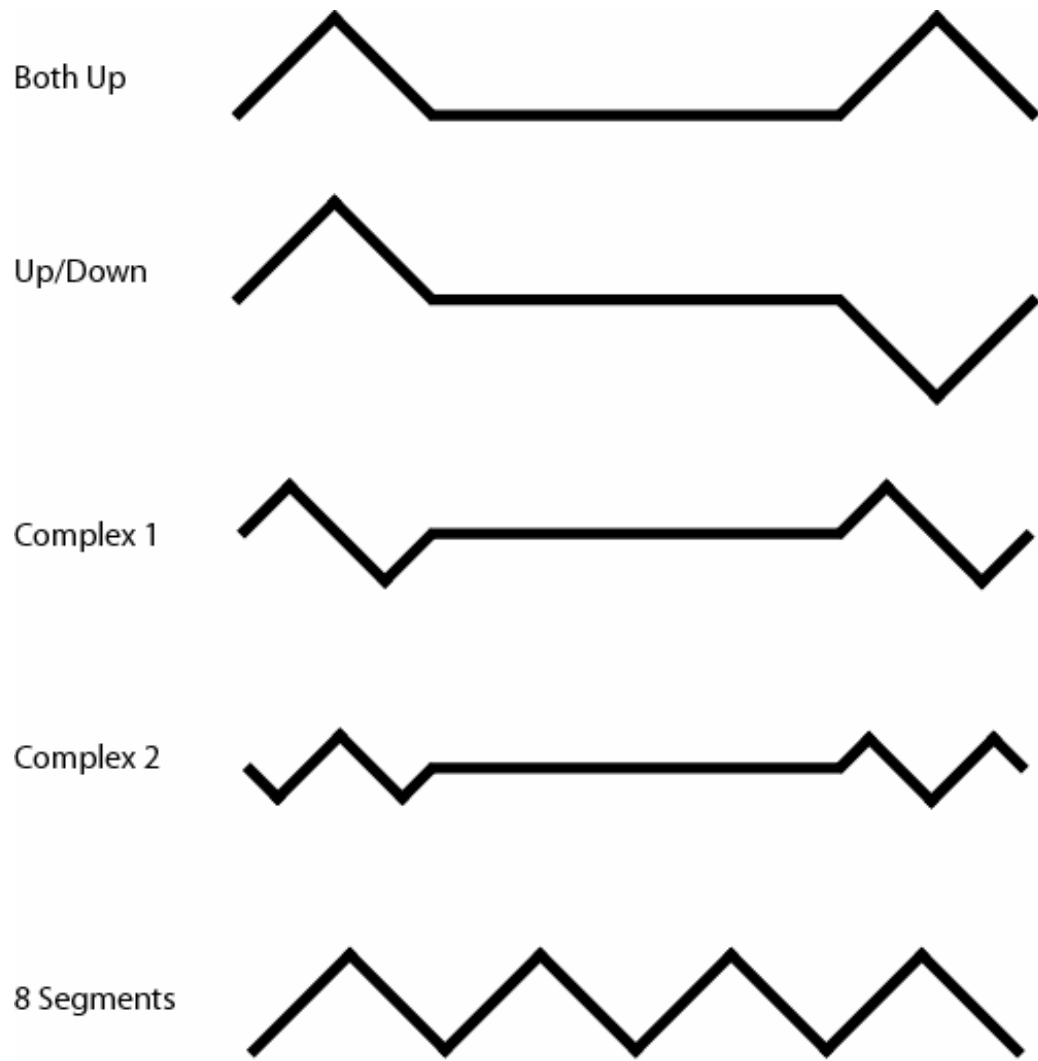


Fig. 4.14: Illustrations of the more complex geometries simulated.

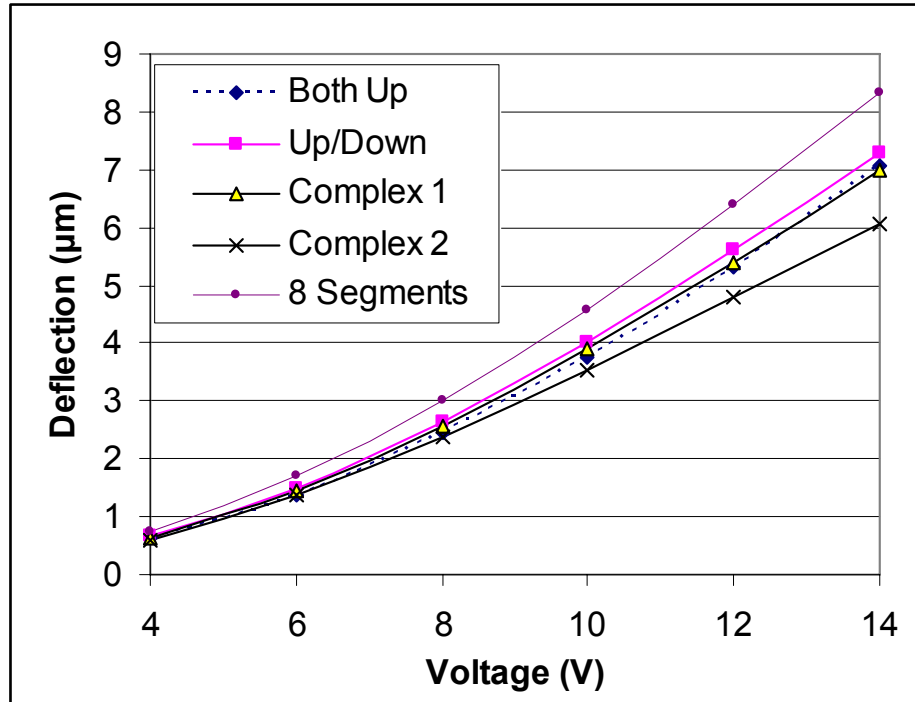


Fig. 4.15: Simulated deflection as a function of voltage of the various micro-ribbon geometries of Fig. 4.14.

The results of the simulations can be seen in Figure 4.15. There is approximately a $\pm 10\%$ range in flexibility between the complex designs; although the 8 segment geometry was obviously the most flexible and Complex 2 was the least flexible.

Another value that was worth examining was the volume of additional air added when the micro-ribbons were deflected. The volume of additional air when the ribbons are deflected is a very important parameter because the phase shift is dependent on how much air is introduced in the stacked dielectrics. The following table shows the volume of air added at 14 V. The value was acquired by integrating the deflection across the micro-ribbon from the COMSOL solution. Simulated results are shown in Table 4-12.

Table 4-12: Volume of air present above a micro-ribbon for various ribbon geometries when deflected by a 14 V potential.

Micro-Ribbon Geometry	Additional Volume of Air Added (m^3)	Maximum Deflection (m)
Both Up	3.3×10^{-13}	7.1×10^{-6}
Up/Down	3.5×10^{-13}	7.3×10^{-6}
Complex 1	3.3×10^{-13}	7.0×10^{-6}
Complex 2	2.8×10^{-13}	6.1×10^{-6}
8 Segments	3.9×10^{-13}	8.3×10^{-6}

4.7 Varying Separation Distances between Micro-ribbons

An investigation was carried out to determine the role of the separation distance between the individual micro-ribbons on the electrostatic force. Table 4-13 shows the calculated force on a micro-ribbon for various separation distances between micro-ribbons. The 3D simulations were done on straight beams that were 3 mm in length, 20 μm in width and 1 μm thick with adjacent rigid grounds (Fig. 4.16). The micro-ribbons were spaced 100 μm away from the pull-down electrode at 50 V.

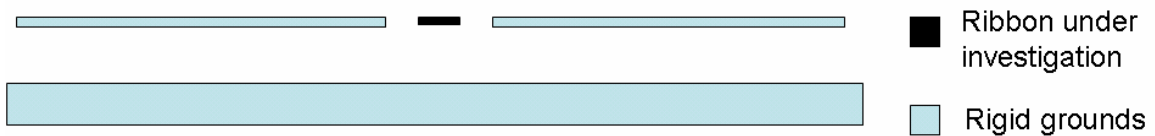


Fig. 4.16: Schematic of the 3D simulation of the micro-ribbon with adjacent rigid grounds used to determine the effect of fringing capacitance on the electrostatic force.

Table 4-13: Simulated electrostatic force between a 3 mm long and 1 μm thick micro-ribbon and a pull-down electrode as a function of inter-ribbon spacing. The electrode is 100 μm from the ribbon and is biased to 50 V.

Separation between Ribbons (μm)	Electrostatic Force (N)
5	6.7×10^{-8}
10	7.0×10^{-8}
20	8.5×10^{-8}
40	1.2×10^{-7}
80	1.8×10^{-7}

It can be seen that there is a gradual increase in the force with increasing separation between ribbons. A second more accurate set of simulations was carried out in order to more accurately simulate the real situation. A 2D simulation of 11 micro-ribbons was carried out for the geometry of Fig. 4.17.

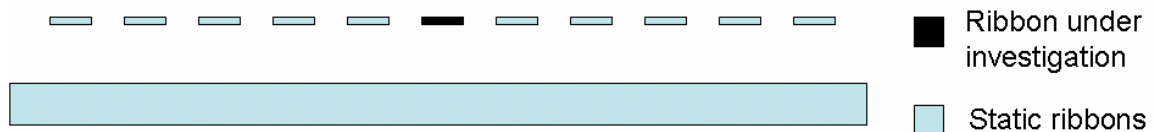


Fig. 4.17: Schematic of the 2D simulation of 11 micro-ribbons used to model the effect of the fringing capacitance on the electrostatic force in an array situation.

Having multiple micro-ribbons in the simulation ensured that the fringing capacitance was more realistically modeled. The micro-ribbons were 20 μm in width, and 1 μm thick. They were 100 μm from the pull-down electrode at 50 V. In the simulation, it was assumed that the results would only be accurate for the middle portion of the length of the micro-ribbon (Table 4-14). We can clearly see that a lower actuation voltage can be used if the ribbons are spaced further apart. A plot of this result is given in Figure 4.18.

Table 4-14: 2D simulation showing the force increase with increasing separation distance between 3 mm long and 1 μm thick micro-ribbons. Ribbons are located 100 μm from the pull-down electrode biased to 50 V.

Separation Distance (μm)	Electrostatic Force (N/m)
5	2.6×10^{-5}
10	3.0×10^{-5}
20	3.9×10^{-5}
40	5.4×10^{-5}
60	6.6×10^{-5}
80	8.2×10^{-5}
100	8.6×10^{-5}
150	1.2×10^{-4}
200	1.2×10^{-4}

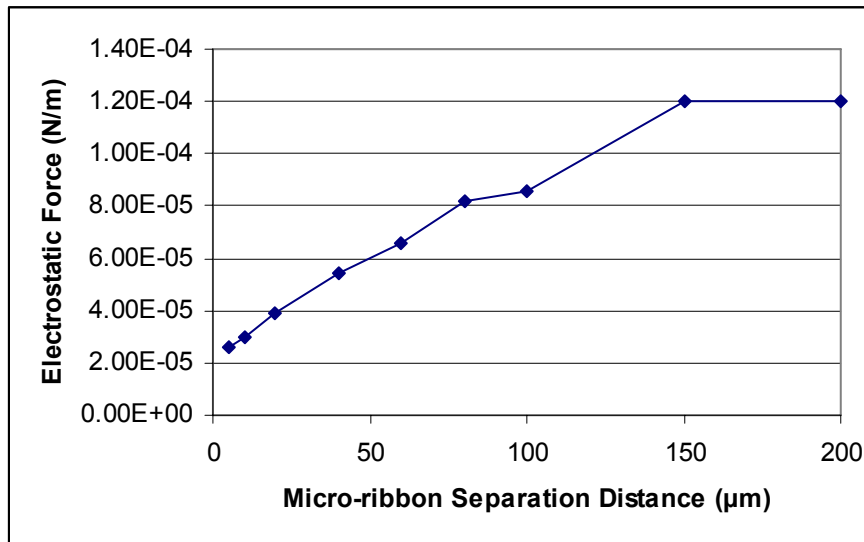


Fig. 4.18: Simulated electrostatic force as a function of micro-ribbon separation distance for 3 mm long and 1 μm thick micro-ribbon. Ribbons are located 100 μm from the pull-down electrode biased to 50 V.

4.8 Summary

This chapter of the thesis discussed the FEM simulations done using COMSOL MultiphysicsTM. For computational reasons, only one micro-ribbon was simulated with adjacent rigid ground planes to account for the fringe fields. Simulations showed that the

spring constant was proportional to the width of the ribbon. However, with equal separation distances between micro-ribbons, the thinner micro-ribbon would have a larger electrostatic force due to the effect of fringe fields. Also, it was shown through simulation that the electrostatic force increased with separation distance between micro-ribbons. Lastly, for a set span length, having a large jog angle increased the flexibility of a micro-ribbon. The number of segments in the micro-ribbon also determined the flexibility of the micro-ribbon. The most flexible case was a micro-ribbon made up of only 2 segments and the flexibility decreased with additional segments. Additional simulations in Appendix B expand on this discussion.

CHAPTER 5

FABRICATION

5.1 Overview

Micro-ribbon geometries from Chapter 4 were fabricated and observations were made about the fabricated micro-ribbon arrays. This chapter details the fabrication process of the aluminum micro-ribbons for the defected ground phase shifter. A great deal of work was done to find an appropriate etch recipe for the plasma etching process to release the micro-ribbons, so there is also a lengthy discussion of that process as well.

5.2 Fabrication Geometries

Two fabrication iterations were carried out. The first set of micro-ribbon arrays possessed micro-ribbons 20 μm wide. After fabrication and testing, it was noted that a larger phase shift could be achieved if there was a smaller air gap beneath the micro-ribbons after the release process. In an attempt to decrease this initial air gap, micro-ribbon arrays were fabricated using 5 μm and 10 μm wide ribbons.

5.3 General Fabrication

The fabrication of the micro-ribbon delay line phase shifter can be broken up into 3 main parts: fabrication of the RF substrate, fabrication of the transmission line, and fabrication of the micro-ribbon array.

5.3.1 Fabrication of the RF Substrate

The aluminum micro-ribbon array for the defected ground structure phase shifter was fabricated on a 2" high resistivity (3000-5000 Ωcm) RF silicon wafer 250 μm thick that was polished and coated with a 1.5 μm layer of silicon oxide (SiO_2) on both sides. The first step was to take the round wafer and pattern and etch it so that it became rectangular in order to fit it in the test fixture. This was done using a KOH etch (Fig. 5.1). Figure 5.1(a) shows the wafer at the initial stage. The photoresist used was HPR-504 and the developer used was Microposit-352. The mask aligner system was an ABM-6" Contact Mask Aligner with a 350 W bulb. Photoresist was deposited and patterned (Fig. 5.1(b)). The patterned location in the photoresist eventually became the etch grooves along which the wafer was broken to attain the rectangular shape. Before the

BOE etch was carried out, the back of the wafer was masked with protective tape in order to protect the silicon oxide on the back side from the solution. The exposed oxide was then etched in a buffered oxide etch (BOE), 10:1 mixture solution, for 40 minutes (Fig. 5.1(c)). Once the oxide was patterned, the photoresist was removed and the wafer was put in a 30% KOH solution for 2.5 hours at 80°C. The oxide acted as a mask in this solution while the silicon was etched away. The KOH etch resulted in a series of “V” grooves in the wafer along which the wafer was cleaved (Fig. 5.1(d)).

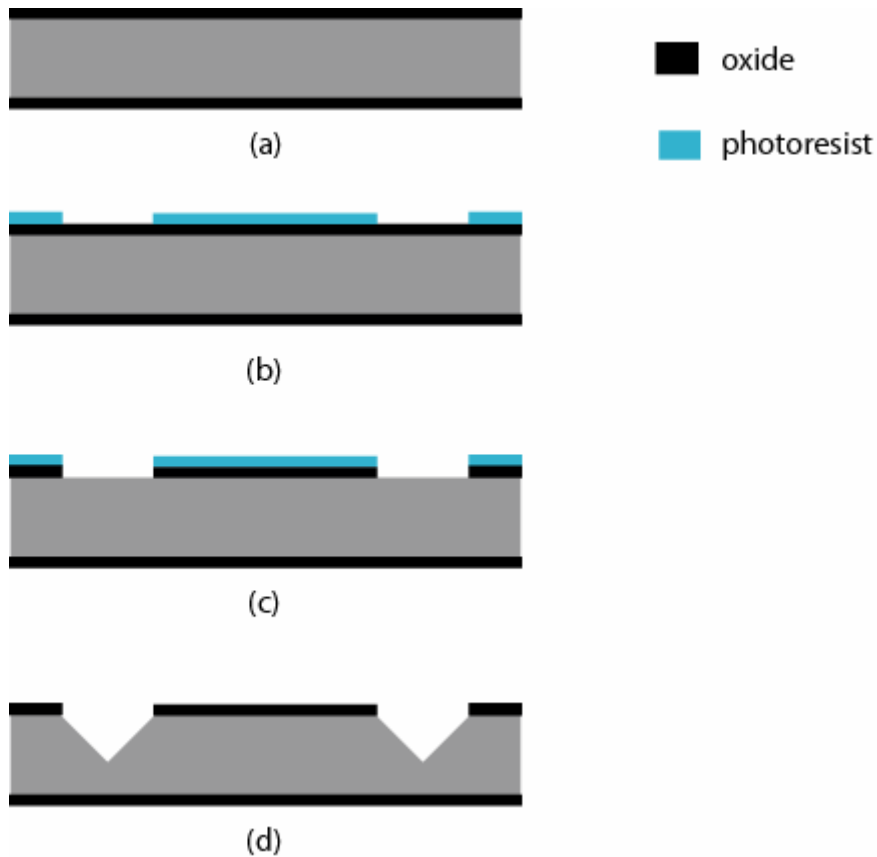


Fig. 5.1: Fabrication steps to attain a rectangular wafer from a round wafer. (a) original wafer. (b) spin on photoresist and do lithography. (c) etch the silicon oxide. (d) Etch in KOH solution to achieve the “V” grooves.

At this point, a piranha cleaning process was applied to the wafer to remove any organic materials. The piranha solution was made up of a 3:1 mixture of H_2SO_4 and H_2O_2 respectively. The wafer was allowed to soak for 5 minutes. The oxide was then stripped in a BOE etch for 1 hour. At this point, the sides of the round wafer were cleaved off, but the top and bottom were left intact to prevent the metals to be deposited for the transmission line and ground from contacting each other during the subsequent sputter deposition steps (Fig. 5.2). In the figure, the transmission lines run vertically. Three transmission lines were built onto a single wafer and under each transmission line was fabricated a set of micro-ribbons with different geometries.



Fig. 5.2: Cleaved wafer with top and bottom intact to prevent shorting of top and bottom metal deposited in subsequent sputter deposition steps.

5.3.2 Fabrication of the Transmission Line

The next step in the fabrication process was to make the transmission line on the front side of the wafer and the micro-ribbon array on the back side of the wafer (Fig. 5.3).

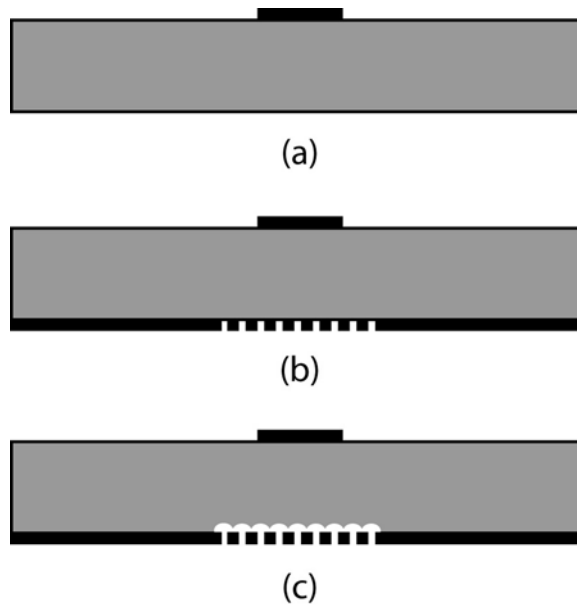


Fig. 5.3: Fabrication of the transmission line and the micro-ribbon array. (a) aluminum for the transmission is deposited and patterned. (b) aluminum for the micro-ribbons is sputtered and patterned. (c) the micro-ribbons are released using a gas etch process.

The transmission line was made by sputtering a 2 μm layer of aluminum according to the recipe found in Table 5-1. This recipe was chosen for its ability to produce micro-ribbons with low levels of internal stress. Thin film stress measurements were carried out using a Toho Technology Corporation FLX-2320-S thin film measurement system. The measured tensile stress for a 1 μm thick aluminum film was measured to be 4.3 MPa. The stress measurements were performed on a separate 4" round wafer, because the measurement system required the sample to be round.

Table 5-1: Aluminum sputtering recipe.

Parameter	Value
Pressure	16 mTorr
Ar	65 sccm
Power	200 W DC
Time	40 minutes

After the aluminum for the transmission line was sputtered, a lithography process was used to pattern the transmission line. After the lithography step, the aluminum was etched in an aluminum etch solution at 50 °C for 6 minutes (Fig. 5.3(a)).

The exposure time in the lithography step was very important in the fabrication step. It was not as important for patterning the transmission line but it was very important for patterning the thin micro-ribbons. Exposure times were varied from 10 seconds to 1 second. At the longer exposure times, the 5 μm lines for the micro-ribbons were over-exposed, which resulted in thinner than desired lines ($\sim 2 \mu\text{m}$). At a 2 second exposure time, the 5 μm lines were measured visually to be 5 μm ; however, the photoresist seemed to be under-exposed because the spaces between the micro-ribbons appeared to be cloudy. At 3 seconds, the photoresist was fully exposed but the lines were $\sim 4 \mu\text{m}$ wide. Table 5-2 shows the parameters used in the lithography process.

Table 5-2: Lithography process parameters.

Parameter	Value
Spin rate	3000 rpm
Soft bake temperature	110°C
Soft bake time	60 seconds
Rest time before exposure	5 minutes
Exposure time	3 seconds
Develop time	30 seconds
Hard bake temperature	120°C
Hard bake time	20 minutes

5.3.3 Fabrication of the Micro-Ribbon Array

The micro-ribbon array was fabricated on the back side of the wafer following completion of the transmission line on the front side of the wafer (Fig. 5.3(b)). A 1 μm

thick layer of aluminum was sputtered on the back side of the wafer for the fabrication of the micro-ribbon arrays. Next, the side of the wafer with the transmission line was coated with photoresist so that it would not be damaged. The lithography for the micro-ribbons was carried out according to the parameters found in Table 5-2. The aluminum micro-ribbons were then etched in the aluminum etch solution at 50 °C for 2.5 minutes. At this point, the wafer was examined under a microscope to determine if more etching was required. Figure 5.4 shows an example with unetched portions, which means that more etching is required. The wafer was then etched for another 30 seconds, and it was then determined that the aluminum was etched properly.

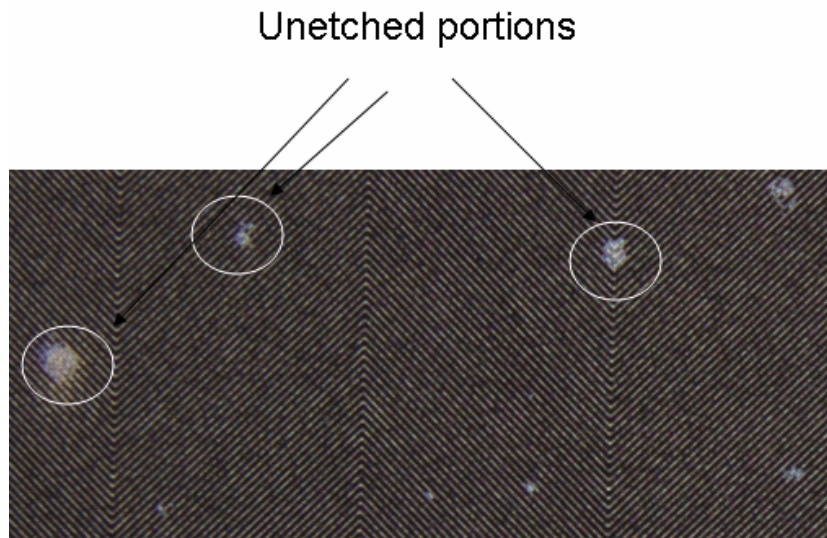


Fig. 5.4: Photograph showing unetched portions in the micro-ribbon array with 10 μm wide ribbons and 10 μm spacing.

Once the micro-ribbon array was patterned, the top and bottom tabs were broken off. A dry release process was then used to release the micro-ribbon array from the silicon substrate (Fig. 5.3(c)). After characterizing many different etch processes and recipes, a plasma etch using SF_6 gas according to the recipe found in Table 5-3 was found

to be the most suitable for releasing the micro-ribbons. Etch times were dependent on the widths of the micro-ribbons.

Table 5-3: Plasma etch parameters for dry release.

Parameter	Value
Pressure	300 mTorr
ICP power	200 W
RIE Power	30 W
SF ₆ flow rate	30 sccm

5.4 Investigation of the Dry Release Process

The release method for the micro-ribbons needed to be optimized in order to minimize the depth of silicon etched when releasing the micro-ribbons. In Fig. 1.5, it can be seen that the greatest change in the effective permittivity of the stacked dielectrics occurred at the initial stage, when the air was introduced to a stacked dielectric made completely of silicon. The shift in effective permittivity becomes less significant the more air that is added. For this reason, it was important to minimize the initial air in the stacked dielectrics. This implies using an isotropic etch to minimize the etch depth required to release the micro-ribbon.

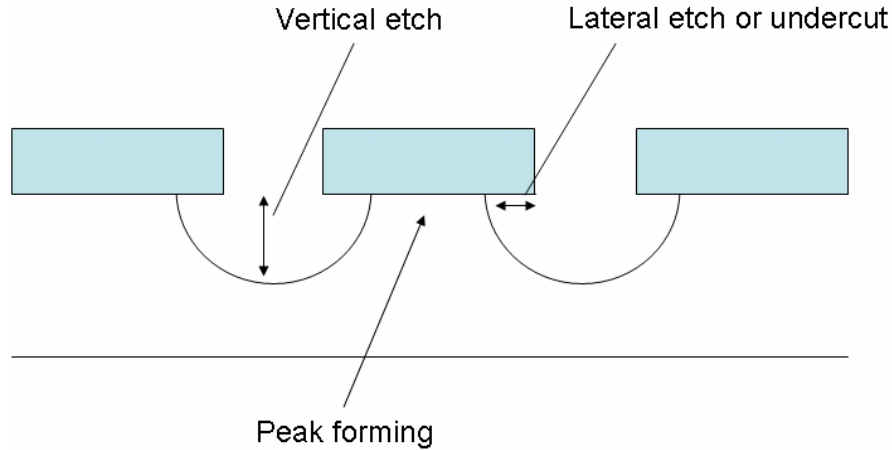


Fig. 5.5: Diagram illustrating vertical etch, lateral etch and the peak that forms underneath a micro-ribbon in an isotropic etch process.

In Figure 5.5, a few concepts relating to the etch process are illustrated. The vertical etch in an isotropic etch process refers to the depth of the etch. The lateral etch or undercut refers to the horizontal etching that occurs. In an isotropic etch, the lateral etching from both sides of the micro-ribbons will eventually form a peak. An important aspect in the dry release step was to be able to control the etch so that no further etching occurred once the micro-ribbons were released. If this could be done, there should be a peak under each micro-ribbon. With a peak under each micro-ribbon, there was less surface area for the ribbon to contact and therefore less likelihood of the micro-ribbon sticking to the substrate. Figure 5.6 shows a peak beginning to form underneath a micro-ribbon while it was being released.

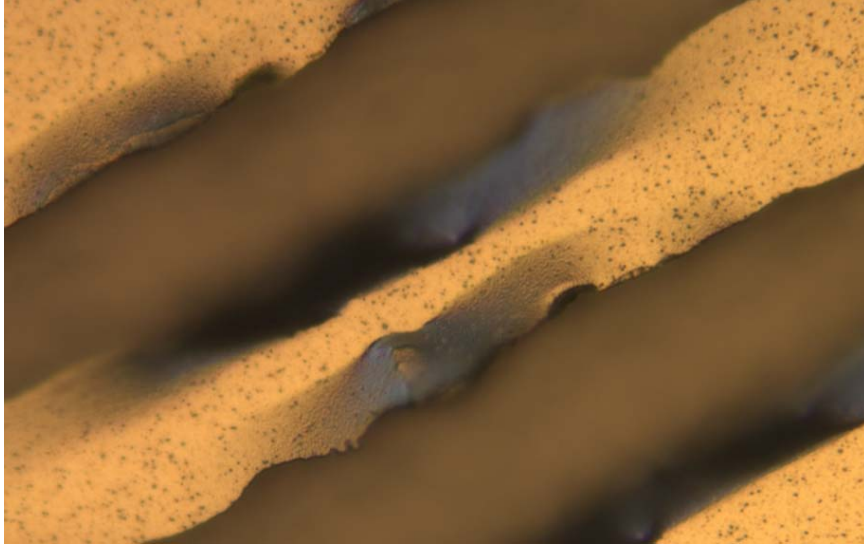


Fig. 5.6: Photo of a peak forming underneath a micro-ribbon. It can be clearly seen that the center micro-ribbon is being released and is bending over the peak.

Two dry etch processes are available at the NSFL at the University of Manitoba: XeF_2 gas and plasma gas. Both techniques were investigated in detail for this thesis.

5.4.1 Dry etch process test mask

A mask was made to test different dry etch recipes (Fig. 5.7). Experiments were conducted to study both the vertical and lateral silicon etch rates for each of the recipes. In these experiments, a silicon wafer with a 2 μm oxide coating was used. The oxide was used as the mask during the silicon etches. The oxide mask, being transparent, was necessary in order to be able to measure the undercut for each recipe since they were measured visually with a microscope. Etch depths were measured using an Alpha-Step® 500 Profiler and the oxide etch rate was measured using a Nanometrics NanoSpec 210 system.

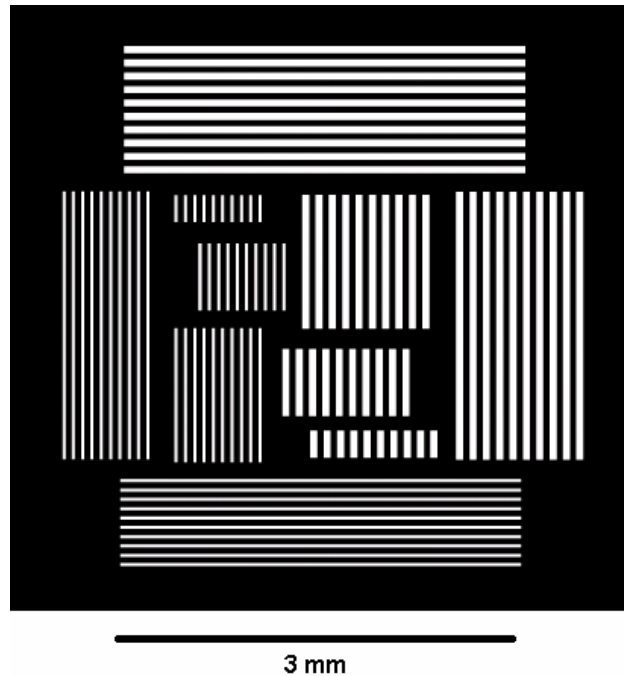


Fig. 5.7: Test pattern for testing dry release recipes.

5.5 XeF₂ Gas Etch

The gas XeF₂ is used to etch silicon and results in an isotropic etch. However, in a XeF₂ gas etch process, the gas approaches the sample from all directions and thus the edges of the etch hole etch faster (Fig. 5.8). This resulted in an etch profile where the edges were etched deeper than the center (trenching). Figure 5.9 shows the etch depths measured across the test pattern and shows that indeed, the edges of the sample have a deeper etch profile than the center. The etch profile was a result of 5 pulses of XeF₂ gas (90 seconds exposed to the gas and 30 seconds of vacuum per pulse). The apparent slope of the wafer surface was a result of the wafer being slightly inclined to the microscope stage.

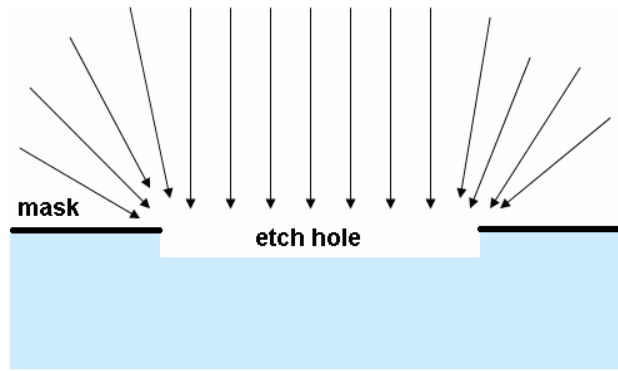


Fig. 5.8: Diagram showing that in a XeF_2 gas etch process more gas atoms can approach from the side resulting in trenching.

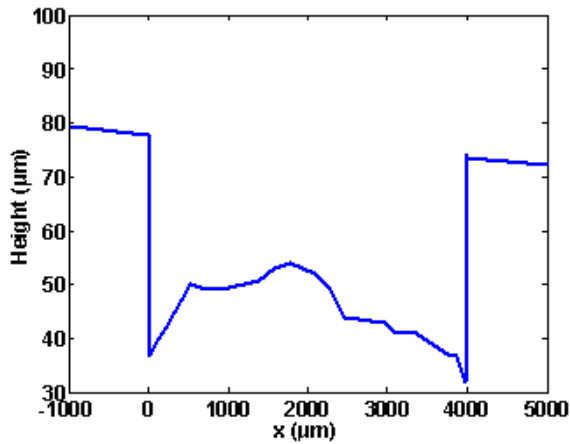


Fig. 5.9: Profile of an etched feature in an XeF_2 gas etched wafer. An etch profile that is deeper on the edges due to trenching is visible.

5.6 Plasma Gas Etch

Plasma etching the sample should yield a more uniform etch profile compared to XeF_2 because the process is done in an etch system at lower pressures, and with a gas input “shower head” that evenly inputs etch gases throughout the chamber. The NSFL has two gases available for etching silicon: CF_4 and SF_6 . Since the resulting phase shift was dependent on the initial air gap that was a result of releasing the micro-ribbons, a

recipe that had a good undercut ratio was desired. The undercut ratio is defined as follows.

$$\text{Undercut Ratio} = \frac{\text{Lateral Etch}}{\text{Vertical Etch}}$$

The gas CF_4 was chosen to do a preliminary test on the test-patterned wafer to observe the etch profile. Table 5-4 shows the recipe used. The Trion plasma etch system in the NSFL has an 8" chuck. Plasma etch systems with a different size chuck would require different power levels.

Table 5-4: Plasma etch parameters for test pattern sample.

Parameter	Value
Pressure	1000 mTorr
ICP power	500 W
RIE Power	25 W
CF_4 flow rate	45 sccm
O_2 flow rate	5 sccm
Time	15 minutes

The CF_4 recipe of Table 5-4 resulted in the the following etch profile (Fig. 5.10). The apparent slope of the wafer surface was a result of the wafer being on a slight slope on the microscope stage.

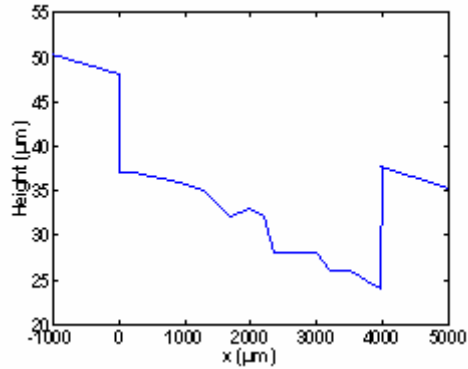


Fig. 5.10: Etch profile for plasma etched test wafer. The plasma gas etch process is a more uniform process than XeF_2 gas etching, resulting in an etch profile that is more uniform in depth.

5.6.1 CF_4 Gas Etch

A total of 5 different CF_4 etch recipes were tested. In these recipes, the CF_4 and O_2 ratios were held constant while the pressure, ICP power and RIE power were adjusted. The recipes are shown in Table 5-5, and etch results are shown in Table 5-6.

Table 5-5: Plasma etch recipes for CF_4 .

Parameter	Recipe 1	Recipe 2	Recipe 3	Recipe 4	Recipe 5
Pressure (mTorr)	200	400	200	800	1000
ICP power (W)	350	350	350	500	500
RIE Power (W)	25	25	10	25	25
CF_4 flow rate (sccm)	45	45	45	45	45
O_2 flow rate (sccm)	5	5	5	5	5

Table 5-6: Plasma etch CF_4 results.

Recipe	Si etch rate ($\mu\text{m}/\text{min}$)	Oxide etch rate ($\mu\text{m}/\text{min}$)	Undercut rate ($\mu\text{m}/\text{min}$)	Ratio (undercut:Si)
1	0.41	0.012	0.20	0.50
2	0.48	0.013	0.28	0.58
3	0.26	0.008	0.17	0.65
4	0.60	0.162	0.40	0.67
5	0.65	0.020	0.47	0.72

As can be seen from Table 5-6, recipe 5 has the best undercut to vertical Si etch ratio which means that this recipe would result in the minimum initial air gap above the fabricated micro-ribbon array.

5.6.2 SF_6 Gas Etch

A total of 13 different SF_6 etch recipes were tested. However, only the relevant recipes will be shown here. The remaining recipes and raw data for all the dry etching recipes can be found in Appendix C. In these recipes, the SF_6 flow rate was held constant while the ICP power and RIE power were adjusted. The best 5 recipes are shown in Table 5-7, and etch results are shown in Table 5-8.

Table 5-7: Plasma etch recipes for SF_6 .

Parameter	Recipe 1	Recipe 2	Recipe 3	Recipe 4	Recipe 5
Pressure (mTorr)	300	300	300	45	16
ICP power (W)	50	0	200	200	50
RIE Power (W)	50	50	30	50	50
SF_6 flow rate (sccm)	30	30	30	30	30

Table 5-8: Plasma etch SF_6 results.

Recipe	Si etch rate ($\mu\text{m}/\text{min}$)	Oxide etch rate ($\mu\text{m}/\text{min}$)	Undercut rate ($\mu\text{m}/\text{min}$)	Ratio (undercut:Si)
1	0.25	0.0006	0.33	1.3
2	0.12	0.0002	0.26	2.2
3	1.20	0.0006	0.87	0.73
4	2.80	0.029	2.00	0.71
5	1.53	0.018	1.00	0.65

Although recipes 1 and 2 had very good undercut ratios, the etches were quite slow compared to the other recipes. Also, because the undercut was measured visually

under a microscope, any uncertainty in measuring a small undercut could result in an inaccurate undercut to Si ratio. Recipes 4 and 5 also seemed to have had a good undercut to Si ratio, however, they etched the oxide faster as well. Recipe 3 was chosen to be used for the ribbon fabrication in this thesis because it had an acceptable undercut ratio and also the speed of $\sim 1 \mu\text{m}/\text{minute}$ was an appropriate speed which allowed for adequate control of etch depth.

5.7 Fabricated Micro-ribbons

20 μm Micro-ribbons:

The first micro-ribbon arrays were made of micro-ribbons that were 20 μm in width and they were fabricated underneath a 400 μm wide transmission line (37Ω). The micro-ribbons spanned a length of 3.2 mm. The jog angle was 22.5° . The geometry of the micro-ribbon can be seen in the following figure.

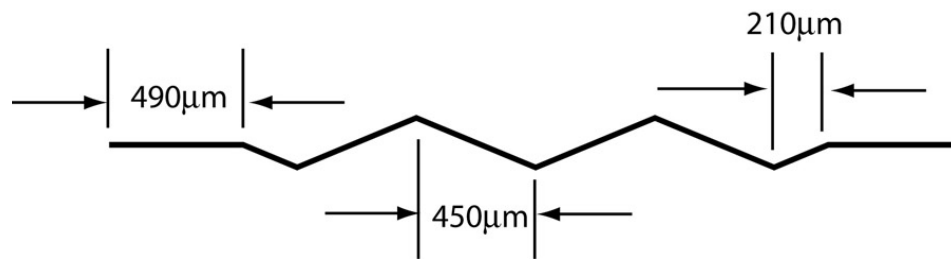


Fig. 5.11: Geometry of the 20 μm wide fabricated micro-ribbon.

XeF_2 etching was used and resulted in an initial air gap under the micro-ribbons of 20 μm at the center, but it was deeper on the edges. The micro-ribbon array was 2 mm wide. This width was selected such that the array would extend beyond the fringing field of the transmission line. The micro-ribbons had a separation distance of 70 μm in order

to take advantage of the force increase with the increase in micro-ribbon separation as studied in the simulations.

10 μm and 5 μm Micro-ribbons:

The 10 μm and 5 μm micro-ribbon arrays were also designed in order to minimize the initial air gap. With a narrower ribbon, the initial air gap would be minimized because less silicon etching is required to release the ribbons. The geometries of the 10 μm and 5 μm micro-ribbons are shown in the following figure.

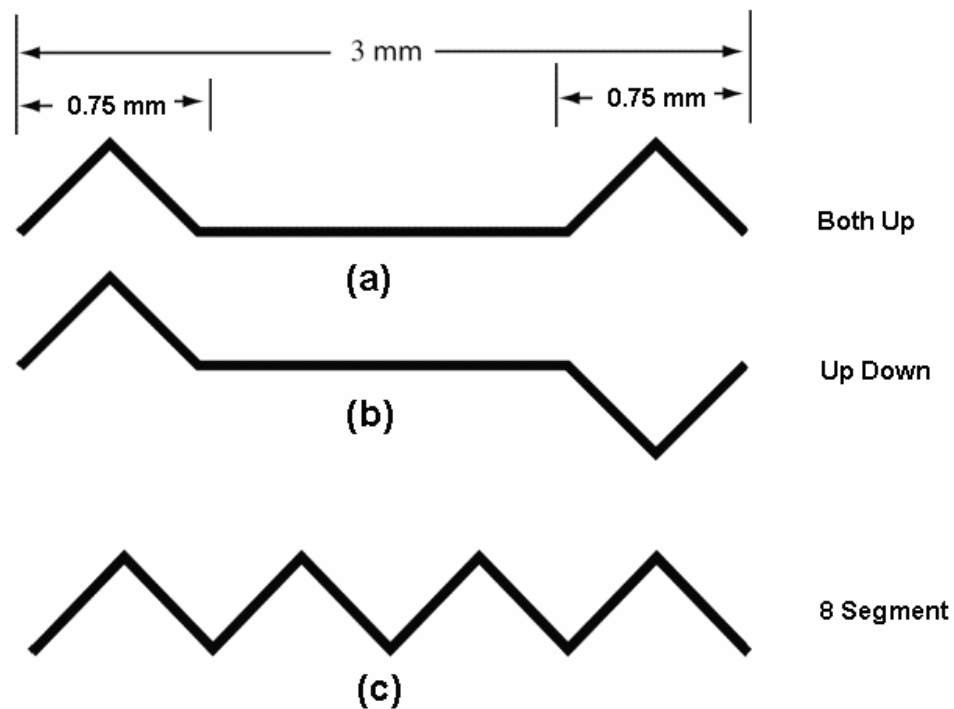


Fig. 5.12: Geometries of the 5 μm and 10 μm micro-ribbons.

In Figure 5.12, the jog angles are 45°. The simulations showed that 45° jog angles would result in more flexible micro-ribbons. The geometries found in Fig. 5.12 (a) and

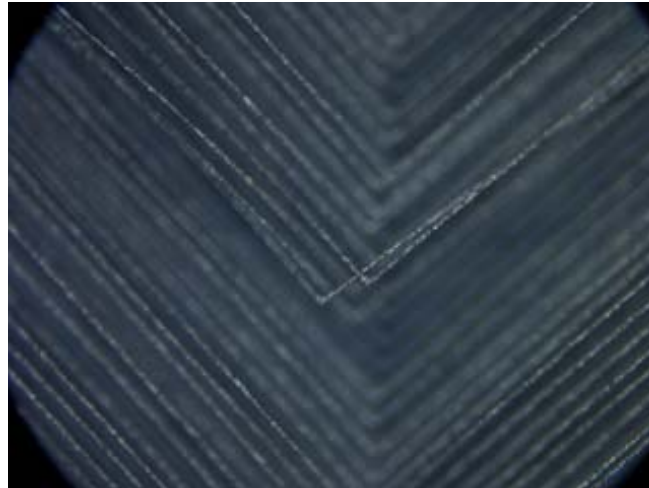
(b) will be referred to as “Both Up” and “Up/Down”, and Fig. 12 (c) will be referred to as “8 Segment”. In the geometries “Both Up” and “Up/Down”, the center straight portion is half the length of the micro-ribbon (1.5 mm). Micro-ribbon arrays were made for each of those geometries with 5 μm and 10 μm micro-ribbon widths with 5 μm and 10 μm spacings. The spacings were reduced compared to the first devices in order to minimize the air gap under the micro-ribbons when they were released. These micro-ribbon arrays were built underneath a 50 Ω transmission line (250 μm).

The SF₆-recipe 3 from Table 5-7 was used to release the micro-ribbons. A 10 minute etch was carried out to release the 10 μm wide micro-ribbons, and this resulted in an initial air gap of 10 μm . A 5 minute etch was carried out to release the 5 μm wide micro-ribbons and this resulted in a 5 μm initial air gap. The etch progress could be observed using the XeF₂ system’s microscope. It could be observed that when some micro-ribbons become released because they were no longer in plane with the other micro-ribbons (Figure 5.13) and therefore were no longer in focus in the microscope.

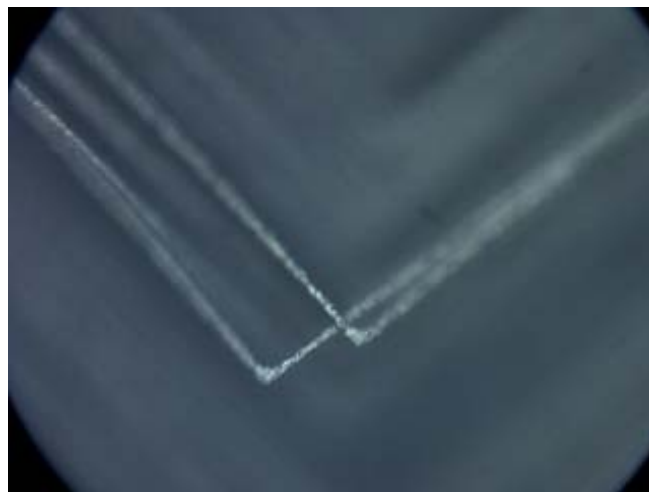


Fig. 5.13: Photograph of 10 μm wide micro-ribbons with 10 μm spacing. Released ribbons are out of plane and no longer in focus.

Once the micro-ribbons were released, the micro-ribbon arrays for the “Both Up” and “Up/Down” geometries were found to be unacceptable due to the overlapping of some micro-ribbons (Fig. 5.14). Although deposited aluminum films possessed low stress, it is hypothesized that the stress was still sufficient to deform the micro-ribbon array so that adjacent micro-ribbons overlapped each other.



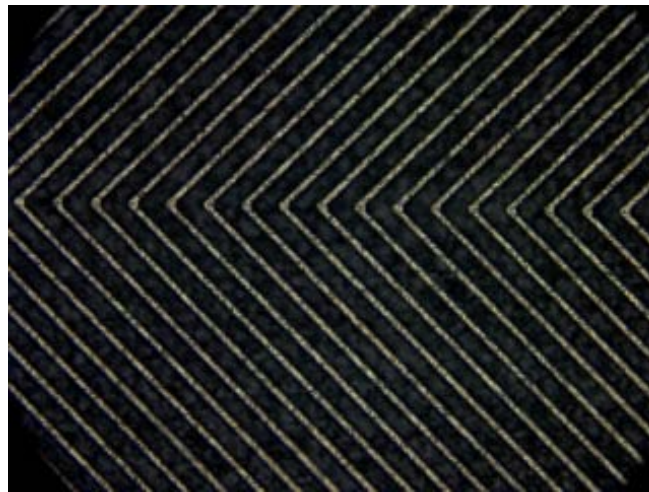
(a)



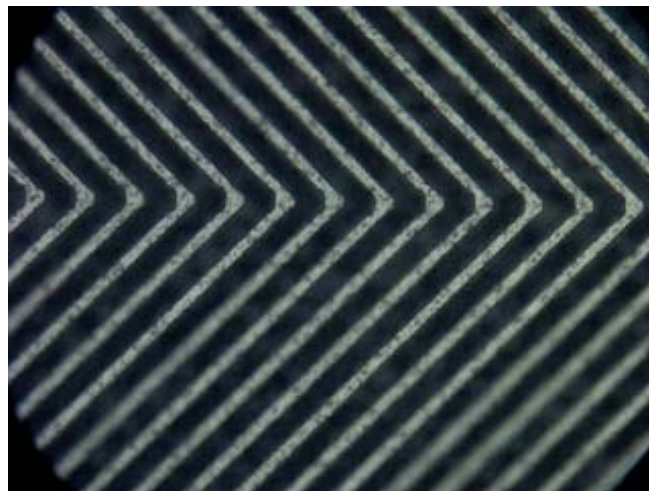
(b)

Fig. 5.14: Photographs of the 5 μm wide micro-ribbons with 10 μm spacing for the “Both Up” geometry showing overlapping micro-ribbons. (a) at 50x and (b) 100x.

As a result of these fabrication difficulties, it was decided that only the “8 segment” geometries would be tested in the phase shifter application due to the overlapping micro-ribbons in the “Both Up” and “Up/Down” geometries. Pictures of the “8 segment” geometry micro-ribbon arrays can be seen in Figure 5.15. As is seen in the figure, the quality of the 8-segment micro-ribbons appeared to be very good.



(a)



(b)

Fig. 5.15: Photographs of the “8 Segment” geometries. (a) 5 μm wide micro-ribbons with 10 μm spacing at 50x. (b) 5 μm wide micro-ribbons with 5 μm spacing at 100x.

5.8 Summary

In this chapter, the fabrication of the micro-ribbon arrays was discussed. This included a discussion of the dry release process. Three different dry release methods were tried, and it was found that a recipe that used SF₆ (recipe 3 from Table 5-7) gave the desired results of having a good uncut ratio and also a good etch rate.

Different sets of micro-ribbons were fabricated with different geometries. The first set of micro-ribbons were 20 μm wide and had an initial air gap of 20 μm with deeper air gaps on the side because it XeF₂ was used. In order to decrease the initial air gap, thinner micro-ribbons were fabricated at 5 μm and 10 μm widths. The “Both Up” and “Up/Down” geometries were fabricated but deemed not worth testing in the phase shift tests because their micro-ribbons overlapped one another. It was decided that only the “8 Segment” geometries would be tested further.

CHAPTER 6

MICRO-RIBBON DEFLECTION: TESTING AND MODEL VERIFICATION

6.1 Overview

In this chapter, the deflection measurement setup and the measurements themselves are discussed. Simulations are also presented for micro-ribbon geometries that match the actual dimensions of the fabricated micro-ribbons. The results of experimental and simulation data are compared. Finally, a discussion of thermal expansion effects is presented.

6.2 Deflection Test Setup

Measurements were carried out in order to investigate the deflection of fabricated micro-ribbons as a function of the pull-down electrode actuation voltage. Measurements were made by positioning the micro-ribbon array under a microscope and focusing on the middle of one micro-ribbon. As deflections occurred, the microscope was refocused, and the microscope micrometer was used to measure the deflection (the distance the stage had to move in order to refocus the image). Accuracy of the measurements was governed by the depth of field of the microscope objective. These measurements were accurate to $\pm 3 \mu\text{m}$, with the error due to the quality of the microscope micrometer.

Two different methods were used to measure the deflection. Since a clear view of the micro-ribbon array was required, it was necessary that the pull-down electrode not obstruct the view from the microscope. The first method that was tried was to use a piece of aluminum with a tiny hole drilled through it as the pull-down electrode. The microscope was focused through this opening in order to make the measurements. However, this technique proved very hard to execute. The second method was to use a piece of glass with a conducting surface as the pull-down electrode. The glass was 0.5 mm in thickness and had a coating of indium tin oxide (ITO) that was 150-300 Å thick. Indium tin oxide is a conducting material that is colorless and transparent in thin layers (Fig. 6.1).

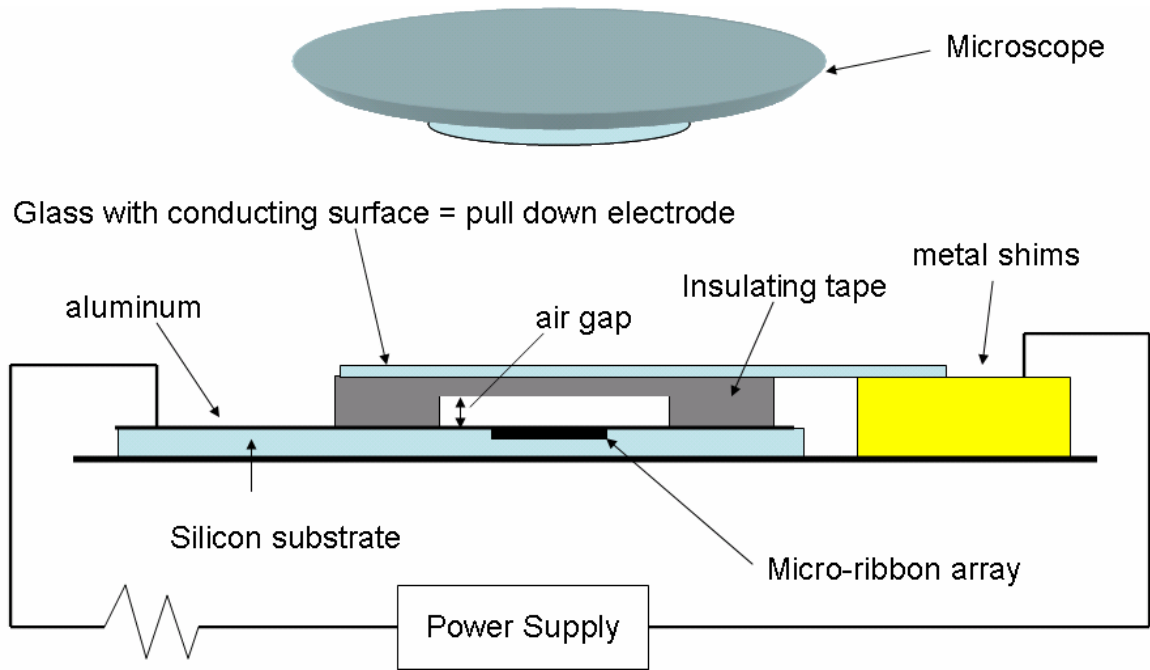


Fig. 6.1: Diagram of the deflection measurement setup showing the placement of the microscope, micro-ribbon array and the glass with a conducting surface used as the pull-down electrode.

Measurements were made with the micro-ribbons located $120\ \mu\text{m}$ from the electrode. The actual spacing for the micro-ribbon to move though was $60\ \mu\text{m}$ due to the need to insulate the pull-down electrode from the micro-ribbon. Therefore, of the $120\ \mu\text{m}$ spacing between the micro-ribbon and electrode, $60\ \mu\text{m}$ was air and $60\ \mu\text{m}$ was the insulator. Metal shims were used as a metal contact for the ITO coated glass. The power supply had a $100\text{k}\ \Omega$ resistor in series as a precaution against shorting between the grounded micro-ribbon array and the pull-down electrode, which in this case was the glass.

6.3 Deflection Measurements

Deflection measurements could only be made on the $20\ \mu\text{m}$ wide micro-ribbons. The arrays of $10\ \mu\text{m}$ and $5\ \mu\text{m}$ were too difficult to measure accurately because they were

too small to be able to focus clearly with the 0.5 mm thick ITO coated glass between the microscope and the micro-ribbons.

The results of the measurements on the 20 μm wide micro-ribbons are shown in Table 6-1. Since there were variations in etch depths and thicknesses due to the fabrication process, measurements were taken from both the left side and the right side of the array. The actuation voltage was increased by 10 V for each measurement.

Table 6-1: Deflection vs. voltage measurements for the 20 μm ribbon array. The result for the ribbons at the left and right side of the array are shown.

Voltage (V)	Left Side Deflection (μm)	Right Side Deflection (μm)
0	0	0
10	22	34
20	35	41
30	36	45
40	44	55
50	47	58
60	57	64

6.4 Simulated Deflections

The fabricated micro-ribbons spanned a distance of 3.2 mm with jog angles of 22.5°. The widths of the micro-ribbons were visually measured under the microscope and was 18 $\mu\text{m} \pm 1 \mu\text{m}$ as opposed to the design width of 20 μm . The following figure shows the geometry of the micro-ribbon.

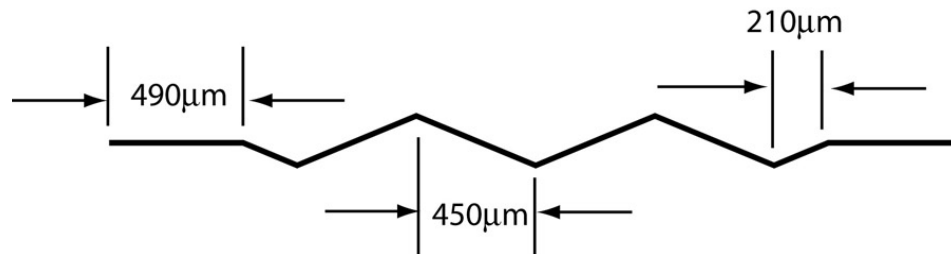


Fig. 6.2: Geometry of the simulated 20 μm wide micro-ribbon.

Simulations were carried out to model the behaviour of this design. These simulations had the micro-ribbons located 100 μm away from the pull-down electrode instead of the 120 μm as in the test setup. However, the insulating material was not included in this simulation. If the insulating material had been included, the simulated deflections would be larger due to the increase in capacitance because the permittivity of plastic is greater than that of air. The air gap between individual micro-ribbons was measured to be 70 μm and thus the simulation also modeled the air gap to be 70 μm . The first set of simulations was done without the “Large Deformation” option enabled. The results are in Table 6-2.

Table 6-2: Simulated behaviour of 20 μm wide and 1 μm thick aluminum micro-ribbons with the “large deformation” option turned off in COMSOL.

Voltage (V)	Maximum Deflection (m)	Electrostatic Force (N)	Spring Constant (N/m)
10	1.6×10^{-5}	2.0×10^{-8}	1.3×10^{-3}
12	2.3×10^{-5}	2.9×10^{-8}	1.3×10^{-3}

A second simulation was done with the “Large Deformation” enabled. The results of the second simulation are found in Table 6-3. It is clear that the first simulation, with “large deformation” off showed a much greater deflection than the second simulation but that was because it did not take into account the nonlinear behaviour of the spring force with array deflection.

Table 6-3: Simulated behaviour of 20 μm wide and 1 μm thick aluminum micro-ribbons with the “large deformation” option turned on in COMSOL.

Voltage (V)	Maximum Deflection (m)	Electrostatic Force (N)	Spring Constant (N/m)
10	9.0×10^{-6}	2.0×10^{-8}	2.2×10^{-3}
20	1.7×10^{-5}	8.0×10^{-8}	4.7×10^{-3}
30	2.4×10^{-5}	1.8×10^{-7}	7.7×10^{-3}
40	2.9×10^{-5}	3.2×10^{-7}	1.1×10^{-2}
50	3.4×10^{-5}	5.0×10^{-7}	1.5×10^{-2}
60	3.9×10^{-5}	7.2×10^{-7}	1.9×10^{-2}

6.5 Comparison of Simulated and Measured Results

The following shows the results of the simulated and the measured deflections on the same graph.

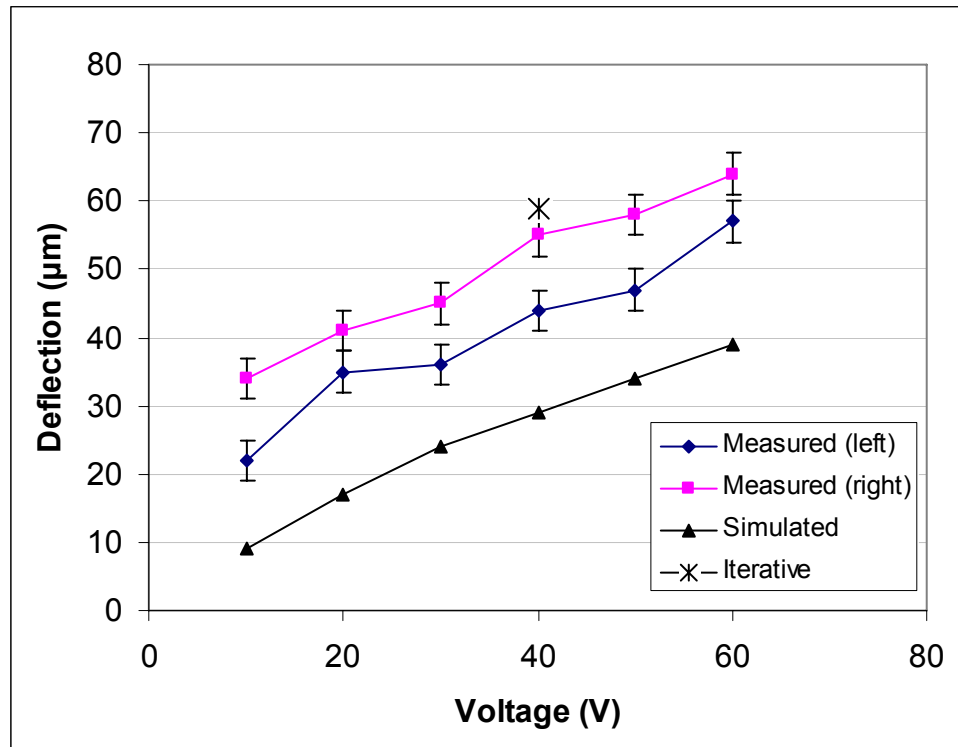


Fig. 6.3: Graph showing the simulated and measured deflections of the 20 μm ribbon array showing both the left and right side measurements with error bars due to the microscope micrometer.

As can be seen in the Figure 6.3, the simulation deflections were lower than the measured deflections. It should be noted that the simulations were actually under-predicting ribbon motion when there was significant deflection because it was not recalculating the electrostatic force as the ribbon got closer to the electrode.

In order to more accurately simulate ribbon motion, iterative simulations were done. These simulations modeled the necessary force to deflect the ribbons. The following graphs show the force vs. deflection (Fig. 6.4) and the force vs. voltage for varying ground heights (Fig. 6.5). The data point labeled “Iterative” on Figure 6.3 was obtained by using the graphs in Figures 6.4 and 6.5. The deflection at 40 V was arbitrarily selected for the iterative calculations. At 40 V, the force can be found on Figure 6.5 and this force can then be used to find the corresponding deflection on Figure 6.4. The new distance to the ground can be used again to find the corresponding force and so on. The “iterative” solution for the deflection at 40 V, is $\sim 59 \mu\text{m}$. The result of these iterative simulations is in closer agreement to the measured results for the fabricated micro-ribbons.

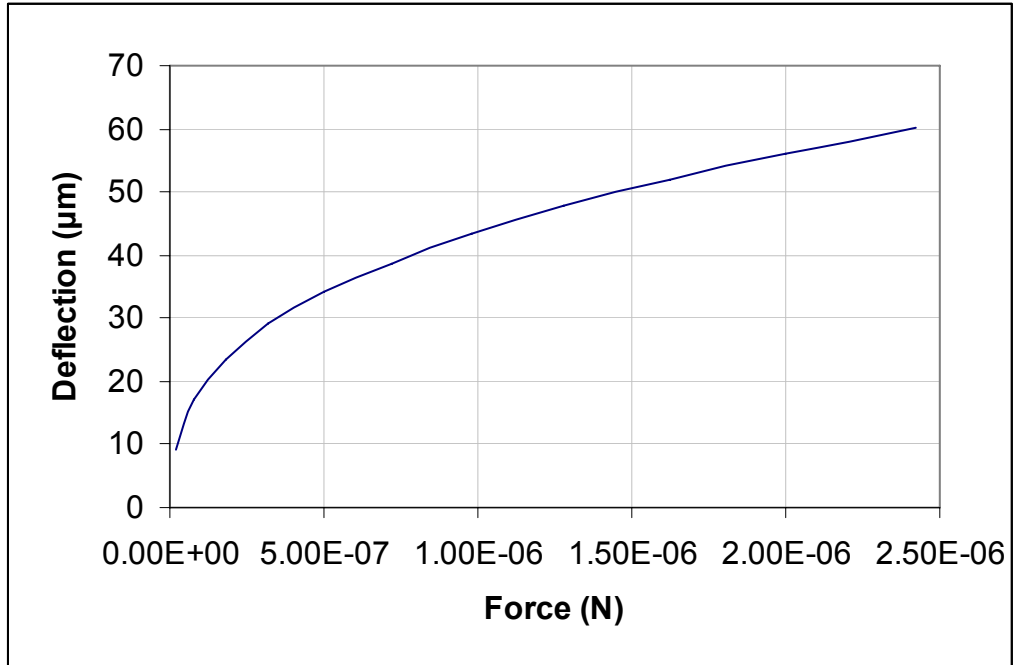


Fig. 6.4: Simulated force required for a specific deflection at the center for the 20 μm wide micro-ribbon fabricated from 1 μm thick aluminum.

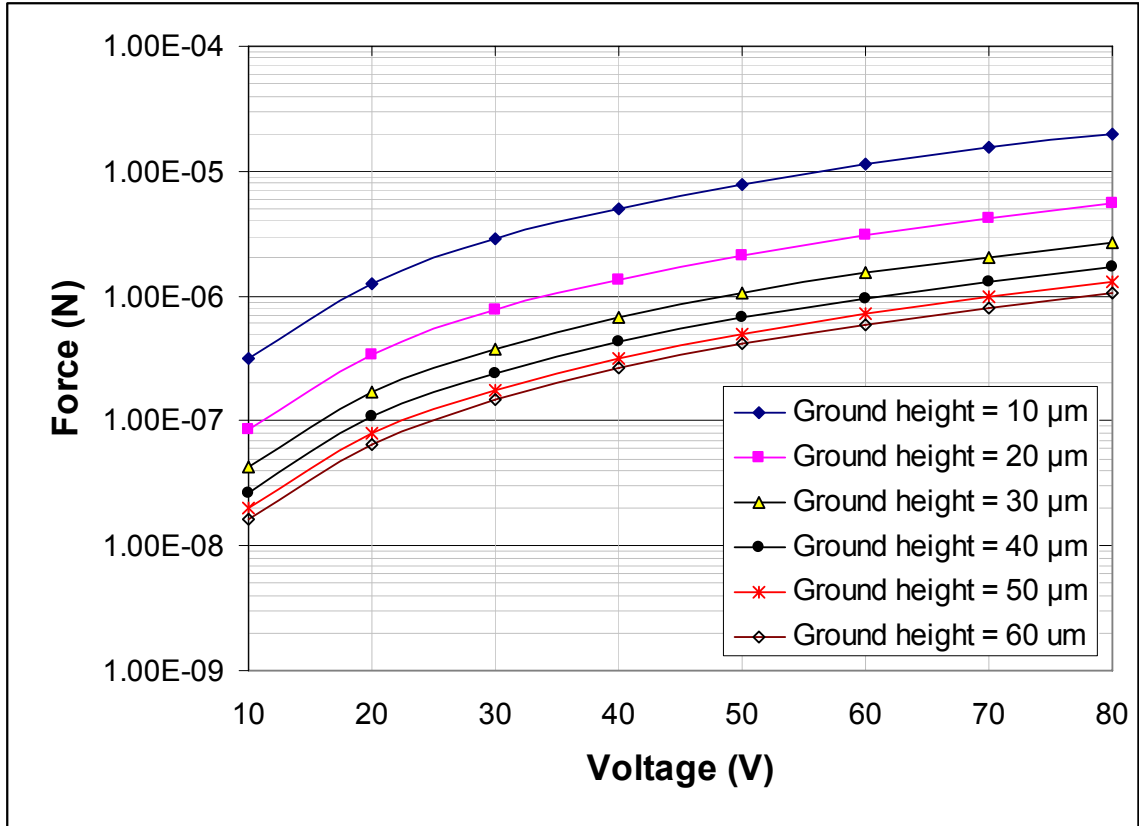


Fig. 6.5: Simulated force as a function of actuation voltage for the 20 μm wide micro-ribbons at varying ground heights.

Resonant Frequency:

The resonant frequency was also extracted from the simulations (Table 6-4). The spring constant and resonant frequencies of the micro-ribbons vary significantly as a function of their deflection. This is because the ribbons were fixed at both ends. At rest the micro-ribbon was simulated in COMSOL to exhibit a spring constant of 1.2×10^{-3} N/m and a resonant frequency of 430 Hz. However, under application of $0.5 \mu\text{N}$ evenly distributed force, the deflected micro-ribbon was simulated to have a maximum deflection of $34 \mu\text{m}$ at its center. The resulting spring constant was 1.5×10^{-2} N/m and the resonant frequency was 1500 Hz. The resonant frequency of the micro-ribbons affects how quickly the micro-ribbon deflections can be changed in order to achieve different

phase shifts. The resonant frequency of the micro-ribbons does not refer to the frequency of the signal on the transmission line.

Table 6-4: Calculated resonant frequency for the 20 μm wide, 3 mm long, and 1 μm thick aluminum micro-ribbon at different deflections.

Maximum Deflection (m)	Electrostatic Force (N)	Spring Constant (N/m)	Resonant Frequency (Hz)
1.5×10^{-9}	1.8×10^{-12}	1.2×10^{-3}	400
9.0×10^{-6}	2.0×10^{-8}	2.2×10^{-3}	600
1.7×10^{-5}	8.0×10^{-8}	4.7×10^{-3}	800
2.4×10^{-5}	1.8×10^{-7}	7.7×10^{-3}	1100
2.9×10^{-5}	3.2×10^{-7}	1.1×10^{-2}	1300
3.4×10^{-5}	5.0×10^{-7}	1.5×10^{-2}	1500
3.9×10^{-5}	7.2×10^{-7}	1.9×10^{-2}	1700

6.6 Thermal Expansion Effects on the Micro-Ribbon Array

A calculation was carried out to investigate the effect thermal expansion would have on the micro-ribbon array. When the micro-ribbons are heated, the aluminum will expand according to [8]:

$$\Delta L = L \alpha_L \Delta T \quad (6.1)$$

where L is the length of the micro-ribbon, ΔL , is the change in the length due to thermal expansion, $\alpha_L = 2.5 \times 10^{-5}/\text{K}$ for thin film aluminum is the linear thermal expansion coefficient, and ΔT is the change in absolute temperature. The software package COMSOL can be used to model thermal expansion. However, without any applied forces, the simulation cannot accurately model in which direction the micro-ribbon would deflect (toward the substrate or away from the substrate). It would be fair to assume that

most, if not all, of the thermal expansion would occur in the plane of the array because that is how the hinges/bends in the micro-ribbon were designed to deflect.

It is interesting to calculate the worst case scenario where the micro-ribbon deforms entirely in the vertical direction, even though the thermal expansion is likely to take place in the horizontal direction.

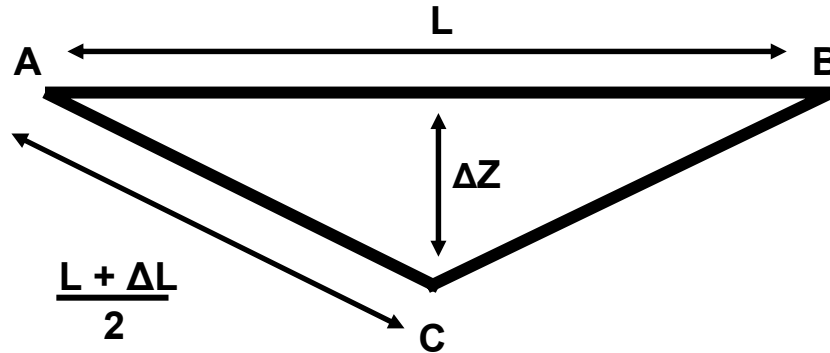


Fig. 6.6: Illustration of worst case deflection in z direction due to thermal expansion of the micro-ribbon.

As shown in Figure 6.6, the original micro-ribbon spans the length, L , from A to B. However, when there is a change in temperature, the worst case for deflection is having no deformation in the horizontal direction and only deflection in the vertical direction. This is the case where the micro-ribbon is defined by A-C-B, and the maximum vertical deflection is ΔZ , which is determined easily with Pythagoras' theorem. Further investigation would have to be carried out to determine how the micro-ribbon geometry will change due to thermal expansion. This calculation was just to illustrate the worst case scenario even though the micro-ribbon was more likely just to buckle rather than bend according to Figure 6.6.

For thin film aluminum, $\alpha_L = 2.5 \times 10^{-5}/K$ [8], and assuming a straight micro-ribbon of 3 mm, the following table of deflections results.

Table 6-5: Thermal expansion deflections for 3 mm long, 1 μm thick aluminum micro-ribbon assuming all deflection in the z direction.

Temperature ($^{\circ}\text{C}$)	ΔL (μm)	Δz (μm)
20	0	0
25	0.375	24
30	0.750	34
50	2.250	58

It should be noted that for the case in which the temperature increases by just 5 $^{\circ}\text{C}$, the micro-ribbon becomes 0.375 μm longer which results in a deflection of 24 μm . If the pull-down electrode is 120 μm away from the micro-ribbon, it means that a fifth of the air gap (~ 24 μm) is now unusable to achieve a phase shift. Figure 6.7 shows the deflection of the micro-ribbon for the out of plane deflection worst case scenario from 20-50 $^{\circ}\text{C}$.

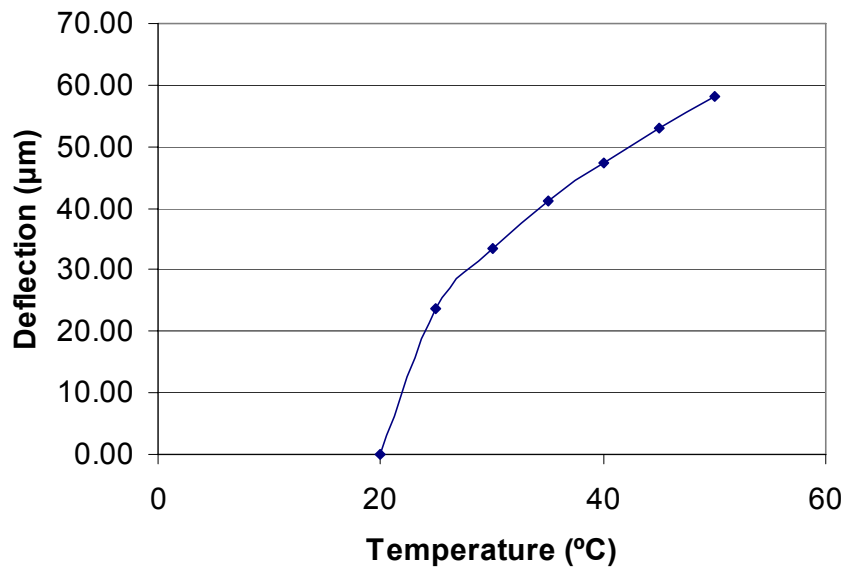


Fig. 6.7: Deflection caused by thermal expansion of a 3 mm long, 1 μm thick aluminum micro-ribbon assuming all deflection is in the z direction.

Again, in practice, the thermal expansion of the micro-ribbon would not all be in the vertical direction. It is fair to expect that most of the expansion will occur in the plane of the micro-ribbons under normal operations.

6.7 Summary

Deflection measurements were carried out using a micrometer on an optical microscope and ITO coated glass as the pull-down electrode. Only the 20 μm wide sets of micro-ribbons were large enough to actually carry out the deflection tests by this technique, the others being too small to be brought reliably into focus with the microscope.

CHAPTER 7

PHASE SHIFT TESTING AND MODEL VERIFICATION

7.1 Overview

This chapter begins with a discussion of the phase shift simulations carried out using the simulating program HFSS. Simulations were carried out to determine the expected phase shift for specific deflections. Then phase shift measurements were performed for the 20 μm wide micro-ribbons as well as the “8 Segment” 5 μm and 10 μm wide micro-ribbons. Finally, the measured results were compared with the simulated results.

7.2 RF Background

A generic 2-port RF network is shown in Figure 7.1. Port 1 is referred to as the input port and V_1 is the input voltage. Port 2 is referred to as the output port and V_2 is the output voltage. The parameter a_1 is the port 1 incident voltage wave; b_1 is the port 1 reflected voltage wave.

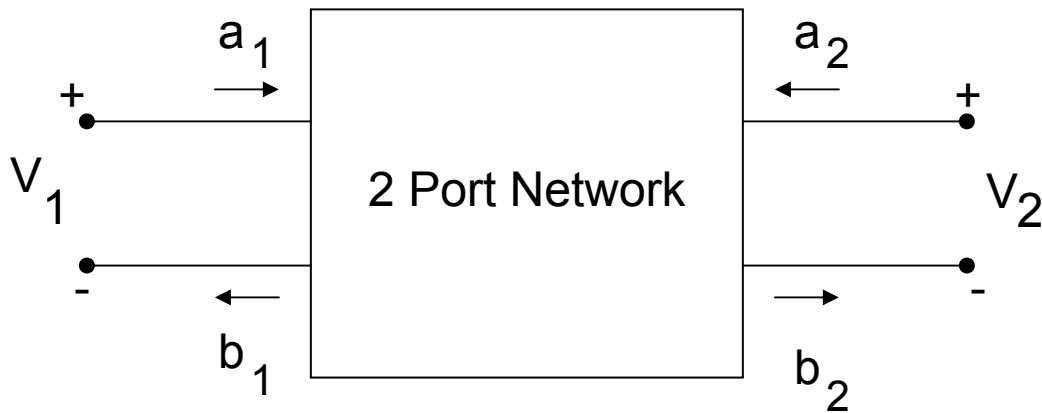


Fig. 7.1: A generic 2-port RF network indicating the input and output port voltages.

A 2-port RF network can be categorized by its 4 scattering parameters: S_{11} , S_{12} , S_{21} , and S_{22} . The parameter S_{11} is the ratio of b_1 and a_1 . The S_{11} value, sometimes referred to as the return loss, in the scattering matrix represents the proportion of the incident voltage wave that is reflected back to port 1. Ideally, for a good transmission line, S_{11} should be zero which indicates there are no signal reflections occurring at the input port and all the signal power is entering the network. The S_{21} value, sometimes referred to as the insertion loss, is the ratio a_2 to b_1 . This represents the proportion of the voltage wave that is transmitted to port 2 from port 1.

7.3 HFSS Simulations Setup

Phase shift simulations were carried out using the program HFSS [7] to determine the expected phase shifts with specific deflections. HFSS which stands for High Frequency Structure Simulator is a commercial finite element method solver for electromagnetic structures. The simulation model was simpler than the actual device in order to facilitate the computer aided drawing (CAD) as well as to decrease computational time. The individual micro-ribbons were not simulated. Instead, a flat rectangular membrane was simulated. It has been reported in [21] that the electrical similarity between a solid membrane and a micro-ribbon array means that a simulation using a solid membrane can be used. In [21], in one case a flat membrane was simulated and in the other case, an array of straight micro-ribbons that were 42 μm wide with a 42 μm wide spacing was simulated. Phase shift and Figure-of-Merit agreed well. However, with the meandering micro-ribbons presented in this thesis, the path length is larger than for straight ribbons and therefore a slight increase in line loss would be expected. Also, the simulations would give an over estimation of the phase shift since they assume a uniform deflection of the membrane. In reality, however, the micro-ribbon would not have a uniform deflection. The center of the micro-ribbon would be deflected more than the ends because the ends are fixed.

In this thesis, the geometry of Figure 7.2 was simulated in HFSS. These simulations were used to investigate the effect of having initial air gaps of different thicknesses and also to investigate different line impedances that were not considered in [21]. A rectangular flat membrane with $L_m = 3 \text{ mm}$ and $W_m = 2 \text{ mm}$ was used. The

silicon substrate ($\epsilon_r=11.9$, $\rho=0.001\Omega\text{-cm}$) had dimensions of $L = 6 \text{ mm}$ and $W = 10 \text{ mm}$ and thickness of $250 \mu\text{m}$ and L_f , the feed line length was 1.5 mm .

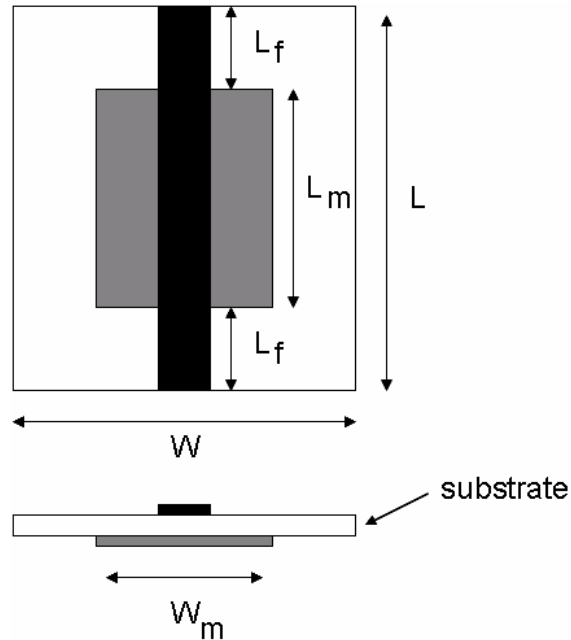


Fig. 7.2: Simulation geometry for the flat membranes in HFSS.

These simulations were carried out to model the case of having a non- 50Ω feed line and also a non- 50Ω membrane. The mesh size was optimized by HFSS for a center frequency of 50 GHz . This frequency was chosen because it was within the range of the highest frequency that accurate measurements could be conducted in the laboratory.

7.4 Transmission Line Design

There are two issues that need to be considered when designing the transmission line. The first issue is that the impedance of the transmission line will change with deflection of the micro-ribbon array. Consider, for example, a 37Ω transmission line

over a deflecting membrane. Figure 7.3 shows the simulated line impedance as a function of deflection for a line that is initially a 37Ω line with no deflection.

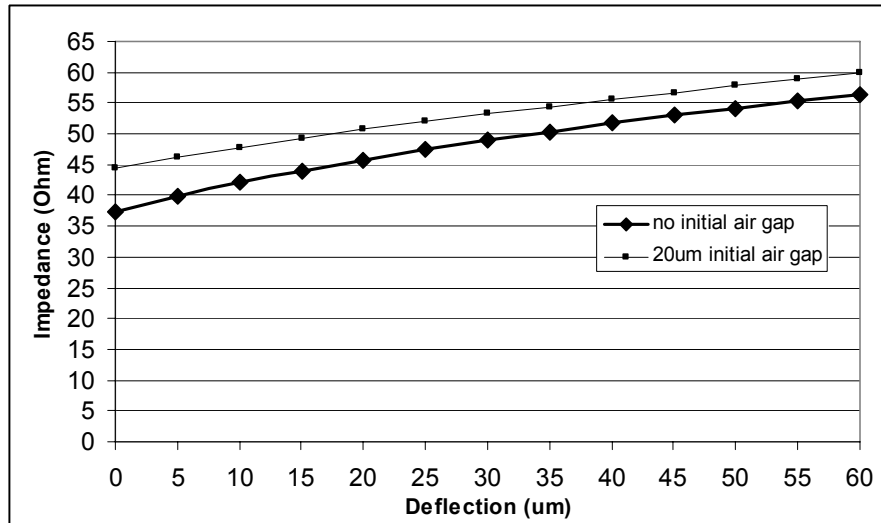


Fig. 7.3: Line impedance vs. deflection for a 37Ω transmission line for the case of having no initial air gap and $20 \mu\text{m}$ initial air gap due to the ribbon release process [22].

As can be seen in the above figure, the transmission line impedance increases (becomes more inductive) with deflection because the capacitance of the line decreases. For the case of no initial air gap, the transmission line impedance starts at 37Ω line, but with $60 \mu\text{m}$ of deflection, the transmission line impedance becomes 56Ω . When there is a mismatch between the line impedance of the feed line and the line impedance of the micro-ribbon array segment, reflections occur at the interface and the signal quality is reduced.

The second issue was that the air gap formed in the fabrication process while releasing the micro-ribbons (as mentioned in section 5.7) affects the potential maximum phase shift achievable. This is because the largest gradient change in ϵ_{eff} occurs for air

gaps close to 0 μm . For the case of the 20 μm wide micro-ribbons the initial air gap in the center of the array was 20 μm . Simulations were carried out to investigate the effect of the 20 μm initial air gap. The results are shown in Figure 7.4. In the “no initial air gap” case, the silicon substrate was 250 μm thick, and air was introduced in the stacked dielectric by uniformly deflecting the flat membrane 10 μm for each simulation. In the 20 μm initial air gap case, the silicon substrate was 230 μm thick and a 20 μm thickness of air was present at zero deflection. Any deflection of the flat membrane added to the initial air gap.

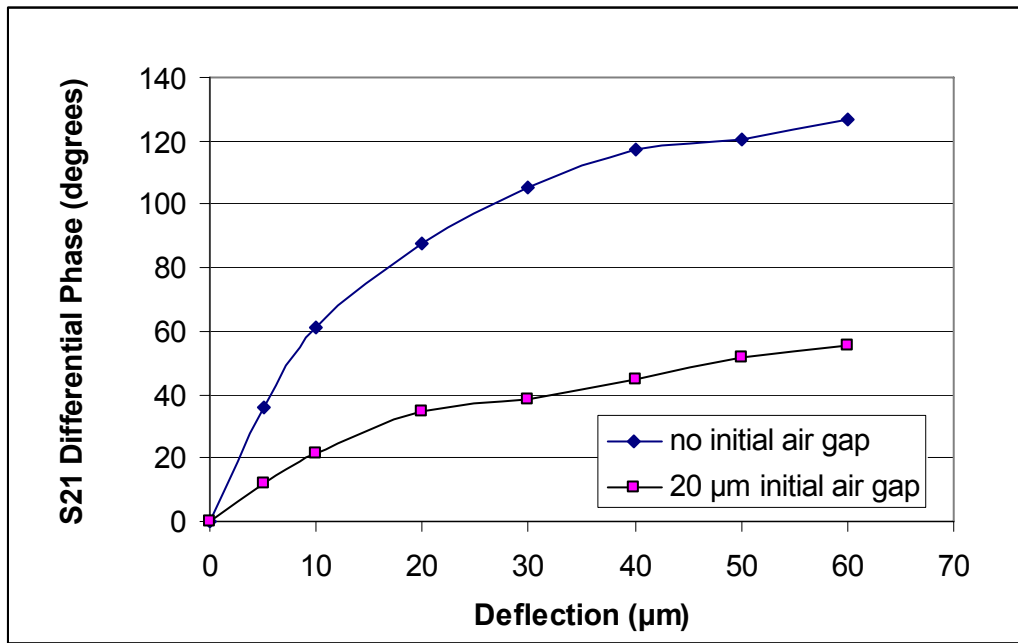


Fig. 7.4: HFSS simulation results showing the expected phase shift vs. deflection for a fabrication process with no initial air gap and an initial air gap of 20 μm at 50 GHz for a 3 mm long membrane.

As can be seen in the figure, the initial air gap that was a result of the fabrication process substantially reduced the corresponding phase shift for a given deflection. In the case where there was no initial air gap, a deflection of 20 μm caused $\sim 90^\circ$ phase shift. In the case where there was an initial air gap of 20 μm , a 20 μm deflection only caused a 35°

phase shift. At 60 μm deflection, the difference between the two cases was $>60^\circ$. Therefore, it is important to start off with a minimal air gap. Appendix D contains further HFSS simulations not discussed in this chapter.

7.4.1 Transmission Line of $37\ \Omega$

Consider the case of a $37\ \Omega$ transmission line. This line would measure 380 μm wide for a 250 μm thick silicon wafer. The S_{11} and S_{21} values were simulated for a 6 mm long line over a 250 μm thick silicon wafer. The results are shown in Figure 7.5 and 7.6 for frequencies ranging from 30 GHz – 70 GHz.

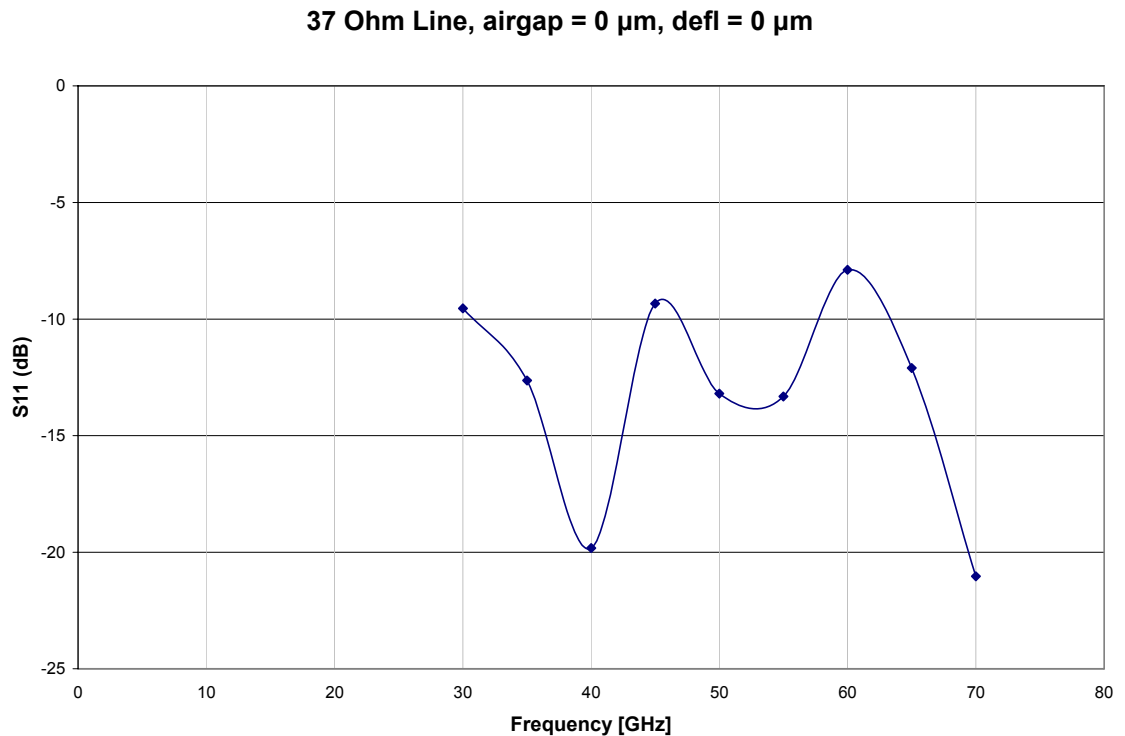


Fig. 7.5: Simulated S_{11} magnitude for a $37\ \Omega$ line for a 6 mm long line and 3 mm long membrane.

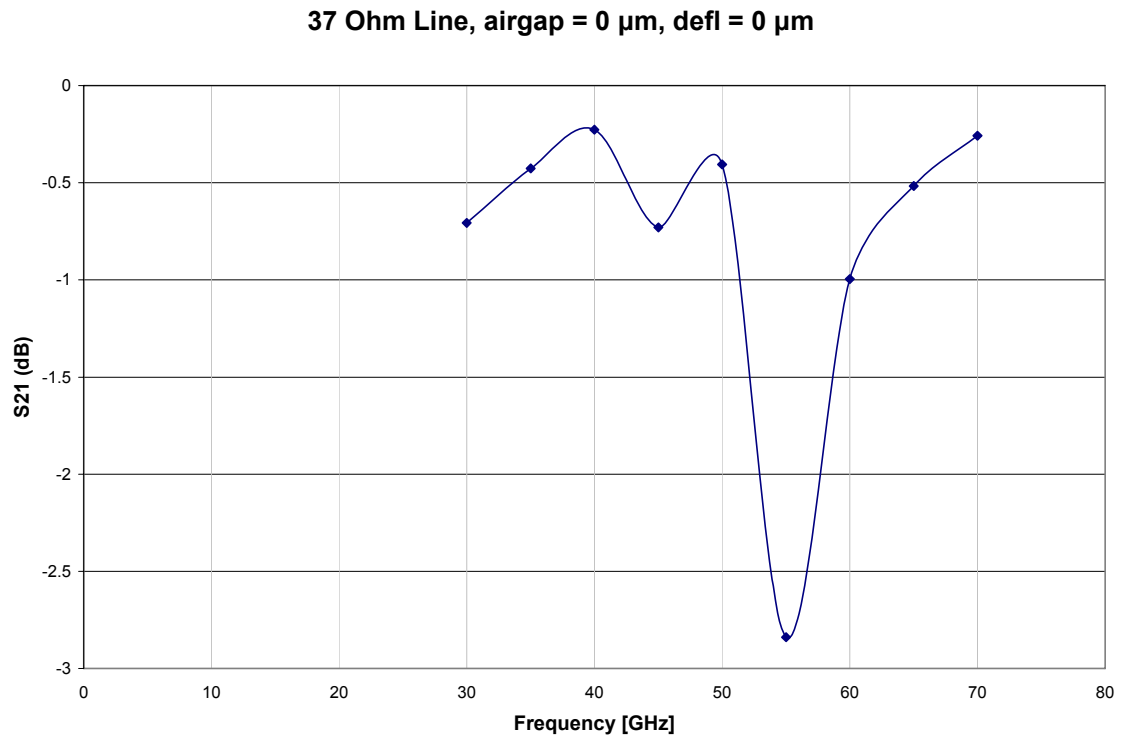


Fig. 7.6: Simulated S_{21} magnitude for a 37 Ω line for a 6 mm long line and 3 mm long membrane.

A plot of the simulated S_{11} at 50 GHz for the 37 Ω line as the membrane is deflected is shown in Figure 7.7 for various air gap thicknesses. The change in impedance matching can clearly be seen in the S_{11} plot as the membrane is deflected. For the 0 μm air gap case, note how the line impedance increased as the membrane was deflected and matched 50 Ω around 5 μm of deflection.

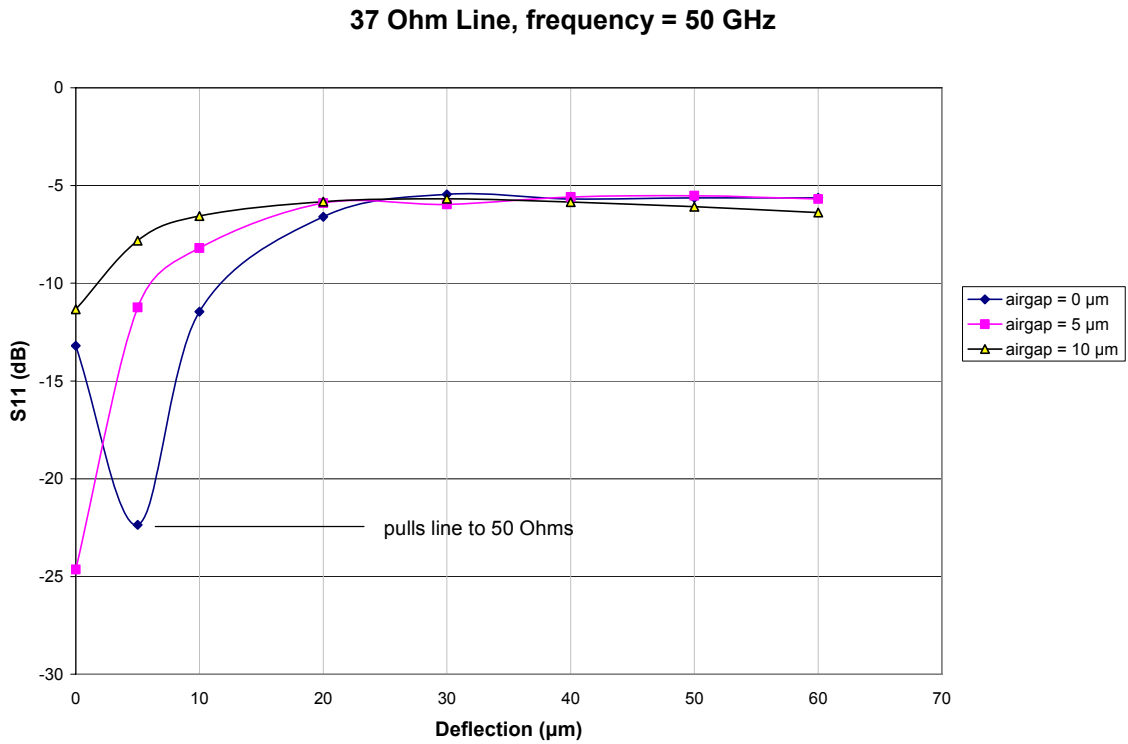


Fig. 7.7: S_{11} magnitude for a 37Ω line at 50 GHz. Note how with membrane deflection, the line impedance increases and is matched at 50Ω around $5 \mu\text{m}$ deflection.

Figure 7.8 and Figure 7.9 show the S_{21} differential phase and the magnitude as a function of deflection for 0, 5 μm , and 10 μm initial air gaps. True line impedance of 37Ω only applied to the case when there was no initial air gap. With increasing air gap, the line impedance increased. There was significant phase shift potential if the air gap can be minimized. S_{21} values increased more slowly for the larger deflections.

37 Ohm Line, frequency = 50 GHz

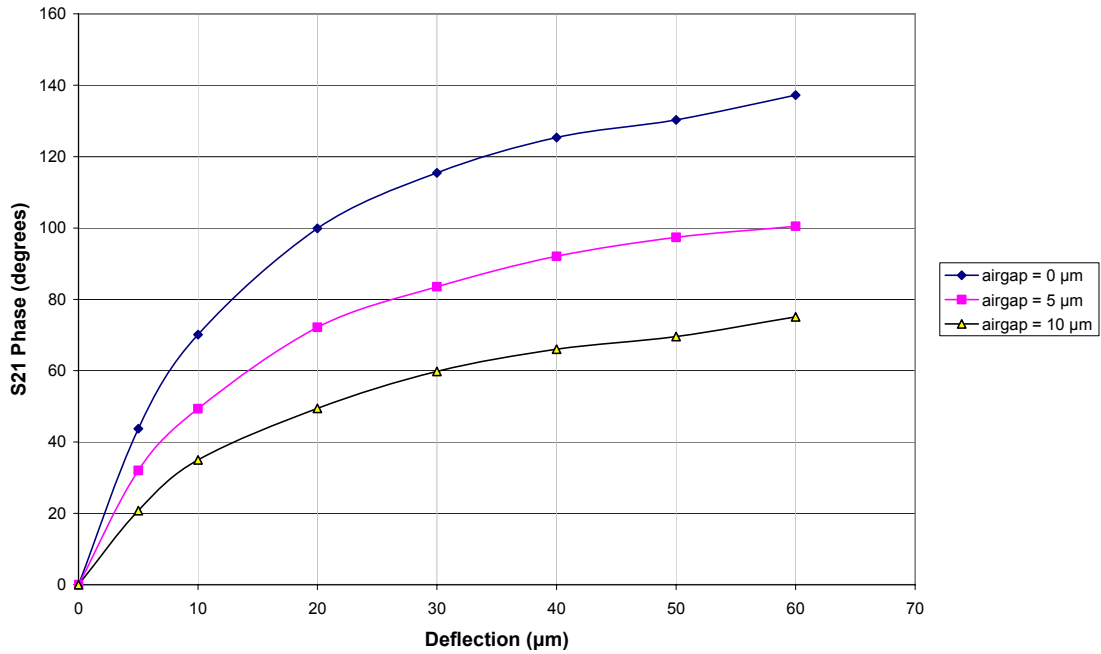


Fig. 7.8: Simulated differential S₂₁ phase for a 37 Ω line for different air gaps vs. deflection at 50 GHz.

37 Ohm Line, frequency = 50 GHz

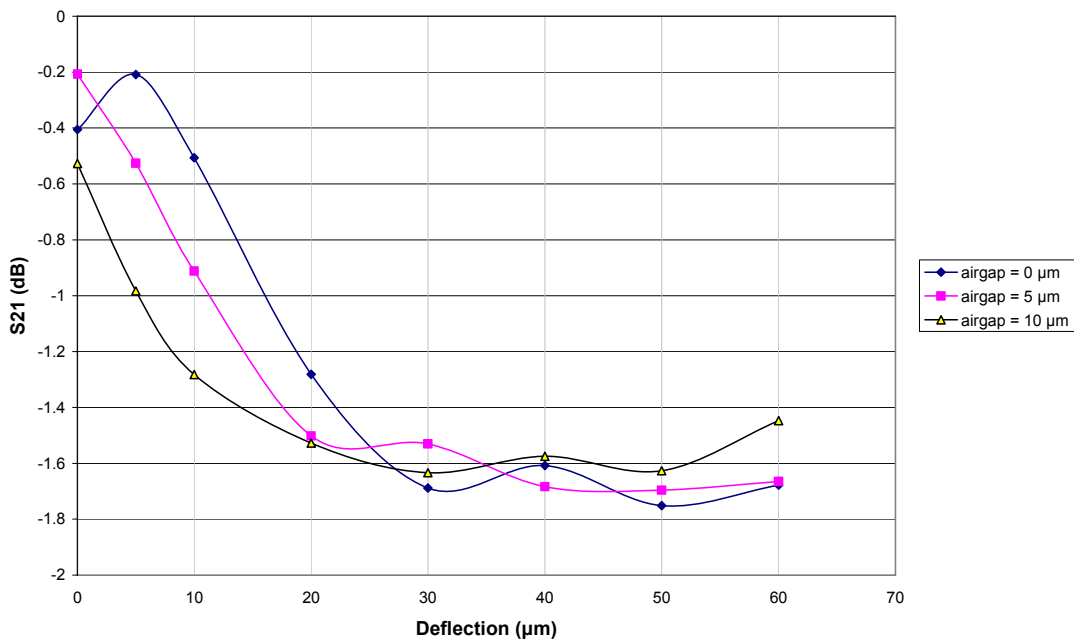


Fig. 7.9: Simulated S₂₁ magnitude for a 37 Ω line for different air gaps vs. deflection at 50 GHz.

7.4.2 Transmission Line of 50Ω

Consider the case of a 50Ω transmission line. This line would measure $250 \mu\text{m}$ wide when over a $250 \mu\text{m}$ thick silicon wafer. The simulated S_{11} and S_{21} can be seen in Figures 7.10 and 7.11 for a range of frequencies from 30 GHz – 70 GHz, for a 50Ω line 6 mm long with a 3 mm long membrane.

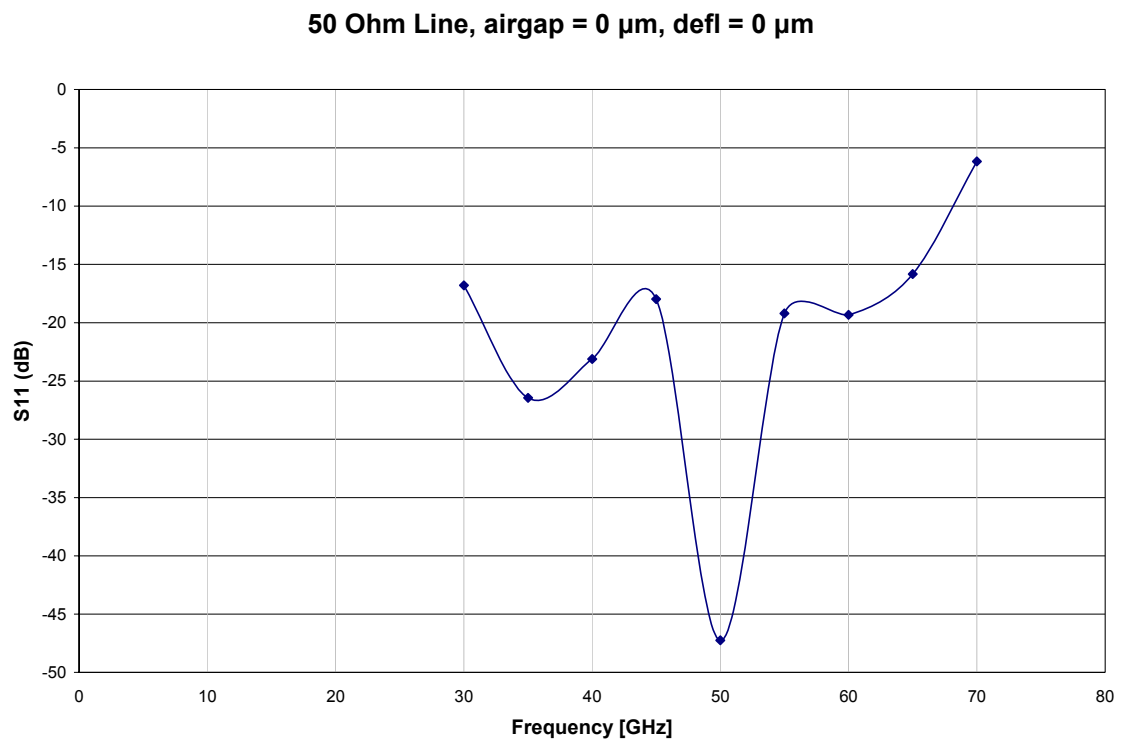


Fig. 7.10: Simulated S_{11} magnitude for a 50Ω line with no initial air gap and no deflection.

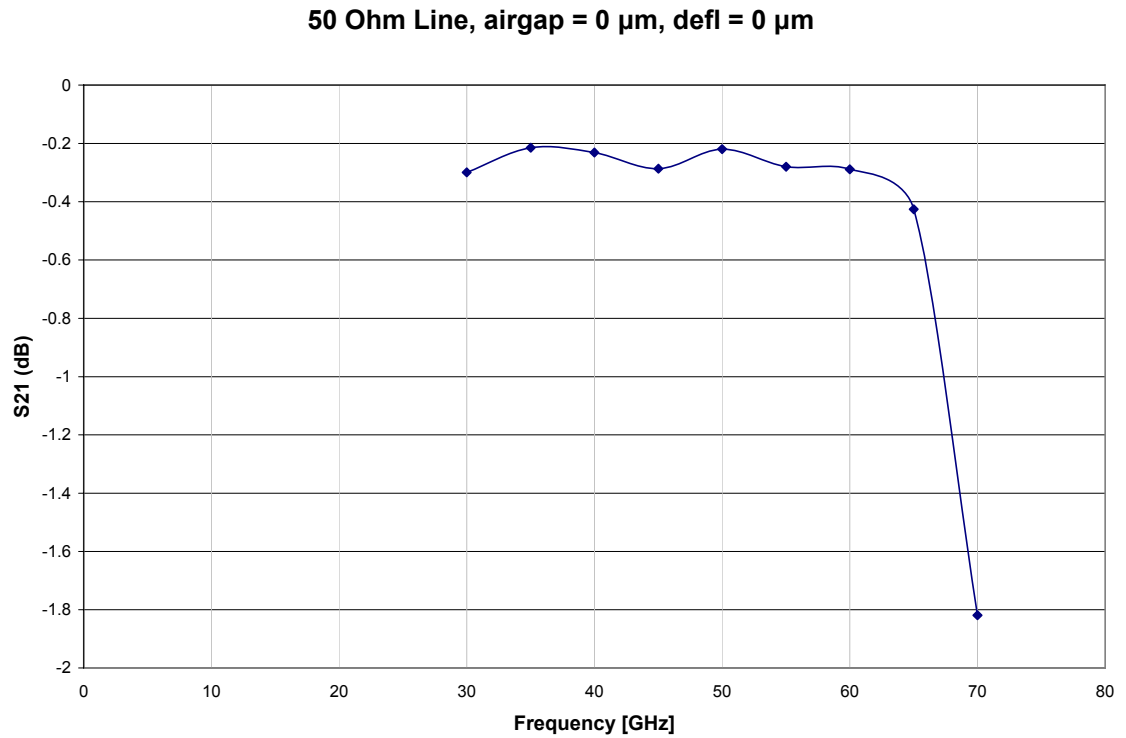


Fig. 7.11: Simulated S_{21} magnitude for a 50 Ω line with no initial air gap and no deflection.

Figure 7.12 shows the line impedance mismatch at 50 GHz as the ground membrane was deflected for the cases of 0 μm , 5 μm , and 10 μm initial air gap. The transmission line impedance was 50 Ω with no initial air gap and no deflection. Once there was an initial air gap of 5 μm or 10 μm , the line impedance was higher than 50 Ω initially. It can be seen that for essentially all cases of the 50 Ω line, S_{11} is below -10 dB, indicating good signal match to the line. Clearly, a 50 Ω transmission line is superior in this application to the 37 Ω line.

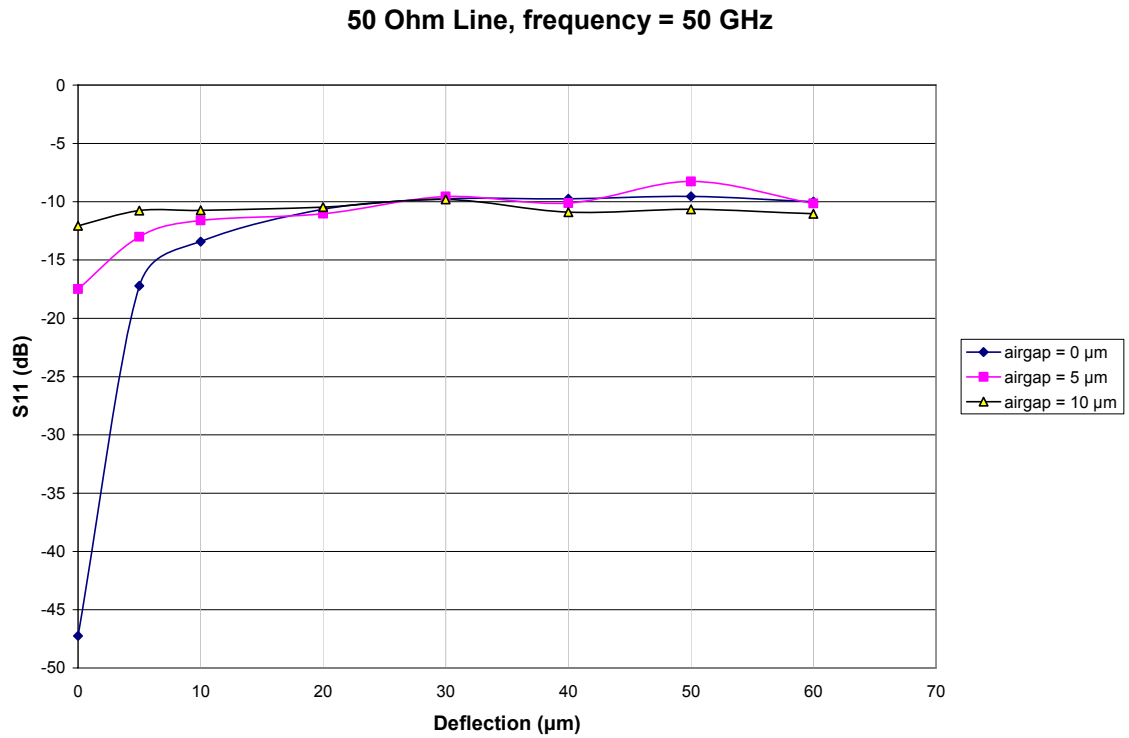


Fig. 7.12: Simulated S_{11} magnitude for a 50 Ω line at 50 GHz. Note how with membrane deflection, the line impedance increases and is no longer matched.

Figure 7.13 and Figure 7.14 show the S_{21} differential phase and the magnitude as a function of deflection for 0, 5 μm , and 10 μm initial air gaps. True impedance of 50 Ω only applied to the case of no initial air gap. With increasing air gap, the line impedance increased. There is clearly significant phase shift potential if the air gap could be minimized. Figure 7.15 shows the differential S_{21} phase for an initial air gap of 5 μm for different frequencies.

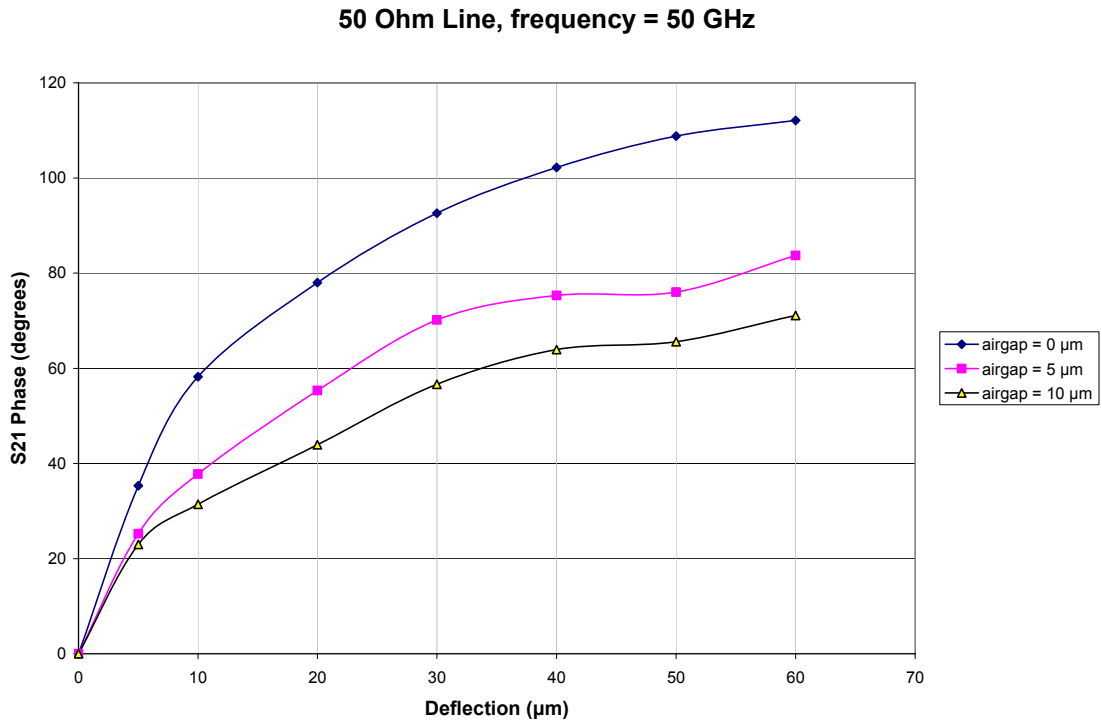


Fig. 7.13: Simulated differential S_{21} phase for a 50 Ω line for different air gaps vs. deflection at 50 GHz.

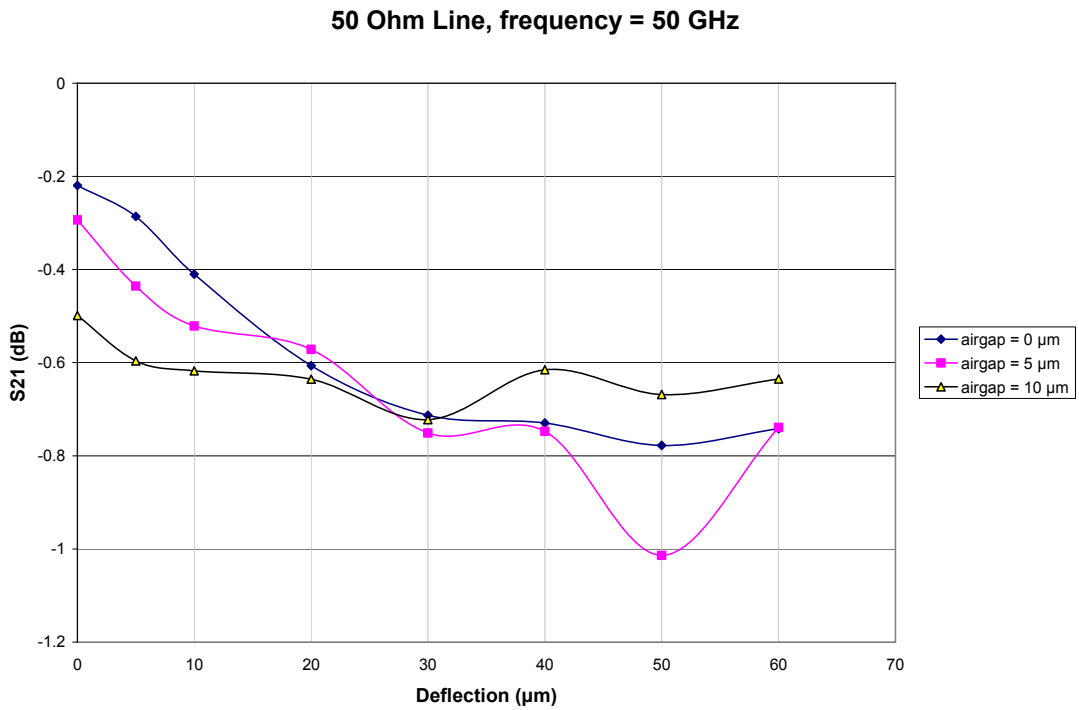


Fig. 7.14: Simulated S_{21} magnitude for a 50 Ω line for different air gaps vs. deflection at 50 GHz.

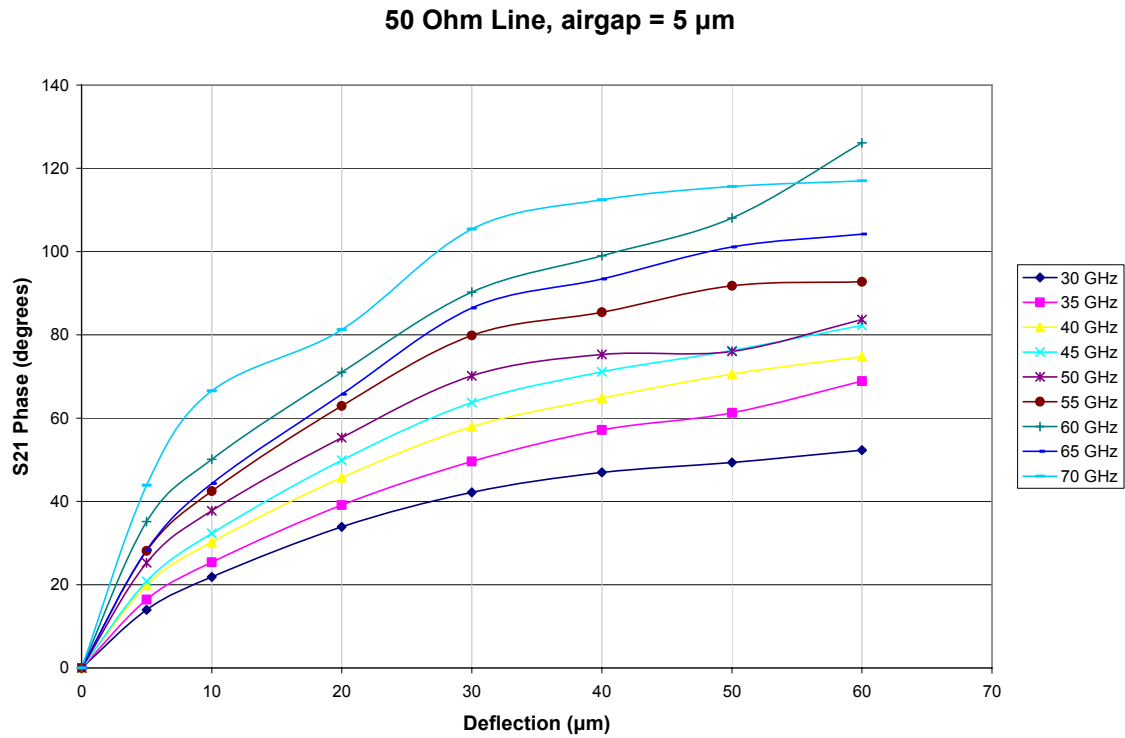


Fig. 7.15: Simulated differential S_{21} phase for a 50 Ω line with an initial air gap of 5 μm for different frequencies.

It can be seen that as the frequency increased, the phase shift also increases. This is because the effective length of the micro-ribbon effectively increases as the frequency increases and the wavelength decreases.

7.5 Measurements for the 20 μm wide Micro-Ribbons

Phase shift tests on the 20 μm wide micro-ribbons were done using an Anritsu ME7808A Vector Network Analyzer (VNA). Phase shift measurements were made by placing the phase shifter in Anritsu's Test Fixture with V-connectors (Fig. 7.16). Three 37 Ω transmission lines 3.5 cm long were fabricated on the silicon wafer, each with a micro-ribbon array fabricated below them.

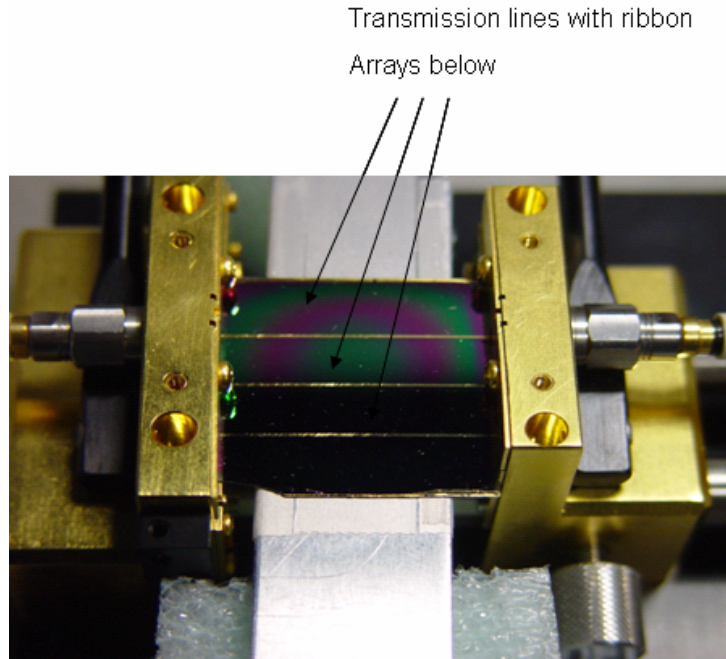


Fig. 7.16: Photograph of the phase shifter in the test fixture with V-connectors. The pull down electrode can be seen running vertically underneath the phase shifter which is propped up by foam.

The phase shifter was placed in the test fixture and 1 of the 3 sets of micro-ribbons was tested at a time. The pull down electrode was a strip of aluminum that was propped up by foam, ensuring good physical contact with the silicon wafer. The insulator used for testing was 3M scotch tape. The tape had a measured thickness of $60\ \mu\text{m}$. The distance between the micro-ribbons and the pull-down electrode was $120\ \mu\text{m}$ (Fig. 7.17); however, the maximum deflection possible was $60\ \mu\text{m}$.

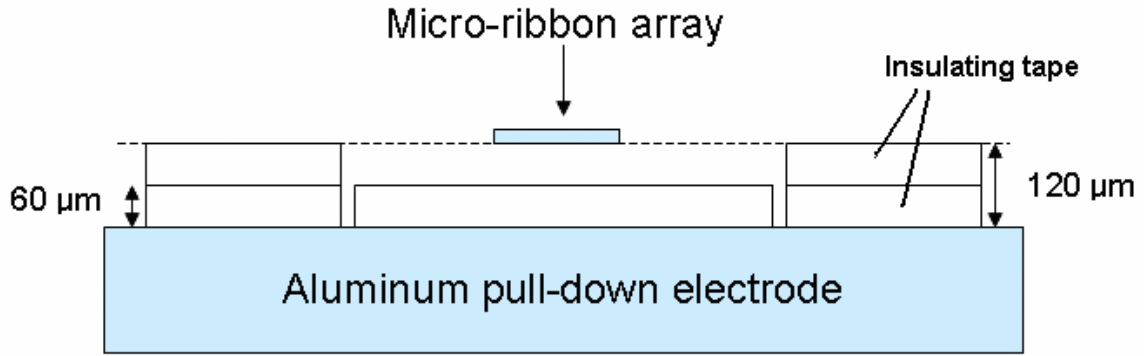


Fig. 7.17: Diagram of the pull-down electrode with the tape as an insulator. Two layers of 3M scotch tape is used to form the 120 μm gap between the micro-ribbon array and 1 layer is used as the insulator.

Phase shift tests were done for the 20 μm wide micro-ribbons built on under a 37 Ω transmission line (which is not ideal for matching). After the measurements were done, the 20 μm wide micro-ribbons were not damaged, unlike the case for the 5 μm wide micro-ribbons that will be discussed later.

The following tables show the measurements taken at 30 GHz, 40.80 GHz, 49.65 GHz, 53.85 GHz, and 59.40 GHz for two different arrays of 20 μm wide micro-ribbons. For the 53.85 GHz and 59.40 GHz measurements, the device becomes very lossy most likely due to the air cavity resonating at those frequencies. The VNA data for these values are found in Appendix E.

Table 7-1: Performance measurements for 20 μm wide micro-ribbons set 1 below a 37 Ω , 3.5 cm long transmission line.

Freq (GHz)	S_{11} at 0V (dB)	S_{11} at 120V (dB)	S_{21} (dB)/ S_{21} (degrees) at 0V	S_{21} (dB)/ S_{21} (degrees) at 120V	Differential Line Loss (0 to 120V) (dB)	Differential Insertion Loss (0 to 120V) (dB)	Phase Shift (degrees)
30.00	-12.2	-10.1	-5.50/ 118	-5.49/ 140	-0.18	-0.005	22
40.80	-10.8	-10.6	-7.37/ 67.0	-7.34/ 100	-0.05	-0.029	33
49.65	-10.2	-8.13	-7.49/ -98.0	-7.94/ -56.9	0.16	0.45	41
53.85	-10.4	-9.84	-11.1/ 35.6	-10.0/ 60.3	-1.14	-1.08	25
59.40	-6.75	-6.52	-9.59/ -45.1	-10.5/ -23.3	0.88	0.94	22

Table 7-2: Performance measurements for 20 μm wide micro-ribbons set 2 below a 37 Ω , 3.5 cm long transmission line.

Freq (GHz)	S_{11} at 0V (dB)	S_{11} at 120V (dB)	S_{21} (dB)/ S_{21} (degrees) at 0V	S_{21} (dB)/ S_{21} (degrees) at 120V	Differential Line Loss (0 to 120V) (dB)	Differential Insertion Loss (0 to 120V) (dB)	Phase Shift (degrees)
30.00	-12.3	-10.1	-5.49/ 120	-5.51/ 141	-0.16	0.02	21
40.80	-11.3	-11.0	-7.25/ 67.9	-7.25/ 99.6	-0.03	0.002	32
49.65	-9.81	-8.07	-7.34/ -98.8	-7.77/ -57.6	0.18	0.44	41
53.85	-10.7	-10.2	-10.2/ 35.5	-9.51/ 60.6	-0.77	-0.72	25
59.40	-6.55	-6.31	-9.37/ -44.9	-10.4/ -23.1	0.93	1.00	22

The two different sets of micro-ribbons show great consistency with each other when comparing their phase shifts. The phase shift measurements for both devices are very similar. The line loss is calculated as the insertion loss minus the mismatch loss as follows:

$$Line\ loss = 10 \log \left(\frac{10^{\frac{S_{21}}{10}}}{1 - 10^{\frac{S_{11}}{10}}} \right) \quad (7.1)$$

In equation (7.1), the line loss can be viewed as a ratio of the power coming out of the system and the power going in the system ignoring the mismatch loss.

The following differential phase results were measured at 49.65 GHz (Fig. 7.18).

A 41° phase shift was achieved at an actuation voltage of 120 V.

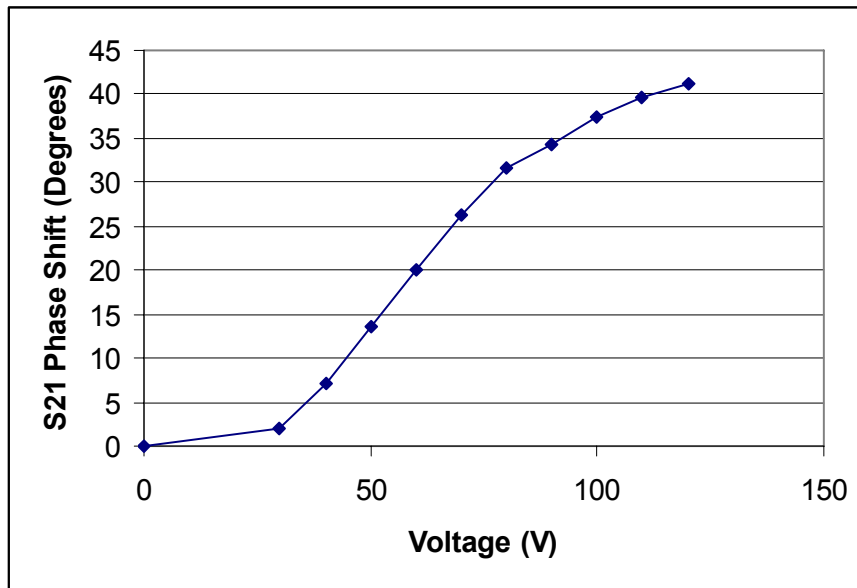


Fig. 7.18: Measured differential phase as a function of voltage for the 20 μm wide micro-ribbon array (set 2) underneath a 37 Ω transmission line at 49.65 GHz.

The measured phase shifts were lower than predicted in the simulation (Fig. 7.4). This is due to two factors. First, as mentioned earlier, the simulations over estimate the phase shift because they assume uniform ribbon deflections while in reality, the ribbons are curved when deflected. Second, these micro-ribbons were released using XeF_2 gas. This means that while the initial air gap was 20 μm below the center of the micro-

ribbons, it was deeper on the edges ($\sim 40 \mu\text{m}$) due to the trenching effect at the edge of the XeF_2 etched regions.

In Tables 7-1 and 7-2, the differential line loss and differential insertion loss values represent the line loss and insertion loss respectively due to actuating the micro-ribbon arrays. From these values, the Figure of Merit for the ribbon deflection can be calculated and are seen in Table 7-3 and 7-4. Figure of Merit is defined as:

$$\text{Figure of Merit} = \frac{\text{degrees of phaseshift}}{\text{line loss}} \quad (7.2)$$

These Figure of Merit values are useful in determining the losses due to the micro-ribbon deflection (the phase shift action) and they do not include the losses of the transmission line itself. Negative Figure of Merit values indicate that differential line loss improved during micro-ribbon deflection.

Table 7-3: Figure of merit for $20 \mu\text{m}$ wide micro-ribbons set 1 for phase shifts from a 120 V actuation voltage.

Freq	Phase Shift	Differential Line Loss (0 to 120V)	Figure of Merit (based on differential line loss)	Differential Insertion Loss (0 to 120V)	Figure of Merit (based on differential insertion loss)
(GHz)	(degrees)	(dB)	(degrees/dB)	(dB)	(degrees/dB)
30.00	22	-0.18	-120	-0.005	-4400
40.80	33	-0.05	-710	-0.03	-1100
49.65	41	0.16	260	0.45	91
53.85	25	-1.14	-22	-1.08	-23
59.40	22	0.88	25	0.94	23

Table 7-4: Figure of merit for 20 μm wide micro-ribbons set 2 for phase shifts from a 120 V actuation voltage.

Freq	Phase Shift	Differential Line Loss (0 to 120V)	Figure of Merit (based on differential line loss)	Differential Insertion Loss (0 to 120V)	Figure of Merit (based on differential insertion loss)
(GHz)	(degrees)	(dB)	(degrees/dB)	(dB)	(degrees/dB)
30.00	21	-0.16	-130	0.02	1000
40.80	32	-0.03	-1100	0.002	16000
49.65	41	0.18	230	0.44	95
53.85	25	-0.77	-33	-0.72	-35
59.40	22	0.93	24	0.99	21.8

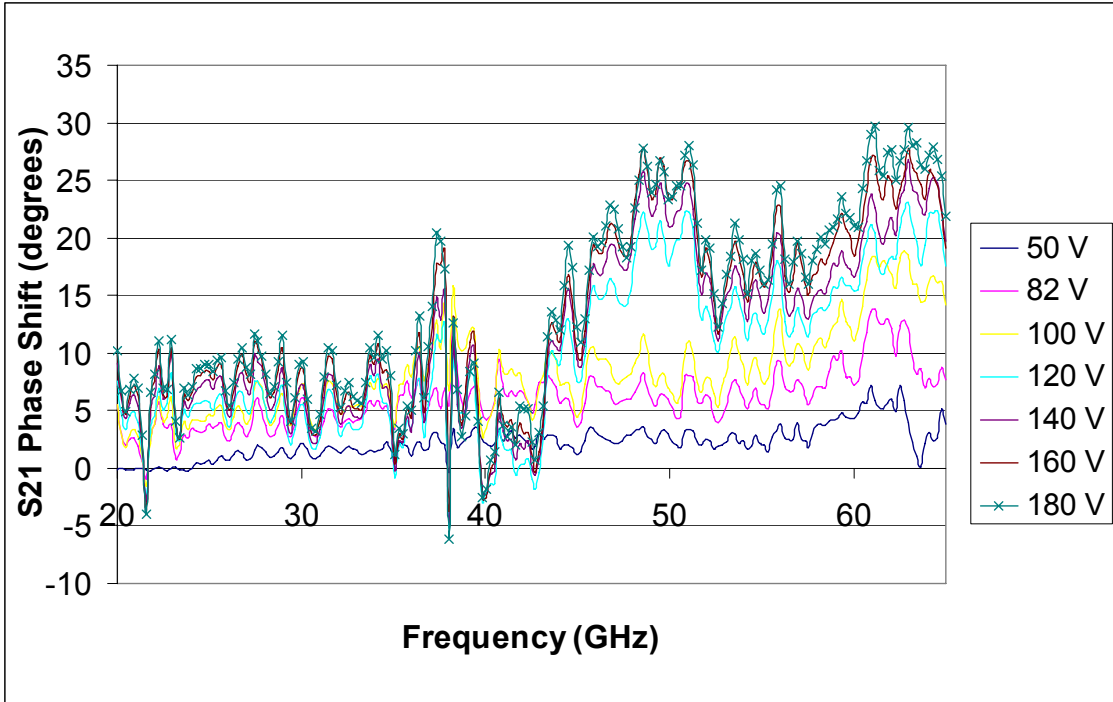
For micro-ribbon Set 1, at 49.65 GHz, a phase shift of 41° was achieved with 120 V actuation voltage and corresponded to a Figure of Merit of $260^\circ/\text{dB}$ of differential line loss. At 40.80 GHz, a phase shift of 33° was achieved with 120 V actuation voltage and this case possessed a negative Figure of Merit. This indicates that there were no losses as a result of obtaining the phase shift.

7.6 Measurements for the 5 μm and 10 μm wide Micro-Ribbons

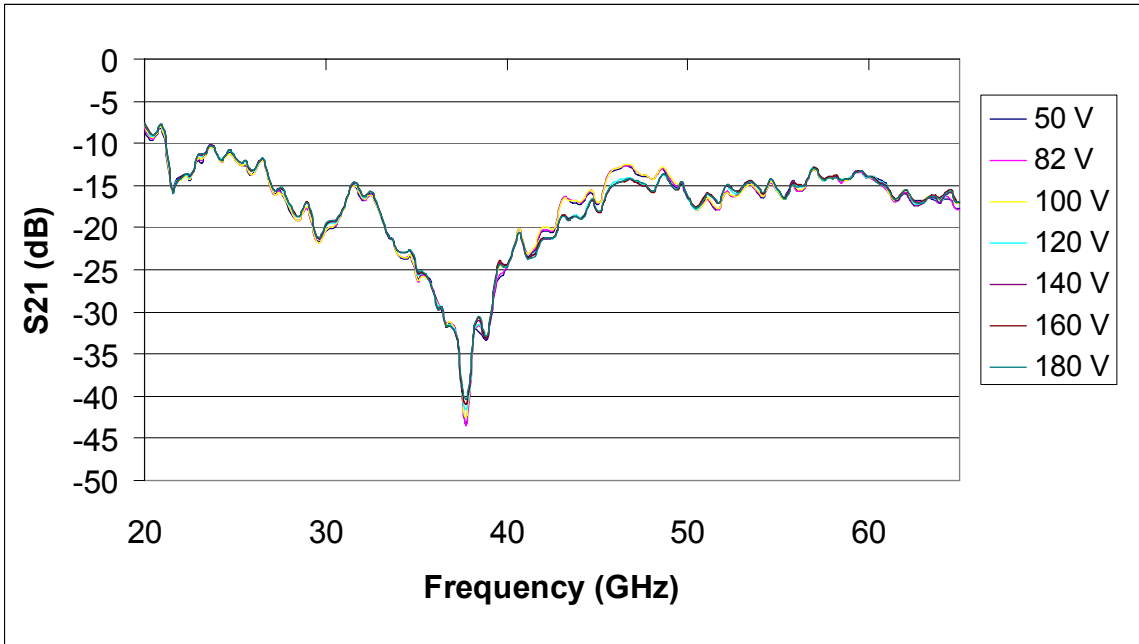
Phase shift tests on the 5 μm and 10 μm wide micro-ribbons were done using an Anritsu 37397D Vector Network Analyzer (VNA). The transmission line fabricated above each ribbon array was $50\ \Omega$ and 3.5 cm long. Prior to the phase shift tests, the VNA was calibrated using a 1601 point calibration for the frequency range of 20-65 GHz. Gore VNA cables were used during the calibration and phase shift tests. It should be noted that even after the calibrations, a change in the S_{21} of the order of ~ 0.1 dB could be observed by just lifting the cables off the table. The test fixture was not used in the calibration process, so the insertion losses measured could not be used to calculate a Figure of Merit for these devices.

7.6.1 *5 μm wide micro-ribbons*

The 5 μm wide micro-ribbons were fabricated in the “8 segment” geometry as discussed in Chapter 5. Two sets were tested. One set had spacing between micro-ribbons of 5 μm and the other set had 10 μm spacing. The S_{21} differential phase shift and S_{21} magnitude for these two sets can be found in Figure 7.19 and Figure 7.20. The oscillations seen in the plots were caused by signal reflections along the micro-ribbon region interface. In normal operation, the phase shifter would only have to operate within narrow frequency range and will therefore not be affected by the oscillations.

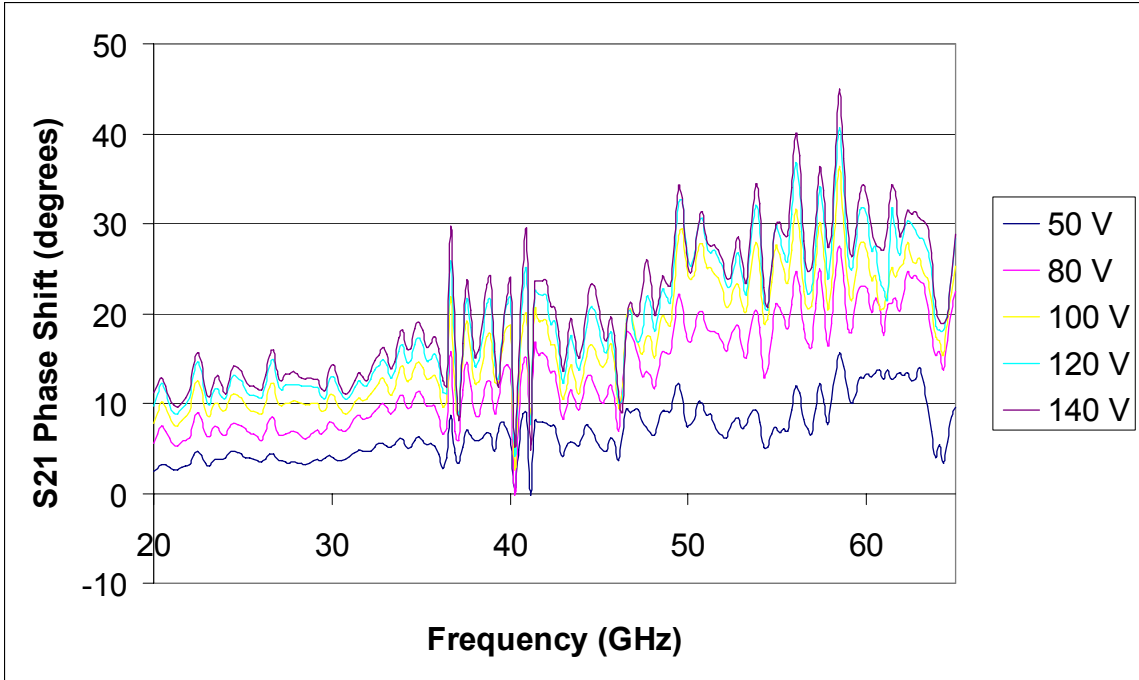


(a)

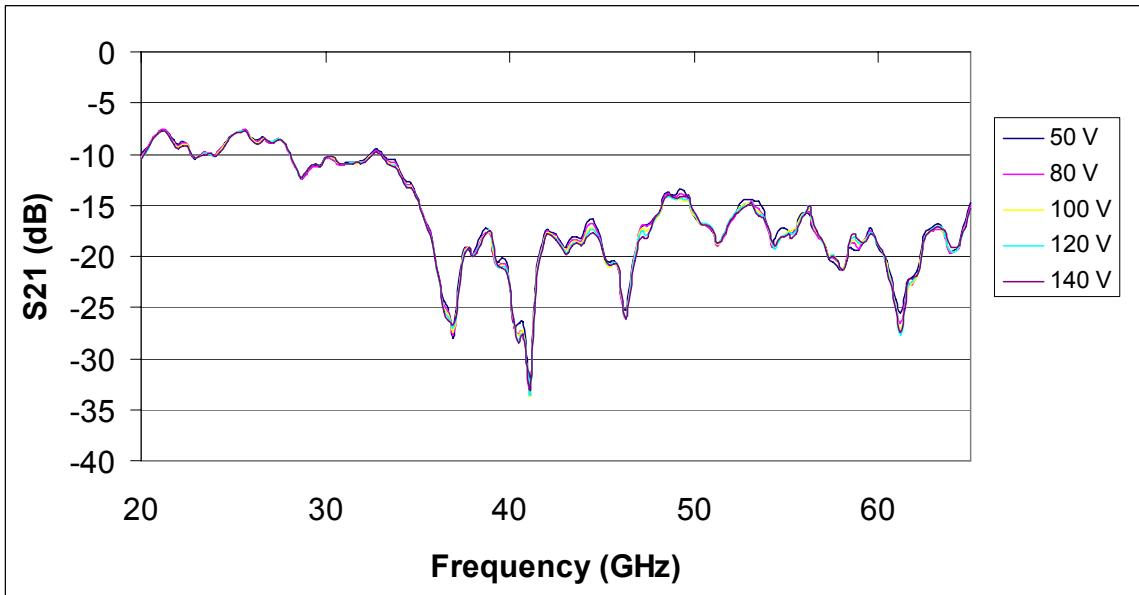


(b)

Fig. 7.19: (a) Measured S_{21} phase shift, (b) S_{21} magnitude for 5 μm wide micro-ribbons with 5 μm spacing in the “8 Segment” geometry.



(a)



(b)

Fig. 7.20: (a) Measured S_{21} phase shift, (b) S_{21} magnitude for 5 μm wide micro-ribbons with 10 μm spacing in the “8 Segment” geometry.

Since the length of the transmission line, as a function of RF signal wavelength linearly increases with frequency, it would be expected that the phase shift should increase linearly with frequency. However, as can be seen in Figure 7.19, this was not the case although a general trend of increasing phase shift with frequency is visible. Figure 7.20 shows a more clearly increasing phase shift with frequency. The actuation voltage for the device in Figure 7.20 was not increased past 140 V because it appeared that the micro-ribbons were at maximum deflection and a higher voltage could damage the micro-ribbons. It can be seen that there was not a significant increase in phase shift when the voltage was increased from 120 V to 140 V.

In Chapter 4, simulations showed that with larger inter-ribbon separation distances, a lower actuation voltage should be necessary to achieve the same deflection. Accordingly, the micro-ribbon array with 10 μm spacing was predicted to offer a higher phase shift at the same actuation voltage compared to the 5 μm spaced array. Figure 7.21, shows the phase shifts for the two devices at 2 different actuation voltages. As can be seen in the figure, the 10 μm spaced micro-ribbons indeed resulted in a larger phase shift at a given voltage due to a larger deflection. This feature was predicted in the COMSOL simulations.

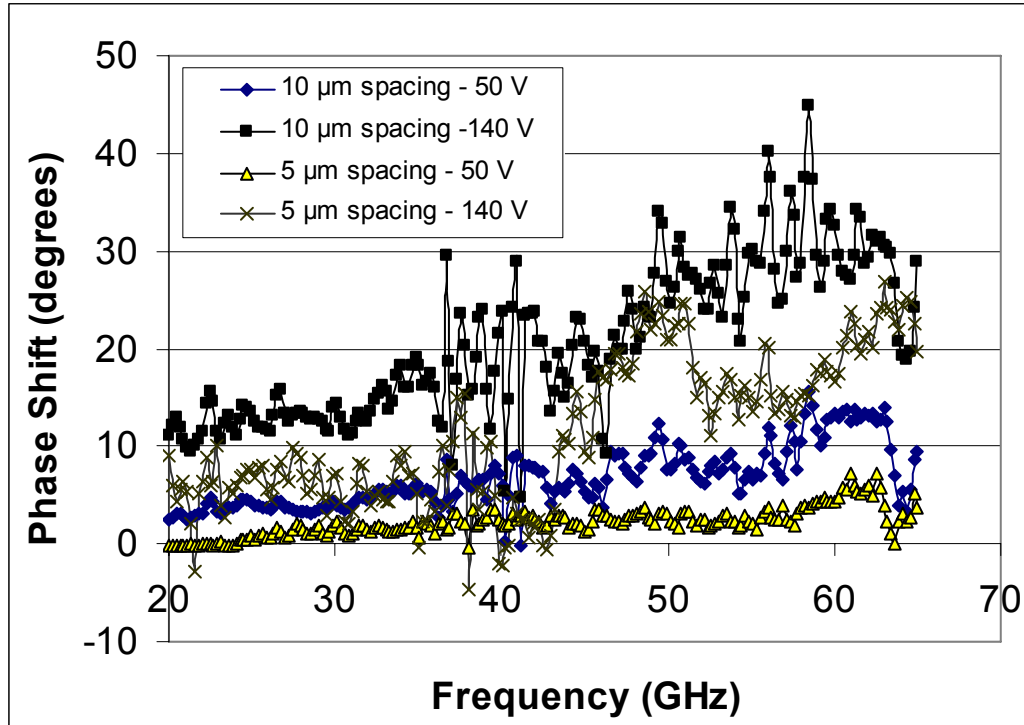


Fig. 7.21: Comparison of measured phase shift results for micro-ribbon arrays with ribbons 5 μm in width with two different ribbon separation distances.

After the measurements were made, photographs of the micro-ribbon arrays were taken (Fig. 7.22). These photographs show serious damage done to the micro-ribbons. It would appear that 5 μm wide micro-ribbons were too fragile for this application.

The resulting phase shifts measured at 50 GHz were lower than the predicted phase shifts in Figure 7.13 for initial air gap = 5 μm . Simulations predicted phase shifts greater than 80° while measured phase shifts were $\sim 30^\circ$. This could be due to the fact that many of the micro-ribbons seemed damaged and are many microns out of plane and thus increased the effective initial air gap.

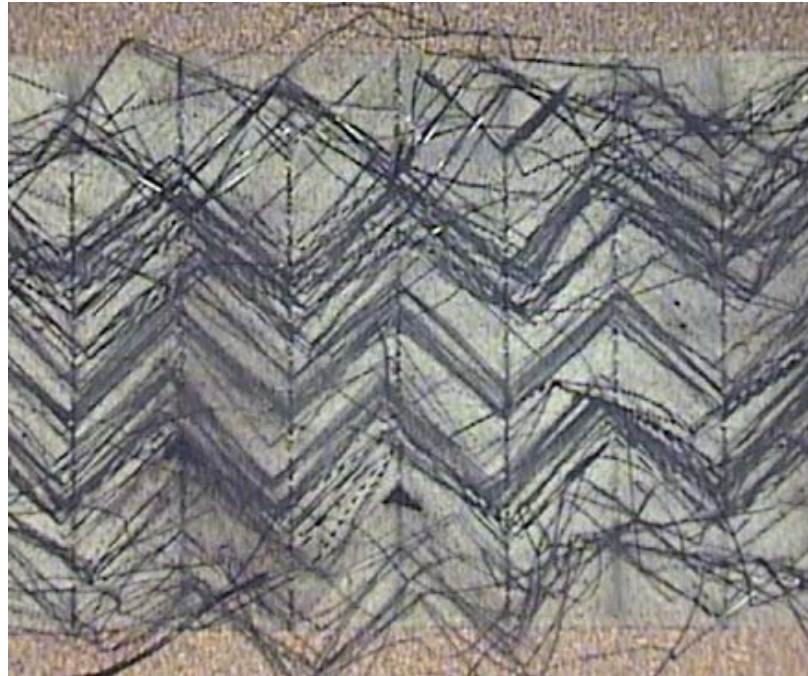
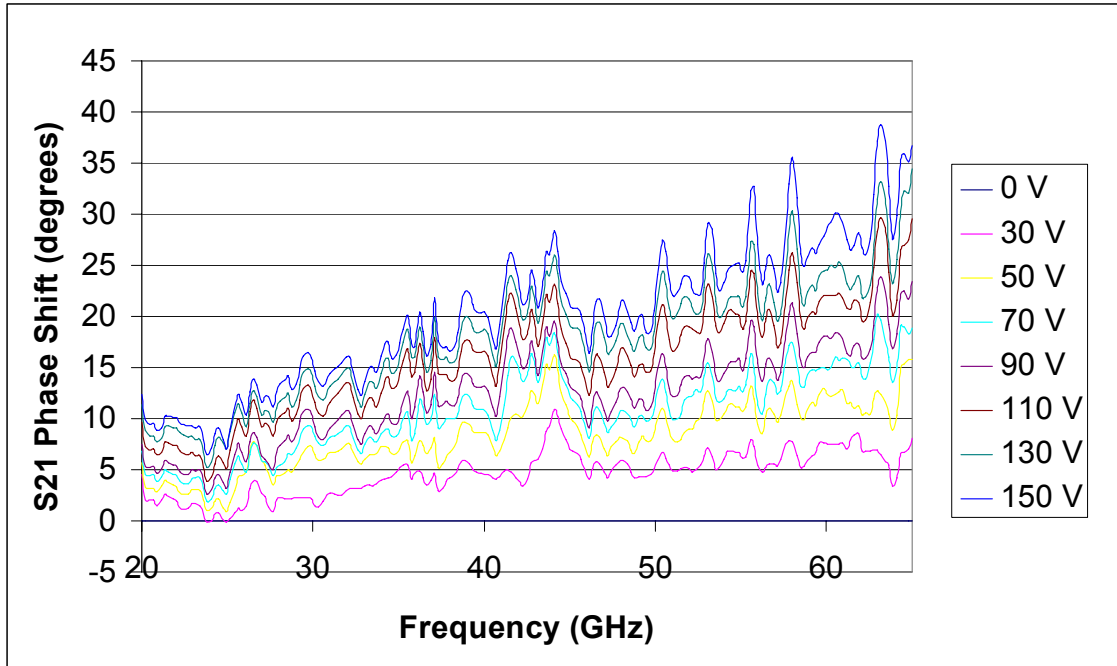


Fig. 7.22: Photographs of the 5 μm wide micro-ribbons after phase shift tests. It is clear that many micro-ribbons were damaged in the testing process.

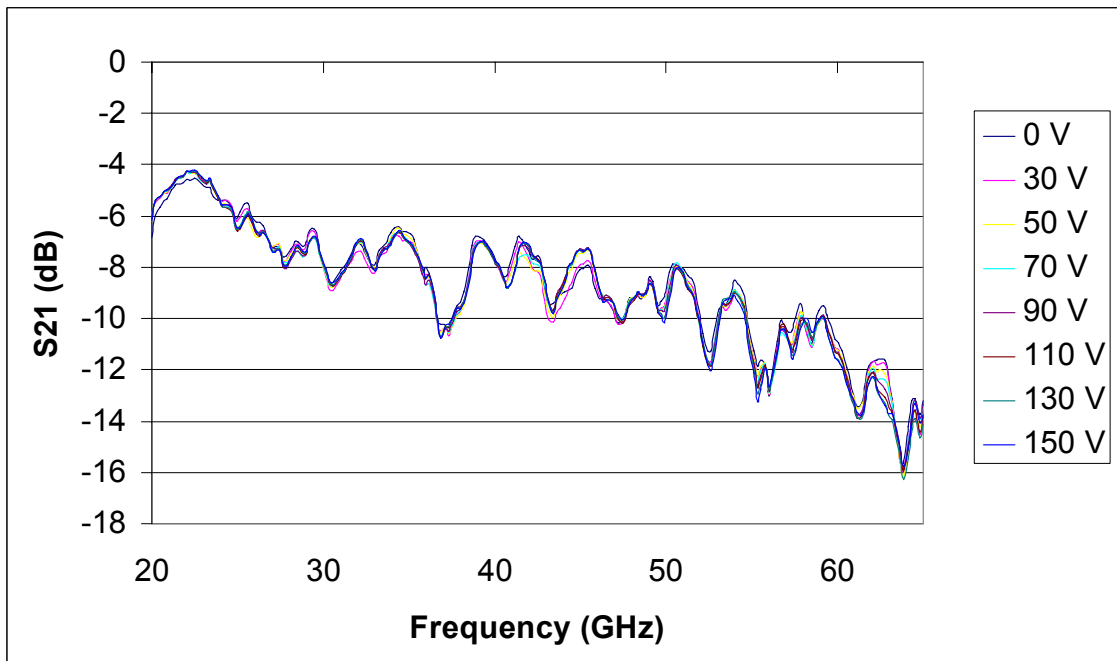
7.6.2 *10 μm wide micro-ribbons*

The 10 μm wide micro-ribbons were fabricated in the “8 segment” geometry as discussed in Chapter 5. Two sets were tested. One set had spacing between micro-

ribbons of 5 μm and the other set had 10 μm spacing. The S_{21} differential phase shift and S_{21} magnitude for these two sets can be found in Figure 7.23 and Figure 7.24.

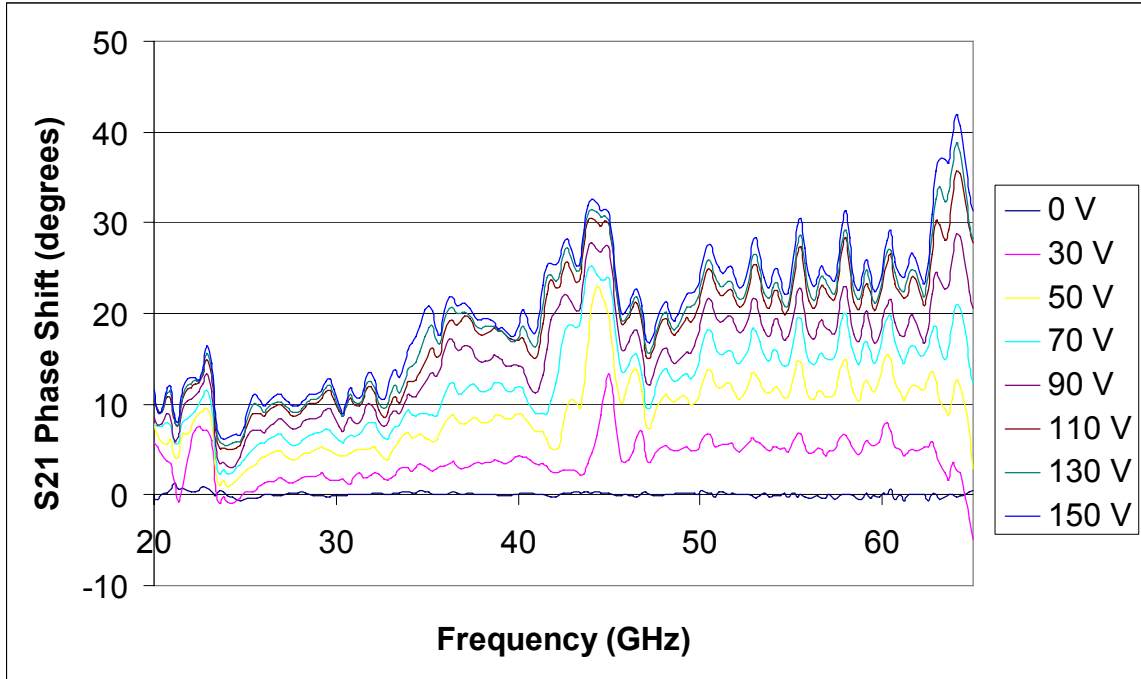


(a)

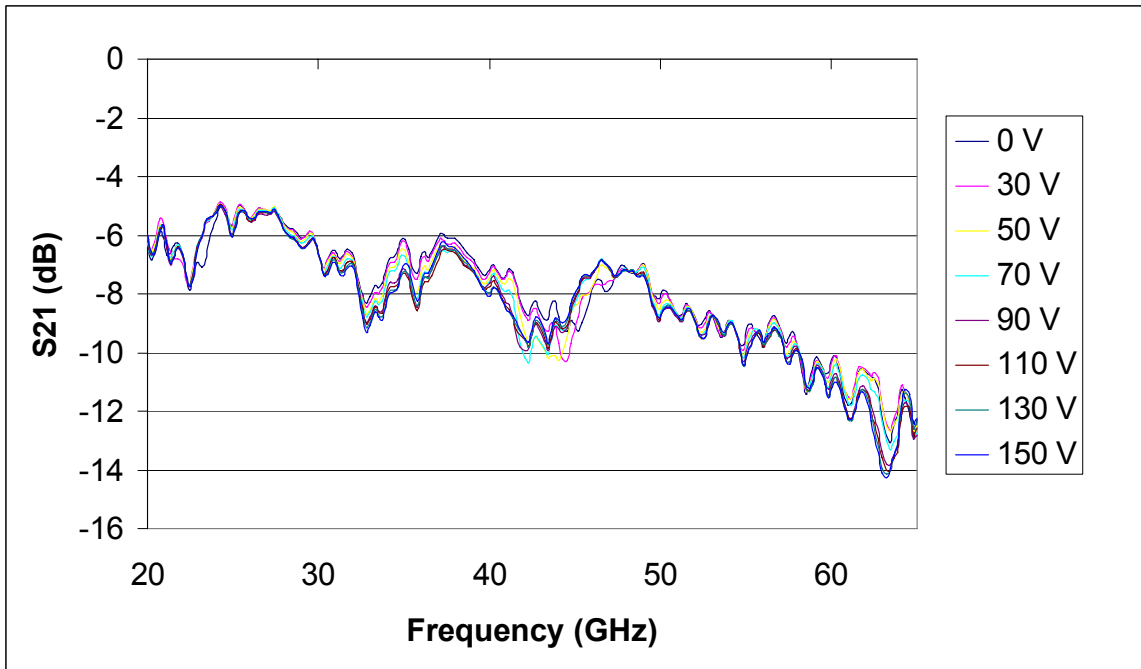


(b)

Fig. 7.23: (a) Measured S_{21} phase shift, (b) S_{21} magnitude for 10 μm wide micro-ribbons with 5 μm spacing in the “8 Segment” geometry.



(a)



(b)

Fig. 7.24: (a) Measured S_{21} phase shift, (b) S_{21} magnitude for 10 μm wide micro-ribbons with 10 μm spacing in the “8 Segment” geometry.

Again, the measured phase shifts were lower than the simulated phase shifts in Figure 7.13 for the case of a 10 μm initial air gap. At 50 GHz, the simulated phase shift was $\sim 70^\circ$ while the measured phase shift was only $\sim 25^\circ$. The 10 μm wide micro-ribbons held up under the testing process better than the 5 μm wide micro-ribbons (Fig. 7.25).



(a)



(b)

Fig. 7.25: Photographs of the 10 μm wide micro-ribbons after phase shift tests. (a) 5 μm spacing, some micro-ribbons do seem to have distorted, (b) 10 μm spacing, ribbons seem to all be in good shape.

Comparing the two sets of 10 μm wide micro-ribbons at specific actuation voltages, Figure 7.26 was obtained. As can be seen, the ribbon spacing did not make a large difference in this case (less than a few degrees). This was due to the micro-ribbon width being larger or equal to the separation distance. If the ribbon separation distance was say 10 μm and 20 μm , then a more significant difference in phase shift for specific voltage would be expected similar to the results in Figure 7.21. It is worth noting that the measured results for both the 5 μm and 10 μm spacing cases are in close agreement.

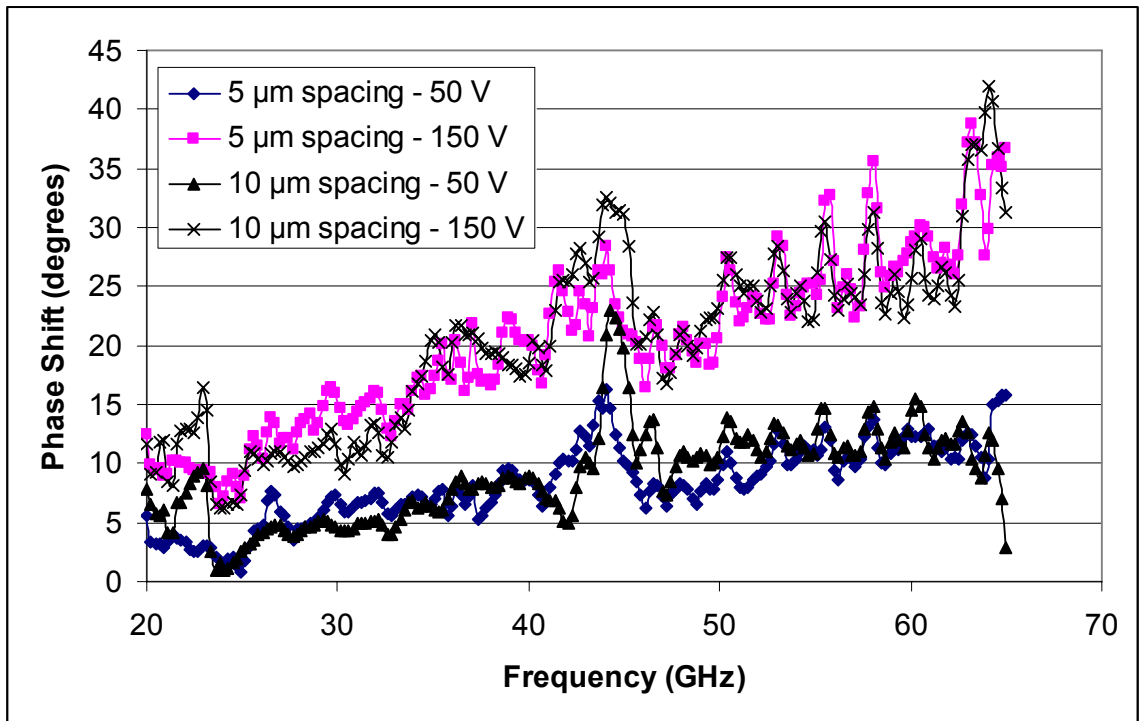


Fig. 7.26: Comparison of measured phase shift results for micro-ribbon arrays with ribbons 10 μm in width with two different ribbon separation distances.

7.6.3 10 μm wide micro-ribbon reproducibility of measurements testing

Finally, the reproducibility of the measurements is discussed. For this discussion, the micro-ribbon array under study was made up of micro-ribbons that were 10 μm in width and had a ribbon separation of 5 μm . For this experiment, measurements were taken at 0 V, 150 V, 0 V, 150 V and then 0 V again in that order (Fig. 7.27).

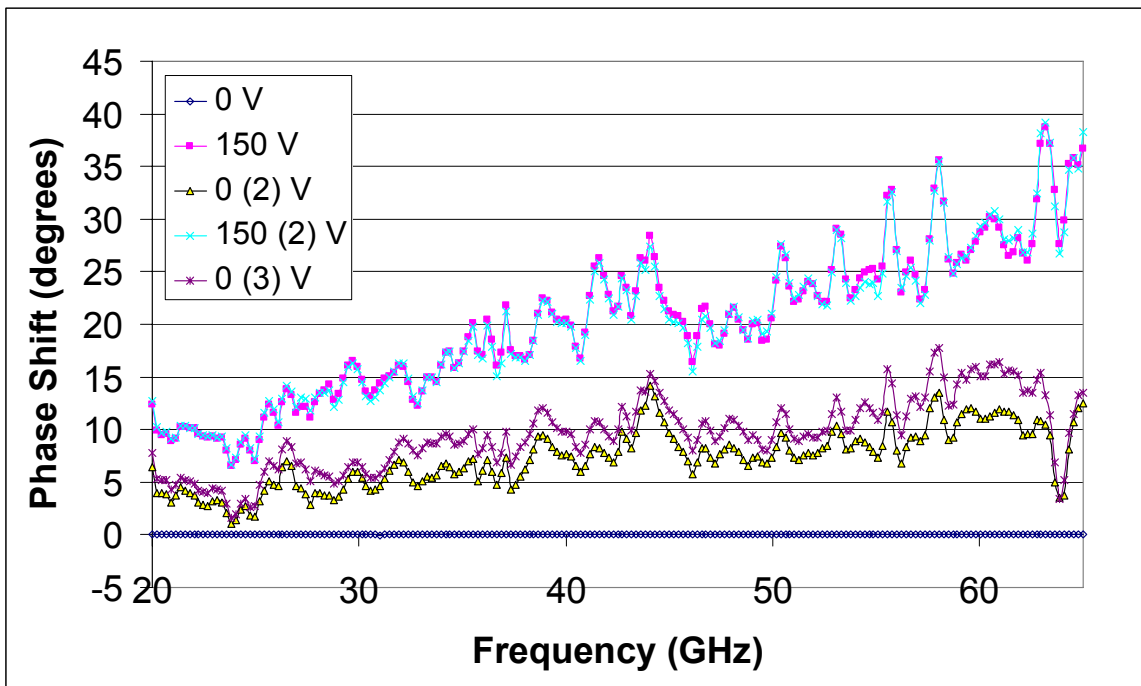


Fig. 7.27: Reproducibility of measurement experiment done on the 10 μm wide micro-ribbons with 5 μm spacing actuating the ribbons from 0 V, 150 V, 0 V, 150 V, and 0 V.

As can be seen in the figure above, the measurements at 150 V seem to match well between measurements. This indicates that the ribbon suffered no significant damage during deflection and that they returned to the same positions when the same voltage was applied. However, it is also clear that the measurements at the three 0 V readings do not match. This was most likely due to the tape/insulator building up a static

charge, which prevents the ribbons from returning to a fully undeflected position. When the power supply was shut off, it was observed through the measured differential phase that the micro-ribbons were still settling after 10 minutes. This issue could likely be addressed by using a leaky insulator that would not store a charge. Figure 7.28 shows the same reproducibility test but for the 10 μm ribbon spacing.

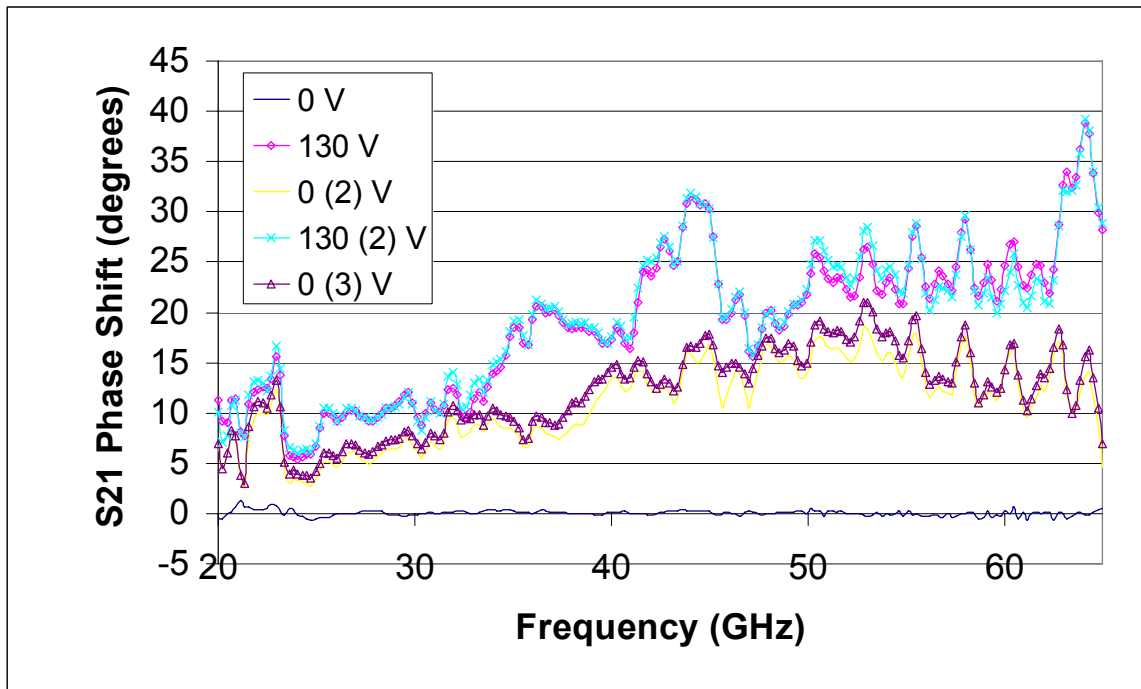


Fig. 7.28: Reproducibility of measurement experiment done on the 10 μm wide micro-ribbons with 10 μm spacing actuating the ribbons from 0 V, 150 V, 0 V, 150 V, and 0 V.

7.7 Summary

This chapter discussed the phase shift simulations and measurements done on the micro-ribbon arrays. The HFSS simulations showed the importance of minimizing the initial air gap that is a result of the fabrication process. By reducing the initial air gap, the required actuation voltage for a given phase shift could be decreased. Also, through the

HFSS simulations, it was shown that a 50 Ω line was better than a 37 Ω line from the point of view of mismatch losses.

The 20 μm wide micro-ribbons resulted in a 33° phase shift at 40.80 GHz at 120 V actuation voltage. The negative Figure of Merit value indicated no losses in the signal during a phase shift. The measured phase shift agreed well with the simulations. The 5 μm wide micro-ribbons resulted in a 30° phase shift at 50 GHz. The measured phase shifts did not match well with the simulations and the micro-ribbons were too fragile for the applied voltages which resulted in many broken micro-ribbons. The measured phase shift for arrays that had different micro-ribbon array spacing confirmed that having larger spacing lowered the required actuation voltage for a given phase shift. Lastly, the 10 μm wide micro-ribbons resulted in a 25° phase shift at 50 GHz with 150 V pull-down voltage. The phase shift was again lower than the simulated results. Reproducibility of measurements was demonstrated by actuating the membranes from 0 V, 150 V, 0 V, 150 V, and 0 V. The phase shifts at both 150 V measurements were in agreement. However, the inconsistent phase shifts at the 0 V readings implied that the insulator used in the measurements was retaining a static charge.

It is recommended to use 20 μm or wider micro-ribbons to ensure durability in the phase shifter application. The fact that the micro-ribbon becomes stiffer with increased width can be solved by increasing the separation distance between micro-ribbons. However, the resistive losses that occur from increasing the separation distances were not studied, so no conclusions can be drawn from that perspective.

CHAPTER 8

CONCLUSION AND FUTURE WORK

8.1 Conclusion

A MEMS phase shifter was presented that used a micro-ribbon array integrated into the ground plane of a microstrip transmission line. The micro-ribbons were electrostatically actuated away from the RF friendly substrate creating an air gap between the micro-ribbons and the transmission line. The silicon and air form a stacked dielectric. By controlling the deflection of the micro-ribbons, an analog phase shift is achieved by changing the effective permittivity of the microstrip line.

Finite element modeling simulations in COMSOL were carried out in order to optimize the geometry of the micro-ribbons. Simulations showed that by increasing the separation distance between micro-ribbons, the electrostatic force increased due to fringing fields. It was also shown that for a given span, a larger jog angle results in a more flexible micro-ribbon. Lastly, it was shown that when the number of segments in the micro-ribbons ranged from 3 to 7, there was not a significant increase in the spring constant. However, there was a slight increase in the spring constant that was proportional to the number of segments.

Simulations in HFSS were also carried out to simulate the phase shift. These indicated that the initial air gap, formed by releasing the micro-ribbons from the substrate in the fabrication process, should be kept at a minimum. By decreasing the initial air gap, a larger phase shift could be achieved for a given micro-ribbon array deflection. This translated to a lower actuation voltage required for a desired phase shift.

The MEMS phase shifter was fabricated entirely at the NSFL at the University of Manitoba. Different dry release processes were tested in order to determine a recipe that would minimize the initial air gap caused due to the release process. Micro-ribbons of widths 5, 10 and 20 μm were fabricated.

Phase shift measurements were carried out and it was determined that the 5 μm wide micro-ribbons were too fragile for the application. The 10 μm wide micro-ribbons were durable enough to survive the phase shift tests, and a phase shift of 25° was achieved at 50 GHz with 150 V actuation voltage. The 20 μm wide micro-ribbons performed the best: a 33° phase shift was achieved at 40.80 GHz with an actuation voltage of 120 V. The Figure of Merit was negative indicating that there was no line loss

due to ribbon deflection. At 49.65 GHz, for the same 20 μm wide micro-ribbon array, a 41° phase shift was achieved with an actuation voltage of 120 V. The Figure of Merit was 260°/dB of differential line loss.

8.2 Future Work and Recommendations

Further improvements can be made in the fabrication process. It is possible to design a process that utilizes a sacrificial layer, most likely photo-resist, in order to decrease the initial air gap even further while having wider micro-ribbons. The challenges of such an approach would be to design a micro-ribbon geometry that would avoid sticking to the substrate once the micro-ribbons were released. The introduction of dimples on the micro-ribbons would be a possible solution to the sticking problem. A sacrificial based fabrication process would also allow for the phase shifter to be built on less lossy, non-silicon substrates.

REFERENCES

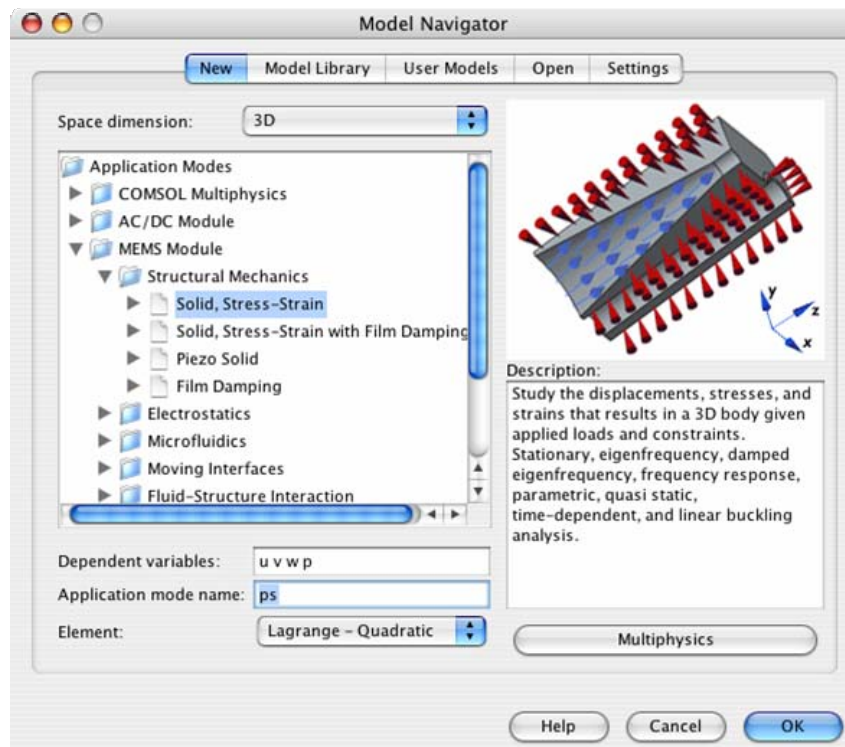
- [1] Johnson, R.C., and Jasik, H.: 'Antenna Engineering Handbook' (McGraw-Hill, 2nd Ed., New York, 1984, chapter 20).
- [2] Koul, S.K., and Bhat, B.: 'Microwave and Millimeter Wave Phase Shifters' (Artech House, 1991, vol. I, Norwood, MA).
- [3] Rebeiz, G.M.: 'RF MEMS: Theory, Design and Technology' (Wiley Inter-Science, New Jersey, USA, 2003).
- [4] Kasap, S.O.: 'Optoelectronics and Photonics: Principles and Practices' (Prentice Hall, New Jersey, 2001, p. 7).
- [5] Shafai, C., Sharma, S.K., Shafai, L., and Chrusch, D.D.: "Microstrip Phase Shifter Using Ground-Plane Reconfiguration", IEEE Transactions on Microwave Theory and Techniques, Vol. 52, No. 1, January 2004, pp. 144-153.
- [6] COMSOL Multiphysics™ version 3.2a. (COMSOL AB, 2005, Stockholm, Sweden).
- [7] HFSS™ version 9.2.1. (Ansoft Corporation, 2004, Pittsburgh, PA, USA).
- [8] Kovacs, G.T.A.: 'Micromachined Transducers: Sourcebook' (McGraw-Hill, New York, USA, 1998).
- [9] Campbell, S.A.: 'The Science and Engineering of Microelectronic Fabrication' (Oxford, New York, 2001).
- [10] Petersen, K.E.: "Dynamic micromechanics on silicon: Techniques and devices", IEEE Transactions on Electron Devices, Vol. 25, Issue 10, Oct. 1978, pp. 1241-1250.
- [11] Tang, W.C, Lim, M.G., Howe, R.T.: "Electrostatic Comb Drive Levitation and Control Method", Journal of Microelectromechanical Systems, Vol. 1, Issue 4, Dec. 1992, pp. 170-178.
- [12] Fan, L.-S, Tai, Y.-C., and Muller, R.S.: "IC-Processed Electrostatic Micromotors", Sensors and Actuators, Vol. 20, no.1-2, November 15, 1989, pp. 41-47.
- [13] Rebeiz, G.M., Tan, G.L., and Hayden, J.S.: "RF MEMS Phase Shifters: Design and Application", IEEE Microwave Magazine, 2002, 42, pp. 72-81.

- [14] Pillans, B., Eshelman, S., Malczewski, A., Ehmke, J., Goldsmith, C.: “Ka-band RF MEMS phase shifters” *Microwave and Guided Wave Letters*, IEEE, Vol. 9, Issue 12, Dec. 1999, pp. 520 – 522.
- [15] Mihailovich, R.E., Kim, M., Hacker, J.B., Sovero, A., Studer, J., Higgins, J.A., and DeNatale, J.F.: “MEM Relay for Reconfigurable RF Circuits”, *IEEE Microwave and Wireless Components Letters*, Vol. 11, No. 2, February 2001, pp. 53-55.
- [16] Jian, Z., Yuanwei, Y., Le, L., Chen, C., Yong, Z., and Naibin, Y.: “A 3-port MEMS switch for MEMS Phase Shifter Application”, *Proceedings of 1st IEEE International Conference on Nano/Micro Engineered and Molecular Systems*, January 18-21, 2006, Zhuhai China, pp. 611-614.
- [17] Jian, Z., Wei, Y.-Y., Chen, C., Yong, Z.: “A Compact 5-bit Switched-line Digital MEMS Phase Shifter”, *Proceedings of 1st IEEE International Conference on Nano/Micro Engineered and Molecular Systems*, January 18-21, 2006, Zhuhai China, pp. 623-626.
- [18] Barker, N.S., and Rebeiz, G.M.: “Optimization of Distributed MEMS Transmission Line Phase Shifter – U-band and W-band Designs”, *IEEE Transactions on Microwave Theory and Techniques*, Vol. 48, No. 11, November 2000, pp. 1957-1966.
- [19] Hung, J.-J., Dussopt, L., Rebeiz, G.M.: “Distributed 2- and 3-bit W-band MEMS Phase Shifters on Glass Substrates”, *IEEE Transactions on Microwave Theory and Techniques*, Vol. 52, No. 2, February 2004, pp. 600-606.
- [20] Qing, J., Shi, Y., Li, W., Lai, Z., Zhu, Z., and Xin, P.: “Ka-band Distributed MEMS Phase Shifters on Silicon Using AlSi Suspended Membrane”, *Journal of Microelectromechanical Systems*, Vol. 13, No. 3, June 2004, pp. 542-549.
- [21] Sharma, S.K., Shafai, C., and Shafai, L.: “Performance of Microstrip Transmission Line Phase Shifter with Integrated Ground Plane Membrane Using Low Actuation Voltage”, *Proc. 12th International Symposium on Antenna Technology and Applied Electromagnetics (ANTEM) and Canadian Radio Science (URSI/CNC)*, July 16-19, 2006, Montreal, QC, Canada, pp. 355-358.
- [22] Submitted Paper: Shafai, C., Sharma, S.K., Yip, J., Shafai, L., Shafai, L.: “Microstrip Delay Line Phase Shifter by Actuating Integrated Ground Plane Membranes” *IET Microwave, Antennas & Propagation*, revisions submitted June 2007.

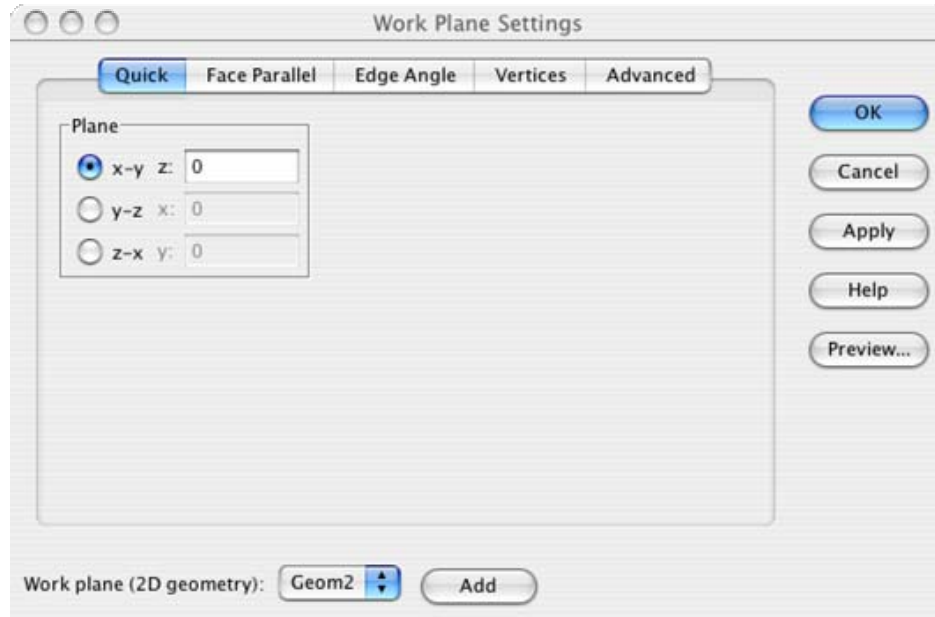
APPENDIX A – COMSOL PROCEDURE

This section of the thesis outlines the procedure to do a typical COMSOL simulation with the adjacent rigid ground planes. The micro-ribbon will be a simple 3 mm x 20 μm x 1 μm straight beam. Micro-ribbons with more complex geometries can be done by changing the geometry of the micro-ribbon drawn. The separation distance between the ribbons and the adjacent grounds will be 50 μm . The ground plane will be 4 mm x 3 mm. The pull-down electrode is 100 μm below the micro-ribbons.

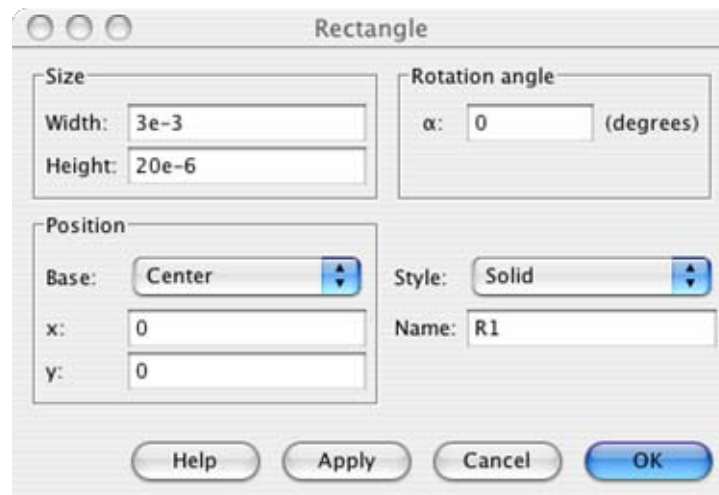
1. Open COMSOL Multiphysics. From the “Model Navigator” window, choose “New” and “3D” for space dimensions. In the “*Applications Modes*”, select “*MEMS Module – Structural Mechanics – Solid, Stress-strain*” and for “*Application mode name*” enter “ps”. Click **OK**.



2. Now create the micro-ribbon by going to the “*Draw*” menu and go to “*Work Plane Settings...*”. Confirm that the following screen appears (z is set to “0” for the x-y plane), and click **OK**.

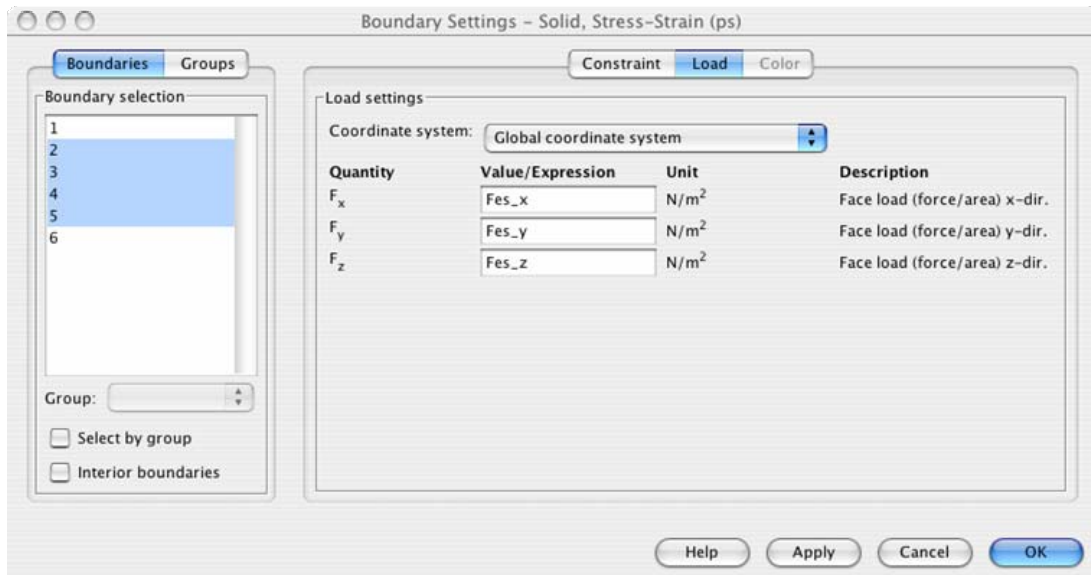


Next, shift-click the “make a rectangle box” and fill in the dimensions as seen in the following figure to create a straight micro-ribbon of 3 mm x 20 μm . Click **OK**.

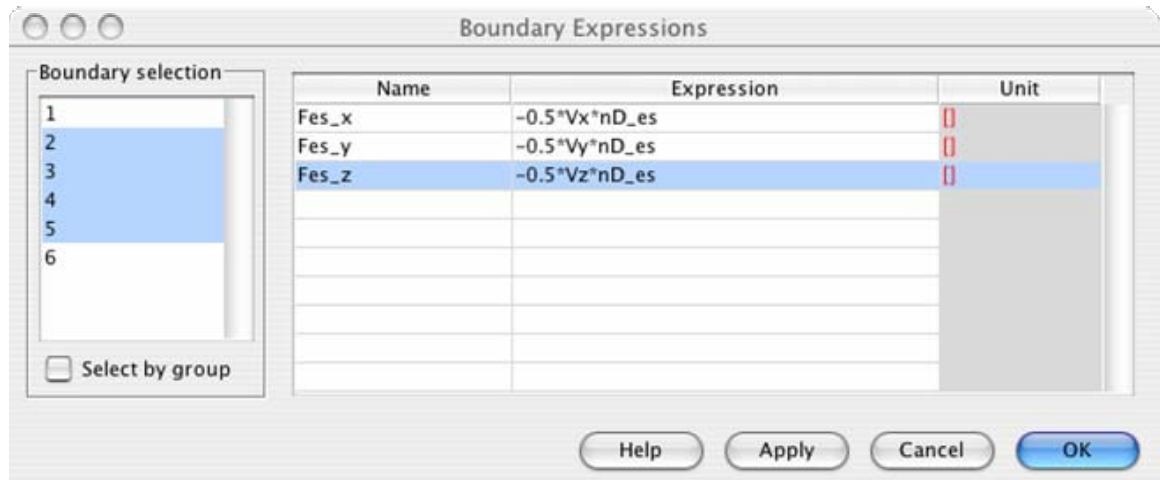


The geometry for the micro-ribbon is now defined in 2D. To make the micro-ribbon a 3D object, go to “*Draw > Extrude...*” and enter **1e-6** for the “*Distance*” parameter and click **OK**.

- Next, to define the micro-ribbon as Aluminum, go to “*Physics > Subdomain Settings...*” and select the micro-ribbon and define the material to be “**Aluminum 3003-H18**”. To define the boundary conditions for the micro-ribbon go to “*Physics > Boundary Settings...*”. Select Boundaries 1 and 6 and set the “*Constraint Condition*” to “**Fixed**”. Select the remaining boundaries, 2 through 5, and assign the following “*Loads*” as can be seen in the following figure. The forces are obtained from the electrostatics module and will be defined later.

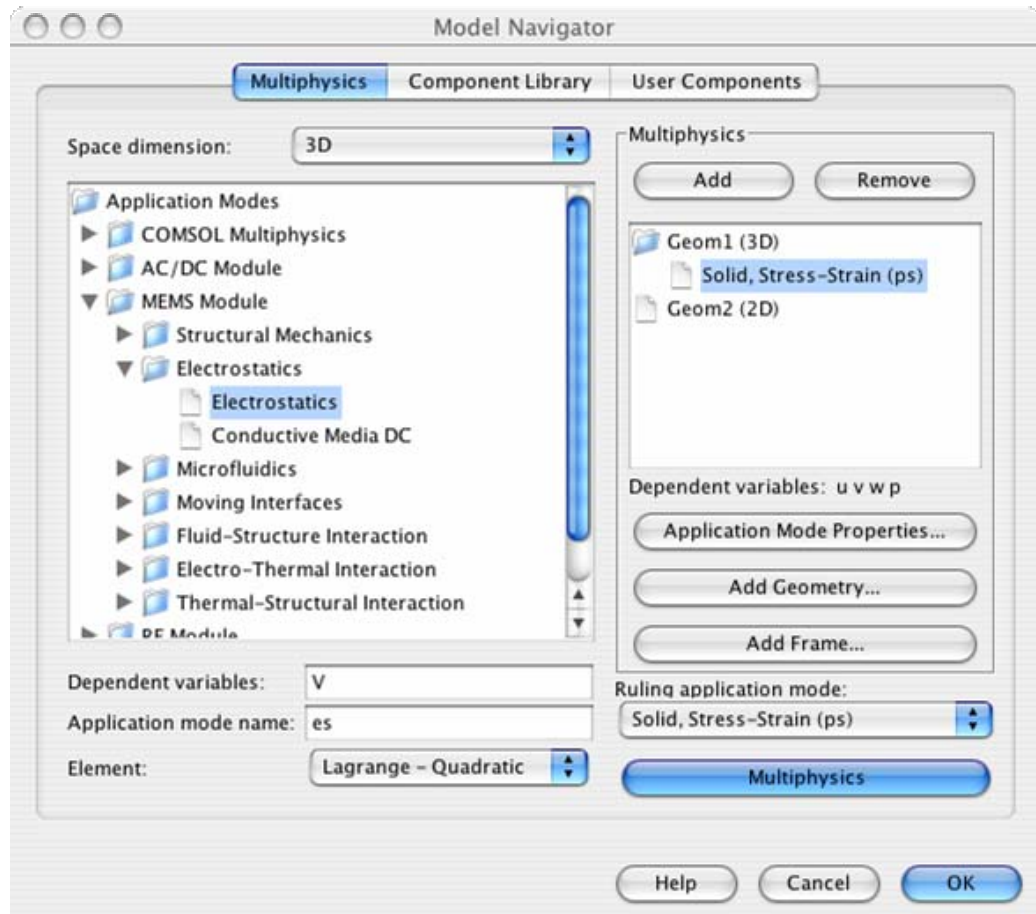


Define the boundary expressions that were just added by going to “*Options*” and selecting “*Expressions > Boundary Expressions*”. Select Boundaries 2 through 5 and type in the following equations.

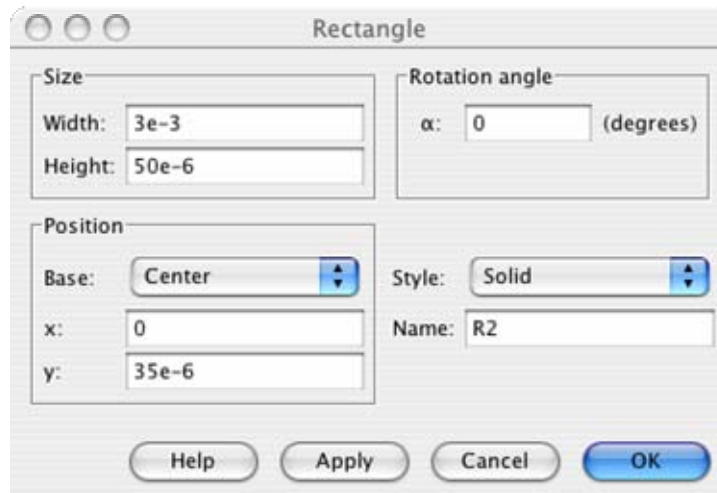


Set the constant for the pull-down voltage by going to “*Options > Constants*” and enter in **Vbeam** as the “*Name*” and **10** as the “*Expression*”.

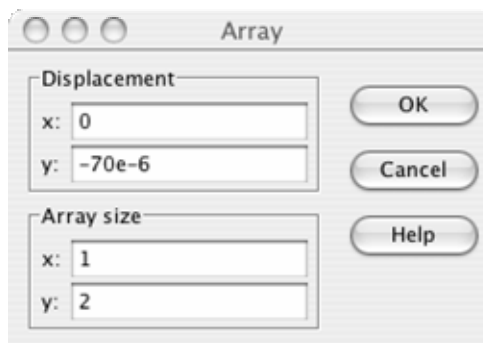
4. The last thing that needs to be done to define the mechanical model is to set large deformation on. Go to the “*Physics*” Menu and select “*Properties...*” and ensure that **Large Deformation** is on.
5. Next, it is necessary to define the Electrostatics portion. Go to “*Multiphysics > Model Navigator*” and add the “*MEMS > Electrostatics > Electrostatics module*” and set the Application mode name to “**es**”. Click **Add** to add the module.



- Next, it is necessary to draw the air that represents the separation distance between micro-ribbons. Go to “*Draw > Work Plane Settings*” and hit **OK**. This will produce the 2D view again. Draw the air gaps by Shift-Clicking the Draw rectangle tool and type in the values shown in the following figure:

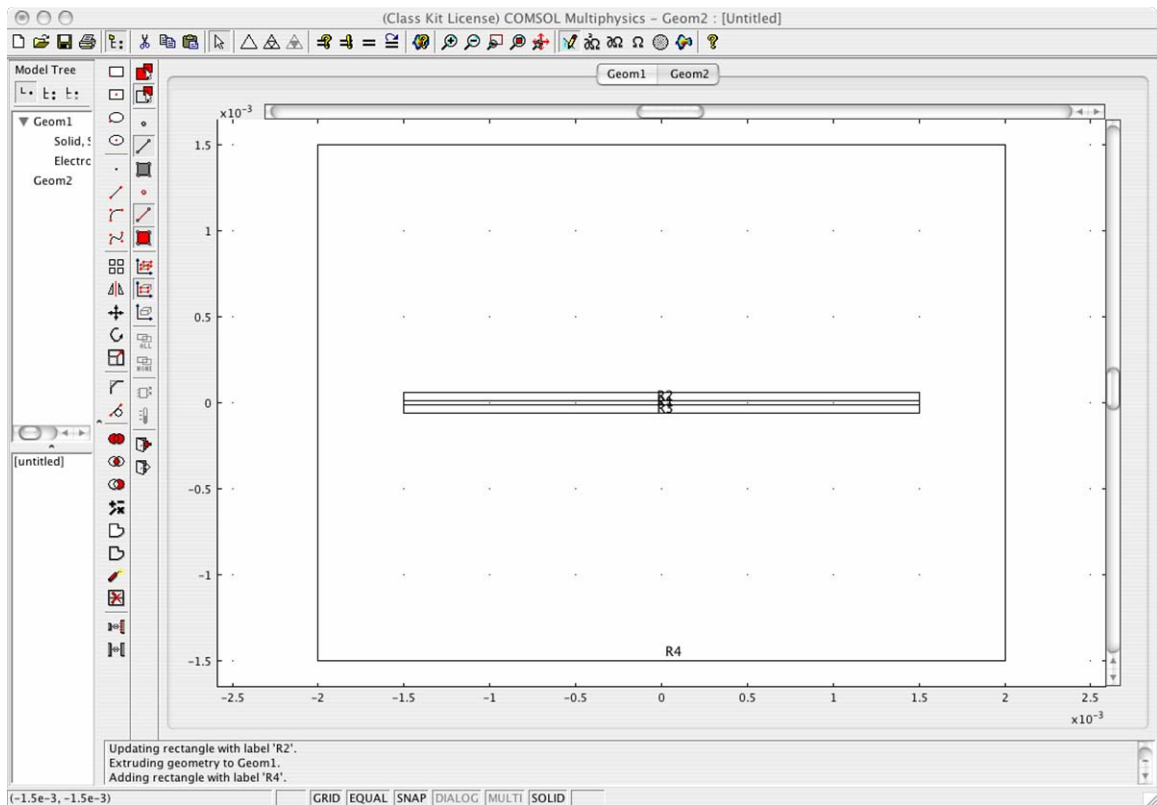


To create the other air gap, click the “array” tool, and enter the following parameters:

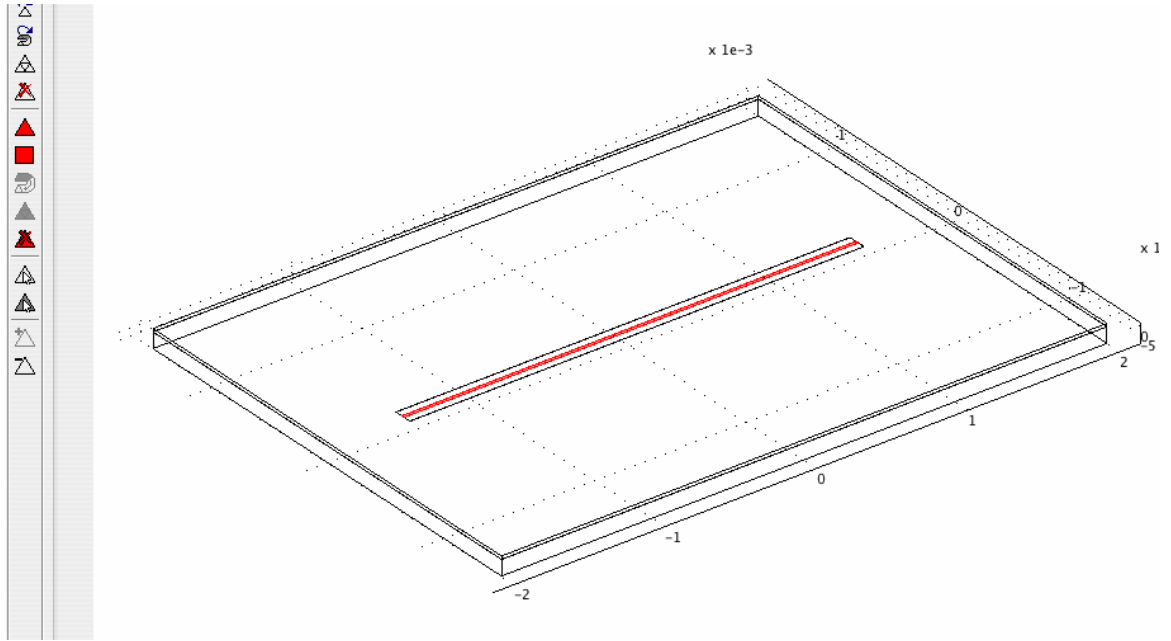


Next, select the 2 newly-drawn rectangles and extrude them **1e-6** in the same manner as in step 2.

7. To draw the ground structure, go to “*Draw > Work Plane Settings...*” and enter **-100e-6** for the z dimension and click **OK**. Next, draw a rectangle with the dimension 4 mm x 3 mm. The resulting screen display should be as follows:



Extrude the ground rectangle **100 μm** with the same procedure as in Step 2. Next, go to “*Draw > Work Plane Settings...*” and enter **1e-6** for the z dimension and click **OK**. Extrude the ground plane rectangle **20 μm** . The following figure should result. All the CAD is now complete.



8. To set the subdomain settings, go to “*Physics > Subdomain Settings...*”. Select subdomain 4 and uncheck “**Active in this domain**”. The other subdomain sections are default to “air”. Click **OK**. Go to “*Multiphysics > Mechanical Structures*” and go to subdomain settings again and make subdomain section 4 the only active domain in this domain. Go to “*Multiphysics > Electrostatics*”.
9. To set the boundary settings go to “*Physics > Boundary Settings...*” set the following boundary conditions

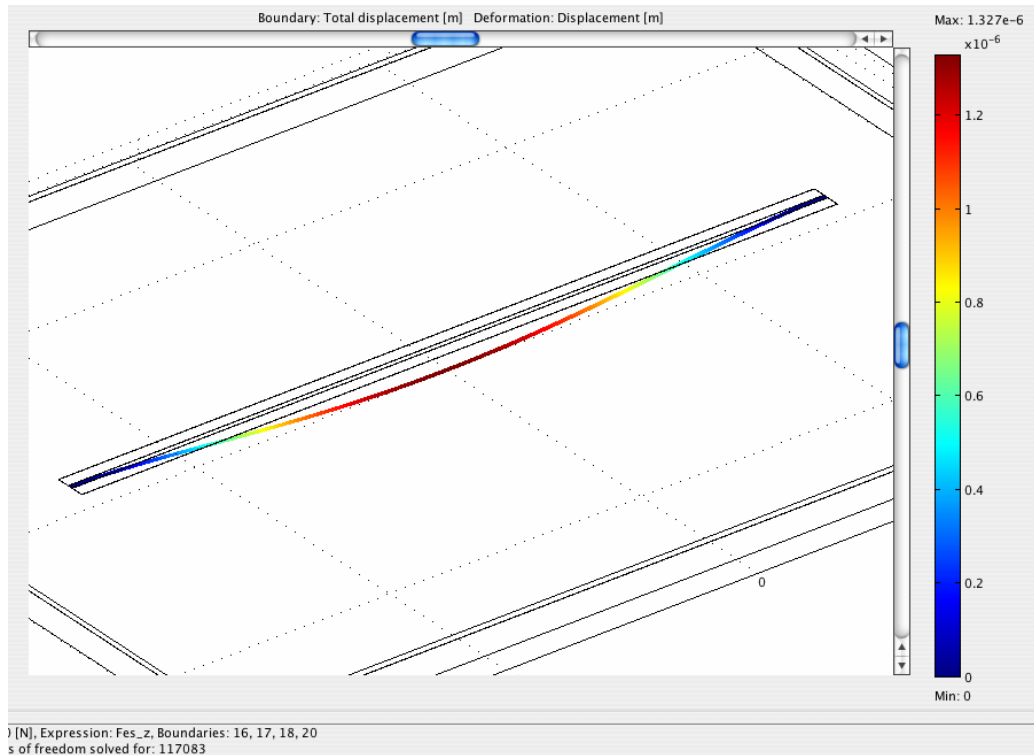
BOUNDARY	CONDITION
1,2,5,6,8,9,10,27,28	ZERO CHARGE/SYM METRY
3	ELECTRIC POTENTIAL > $V_0 = V_{BEAM}$
EVERYTHING ELSE	GROUND

10. Set mesh settings by going to “*Mesh > Free Mesh Parameters*” and select “Extremely coarse” as the predefined mesh size, and Click **OK**. “Mesh elements”

will have the value 59181 and the “Degrees of Freedom” will have the value 382418.

Click **Solve**.

11. To view the maximum deflection, go to “*Postprocessing > Plot Parameters*” and click “deformed shape” and “boundary” and click **OK**. Maximum deflection is $1.327\text{e-}6$ m.



12. To determine the total electrostatic force in the z direction, go to “*Postprocessing > boundary integration*” and select the 4 edges of the micro-ribbon and integrate the expression “**Fes_z**”. This should give a value of $-4.422\text{e-}9$ N.

APPENDIX B – COMSOL SIMULATIONS

Simulations presented in this appendix are meant to supplement the simulations presented in chapter 4 of the thesis. The following tables are some simulations done investigating longer micro-ribbons and different thicknesses:

Table B-1: Simulations done investigating longer micro-ribbons and different thicknesses.

		Aluminum Density	2730	kg/m ³
<u>3mm Ribbons - 4 segments at 22.5</u>				
width = 20 um		length = 3.247 mm		
Thickness (um)	Pressure (N/m ²)	Electrostatic Force (N)	Maximum Deflection (m)	ω (Hz)
1	1.5398	1.02E-07	2.33E-05	790.6705034
1.5	1.5398	1.02E-07	1.43E-05	822.6022205
2	1.5398	1.02E-07	7.34E-06	995.1834945
<u>6 mm Ribbons - 8 segments at 22.5</u>				
width = 20 um		length = 6.494 mm		
Thickness (um)	Pressure (N/m ²)	Electrostatic Force (N)	Maximum Deflection (m)	ω (Hz)
1	1.5398	2.03E-07	6.84E-05	460.8756318
1.5	1.5398	2.03E-07	5.66E-05	413.8375697
2	1.5398	2.03E-07	4.69E-05	393.7297369
<u>9 mm Ribbons - 12 segments at 22.5</u>				
width = 20 um		length = 9.742 mm		
Thickness (um)	Pressure (N/m ²)	Electrostatic Force (N)	Maximum Deflection (m)	ω (Hz)
1	1.5398	3.05E-07	1.21E-04	346.2847891
1.5	1.5398	3.05E-07	1.03E-04	306.853731
2	1.5398	3.05E-07	9.00E-05	284.1347465
2.5	1.5398	3.05E-07	7.99E-05	269.7543832
3	1.5398	3.05E-07	7.04E-05	262.3424772
<u>"Large Deformation" Off</u>				
Length (mm)	Thickness (um)	Pressure (N/m ²)	Electrostatic Force (N)	Maximum Deflection (m)
3	2	1.5398	1.02E-07	7.64E-06
6	2	1.5398	2.03E-07	1.24E-04
9	2	1.5398	3.05E-07	6.30E-04
			k	Mass
			1.33E-02	3.5457E-10
			1.64E-03	7.0914E-10
			4.84E-04	1.0638E-09
			k	Mass
			2.52E-03	5.3191E-10
			2.96E-03	7.9787E-10
			3.39E-03	1.0638E-09
			3.82E-03	1.3298E-09
			4.33E-03	1.5957E-09
			k	Mass
			4.37E-03	1.7729E-10
			7.10E-03	2.6593E-10
			1.38E-02	3.5457E-10

Table C-3: CF₄ under cut and under cut rate.

Recipe	Under cut (µm)			Under cut Rate (µm/min)		
	5 min	10 min	15 min	5 min	10 min	15 min
1	1	2	3	0.2	0.2	0.2
2	1	2.5	4.25	0.2	0.3	0.35
3	0.5	2	2.5	0.1	0.3	0.1
4	1.25	3.25	6	0.25	0.4	0.55
5	2	4.5	7	0.4	0.5	0.5

Table C-4: CF₄ silicon etch depth and silicon etch rate.

Recipe	Silicon Etched (µm)			Silicon Etch Rate (µm/min)		
	5 min	10 min	15 min	5 min	10 min	15 min
1	2.136	4.1855	6.0892	0.4272	0.4099	0.3807
2	2.5059	4.8289	7.2657	0.5012	0.4646	0.4874
3	1.3044	2.646	3.9325	0.2609	0.26832	0.2573
4	2.3965	5.5323	9.0159	0.4793	0.62716	0.69672
5	3.1785	6.6763	9.769	0.6357	0.69956	0.61854

Table C-5: Overall Rates for the CF₄ recipes.

Recipe	Oxide Etch Rate (µm/min)	Silicon Etch Rate (µm/min)	Under cut Rate (µm/min)	Under cut:Silicon Ratio
1	0.0121	0.4506	0.2	0.4927
2	0.0129	0.4844	0.2833	0.5849
3	0.0080	0.2622	0.1667	0.6357
4	0.0162	0.6011	0.4	0.6655
5	0.0198	0.6513	0.4667	0.7166

Table C-6: SF₆ Etch Recipes and the raw data.

Recipe	Pres. (mTorr)	SF6	O2	ICP (W)	RIE (W)	In. Oxide	In. Depth	Time 1	Depth	Oxide	UC	Time 2	Depth	Oxide	UC	Time 3	Depth	Oxide	UC
1	300	30	0	50	50	2.0236	2.014	5	3.453	2.0074	2	5	4.743	2.0032	4	5	5.742	1.9985	5
2	300	30	0	0	50	2.024	2.013	5	2.728	2.0204	2	5	3.23	2.0194	3	5	3.768	2.0178	4
3	300	30	0	200	30	2.025	2.014	5	9.252	2.0178	5	10	18	2.0052	13				
4	300	50	0	200	50	2.025	2.031	5	5.725	2.0171	2	10	15	2.0079	9				
5	300	30	5	200	50	2.0238	2.013	5	4.08	1.9794	1.5	10	7.797	1.8853	4				
6	300	30	0	500	50	2.0234	2.011	5	14.93	2.0006	11	10	50	1.9319	31				
3B	300	30	0	200	50	2.0232	2.027	5	10.36	2.0116	5	10	20	1.9954	12				
7	300	30	0	200	100	2.023	1.995	5	11.86	2.0117	6	10	24	1.9954	11				
8	300	30	0	50	50	2.0229	2.016	5	2.648	2.0196	2	25	4.293	2.0122	2				
8B	300	30	0	200	50	2.0218	2.015	5	4.313	2.0136	4	25	42	1.9867	24				
9	50 (45)	30	0	50	50	2.0236	2.003	10	18	1.9048	6								
10	50 (45)	30	0	200	50	2.0239	2.017	10	30	1.7382	20								
11	50 (45)	30	0	50	100	2.0223	1.984	10	30	1.5549	17								
12	10 (16)	30	0	50	50	2.0261	2.097	10	17.19	1.8878	10								
13	10 (16)	30	0	50	100	2.0227	2.006	10	23	1.6172	16								

Etch depths, oxide thickness and undercut (UC) are all in μm.

Time is in minutes.

SF₆ and O₂ flow rates are in sccm.

Rates are all μm/min.

Table C-7: SF₆ raw data for the oxide etch rate, silicon etch rate and undercut rate.

Recipe	Time 1	Si Rate 1	SiO2 Rate 1	UC Rate 1	Time 2	Si Rate 2	SiO2 Rate 2	UC Rate 2	Time 3	Si Rate 3	SiO2 Rate 3	UC Rate 3
1	5	0.28912	0.00324	0.4	5	0.25884	0.00084	0.4	5	0.20074	0.00094	0.2
2	5	0.14152	0.00072	0.4	5	0.1006	0.0002	0.2	5	0.10792	0.00032	0.2
3	5	1.44684	0.00144	1	10	0.87606	0.00126	0.8				
4	5	0.74158	0.00158	0.4	10	0.92842	0.00092	0.7				
5	5	0.42012	0.00888	0.3	10	0.38111	0.00941	0.25				
6	5	2.58588	0.00456	2.2	10	3.51387	0.00687	2				
3B	5	1.66968	0.00232	1	10	0.96562	0.00162	0.7				
7	5	1.96966	0.00226	1.2	10	1.21563	0.00163	0.5				
8	5	0.12568	0.00066	0.4	25	0.066096	0.000296	0				
8B	5	0.45988	0.00164	0.8	25	1.508556	0.001076	0.8				
9	10	1.60952	0.01188	0.6								
10	10	2.82618	0.02857	2								
11	10	2.84451	0.04674	1.7								
12	10	1.53022	0.01383	1								
13	10	2.13828	0.04055	1.6								

Recipe	Time 1	Si Rate 1	Time 2	Si Rate 2	Time 3	Si Rate 3	Recipe	Time 1	SiO2 Rate 1	Time 2	SiO2 Rate 2	Time 3	SiO2 Rate 3
1	5	0.28912	5	0.25884	5	0.20074	1	5	0.00324	5	0.00084	5	0.00094
2	5	0.14152	5	0.1006	5	0.10792	2	5	0.00072	5	0.0002	5	0.00032
3	5	1.44684	10	0.87606			3	5	0.00144	10	0.00126	5	0.00094
4	5	0.74158	10	0.92842			4	5	0.00158	10	0.00092	5	0.00032
5	5	0.42012	10	0.38111			5	5	0.00888	10	0.00941	5	0.00094
6	5	2.58588	10	3.51387			6	5	0.00456	10	0.00687	5	0.00094
3B	5	1.66968	10	0.96562			3B	5	0.00232	10	0.00162	5	0.00094
7	5	1.96966	10	1.21563			7	5	0.00226	10	0.00163	5	0.00094
8	5	0.12568	25	0.066096			8	5	0.00066	25	0.000296	5	0.00094
8B	5	0.45988	25	1.508556			8B	5	0.00164	25	0.001076	5	0.00094
9	10	1.60952					9	10	0.01188			5	0.00094
10	10	2.82618					10	10	0.02857			5	0.00094
11	10	2.84451					11	10	0.04674			5	0.00094
12	10	1.53022					12	10	0.01383			5	0.00094
13	10	2.13828					13	10	0.04055			5	0.00094

Table C-8: SF₆ raw data for the undercut rate, si/oxide etch ratios and the lateral to vertical etch ratios.

Recipe	Time 1	UC Rate 1	Time 2	UC Rate 2	Time 3	UC Rate 3	Recipe	Time 1	Si/SiO ₂ 1	Time 2	Si/SiO ₂ 2	Time 3	Si/SiO ₂ 3
1	5	0.4	5	0.4	5	0.2	1	5	89.234568	5	308.14286	5	213.55319
2	5	0.4	5	0.2	5	0.2	2	5	196.55556	5	503	5	337.25
3	5	1	10	0.8			3	5	1004.75	10	695.28571		
4	5	0.4	10	0.7			4	5	469.35443	10	1009.1522		
5	5	0.3	10	0.25			5	5	47.310811	10	40.500531		
6	5	2.2	10	2			6	5	567.07895	10	511.48035		
3B	5	1	10	0.7			3B	5	719.68966	10	596.06173		
7	5	1.2	10	0.5			7	5	871.53097	10	745.78528		
8	5	0.4	25	0			8	5	190.42424	25	223.2973		
8B	5	0.8	25	0.8			8B	5	280.41463	25	1402.0037		
9	10	0.6					9	10	135.48148				
10	10	2					10	10	98.921246				
11	10	1.7					11	10	60.858151				
12	10	1					12	10	110.64497				
13	10	1.6					13	10	52.731936				

Recipe	Time 1	UC Ratio 1	Time 2	UC Ratio 2	Time 3	UC Ratio 3
1	5	1.3835086	5	1.5453562	5	0.9963136
2	5	2.8264556	5	1.9880716	5	1.8532246
3	5	0.6911614	10	0.9131795		
4	5	0.5393889	10	0.7539691		
5	5	0.7140817	10	0.6559786		
6	5	0.8507742	10	0.569173		
3B	5	0.5989172	10	0.7249228		
7	5	0.6092422	10	0.4113094		
8	5	3.1826862	25	0		
8B	5	1.7395842	25	0.5303085		
9	10	0.3727819				
10	10	0.707669				
11	10	0.5976425				
12	10	0.6535008				
13	10	0.748265				

APPENDIX D – HFSS SIMULATIONS

This section is meant to supplement the HFSS simulations presented in chapter 7 of the thesis. A transmission line with line impedance of 30Ω lines with a width of $520 \mu\text{m}$ was also simulated.

30 Ω Line:

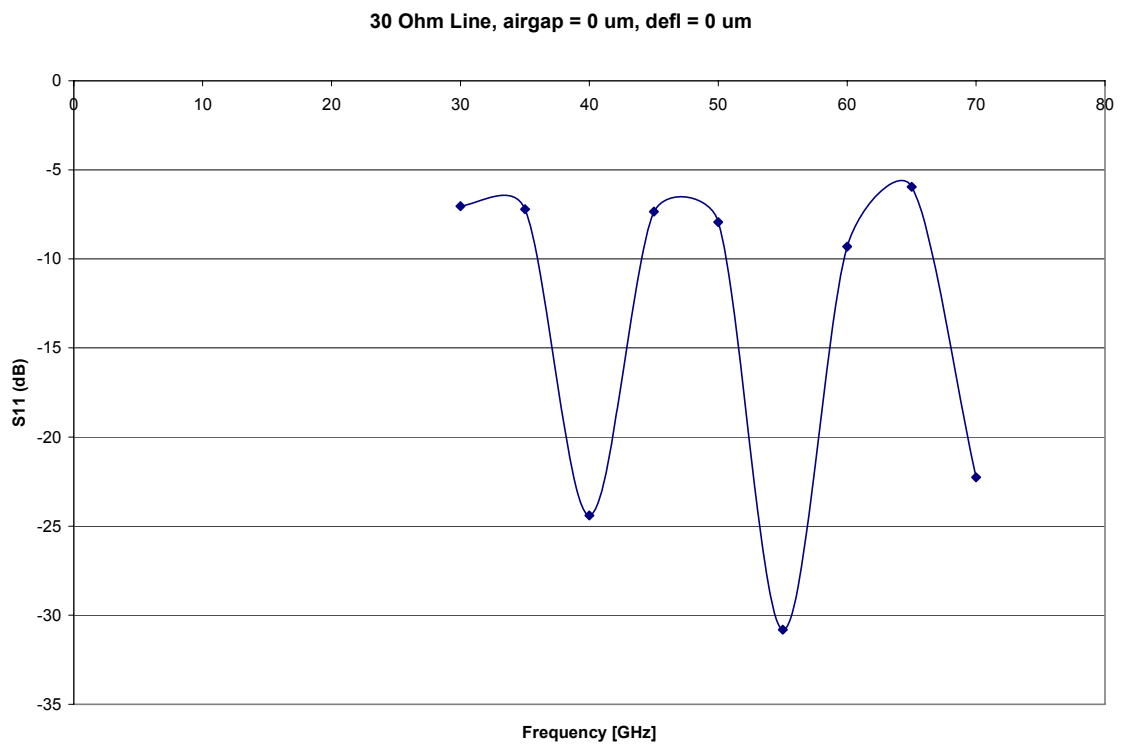


Fig. D.1: Simulated 30Ω transmission line S_{11} .

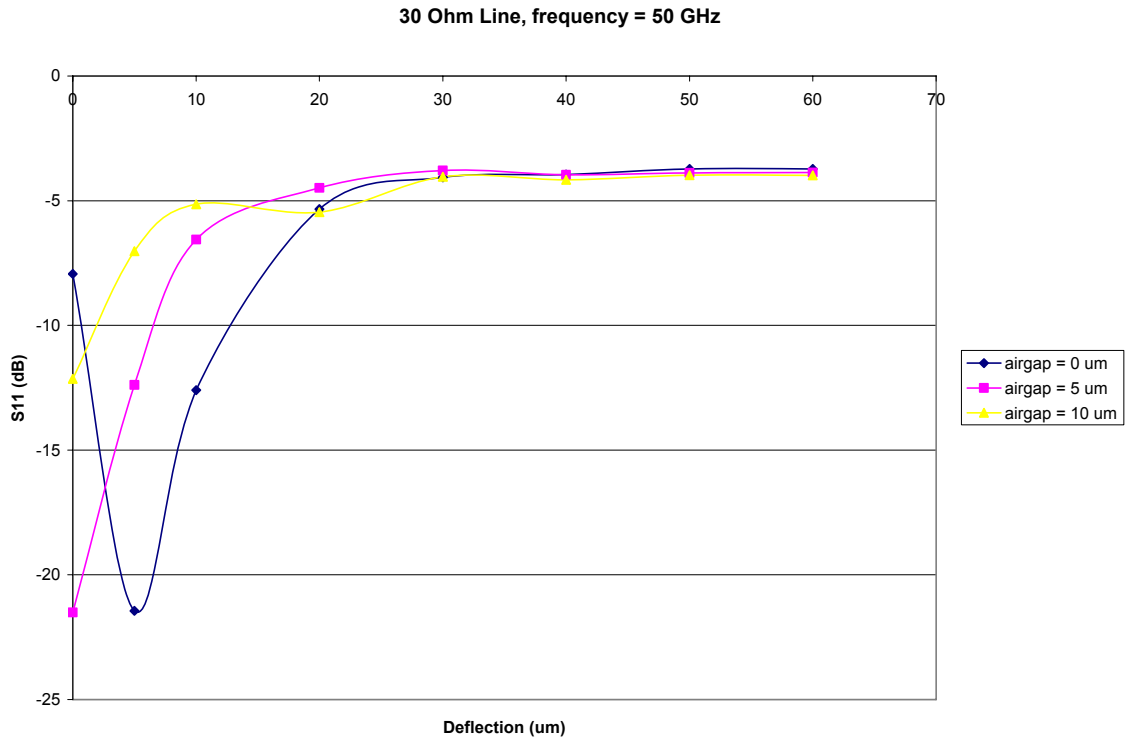


Fig. D.2: Simulated 30 Ω transmission line S₁₁ for different deflections at 50 GHz.

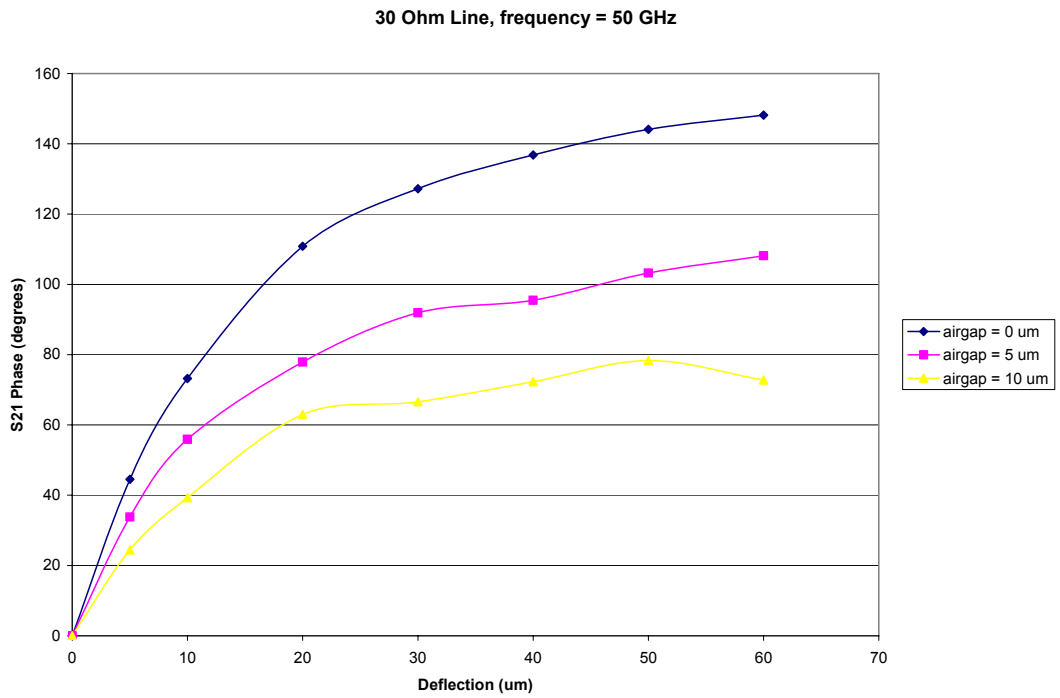


Fig. D.3: Simulated 30 Ω transmission line differential S_{21} phase for different air gaps.

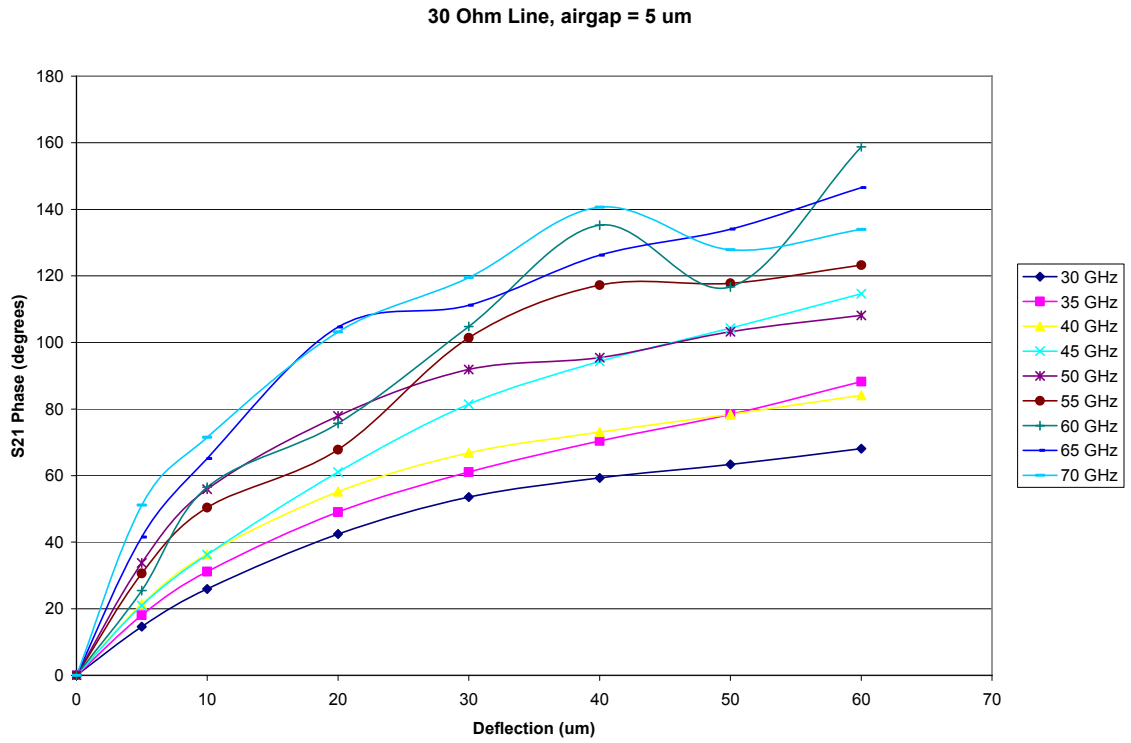


Fig. D.4: Simulated 30 Ω transmission line differential S_{21} phase for a 5 μm initial air gap for different deflections for different frequencies.

50 Ω Line:

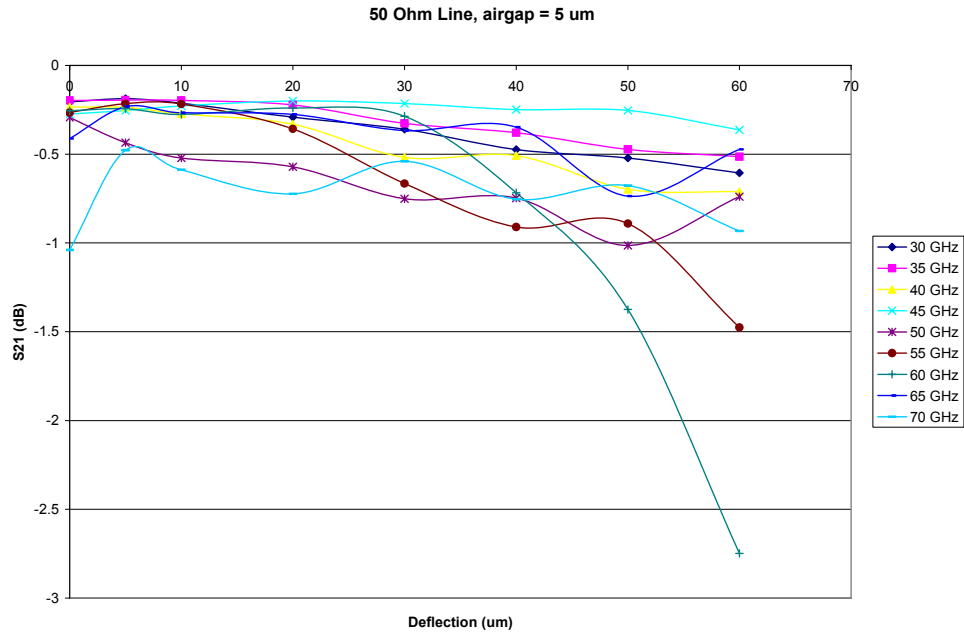


Fig. D.5: Simulated S₂₁ for an initial air gap of 5 μm for different frequencies vs. deflection.

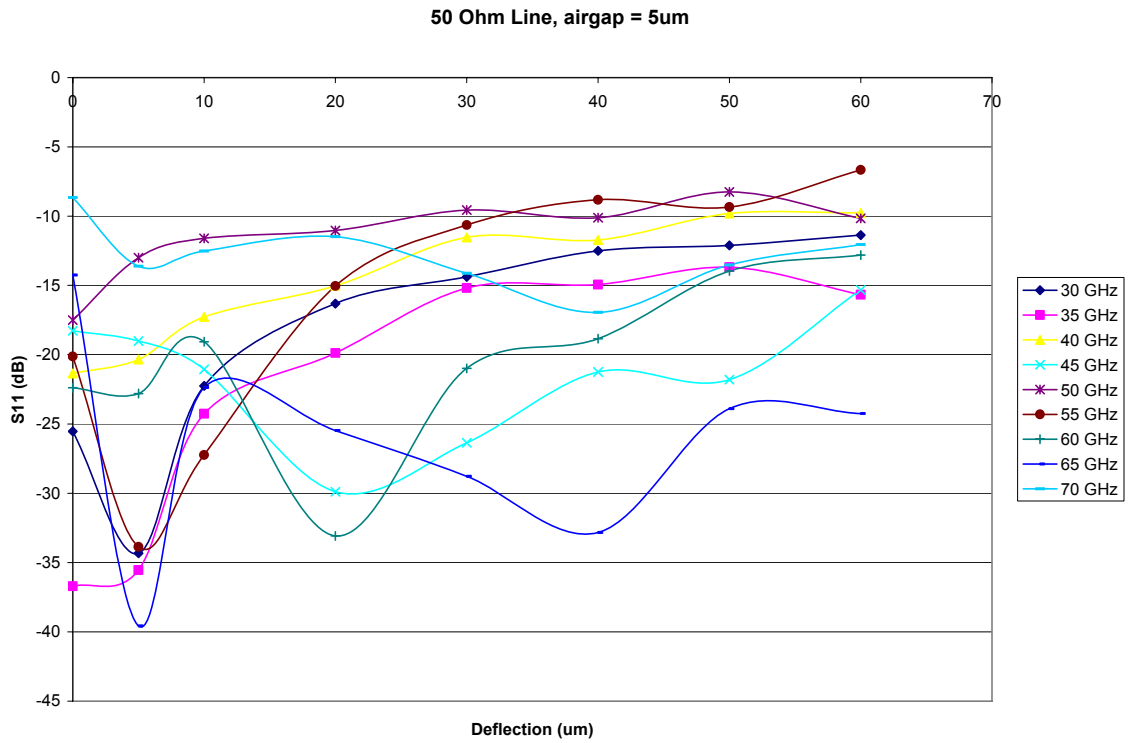


Fig. D.6: Simulated S₁₁ for an initial air gap of 5 μm for different frequencies vs. deflection.

37 Ω Line:

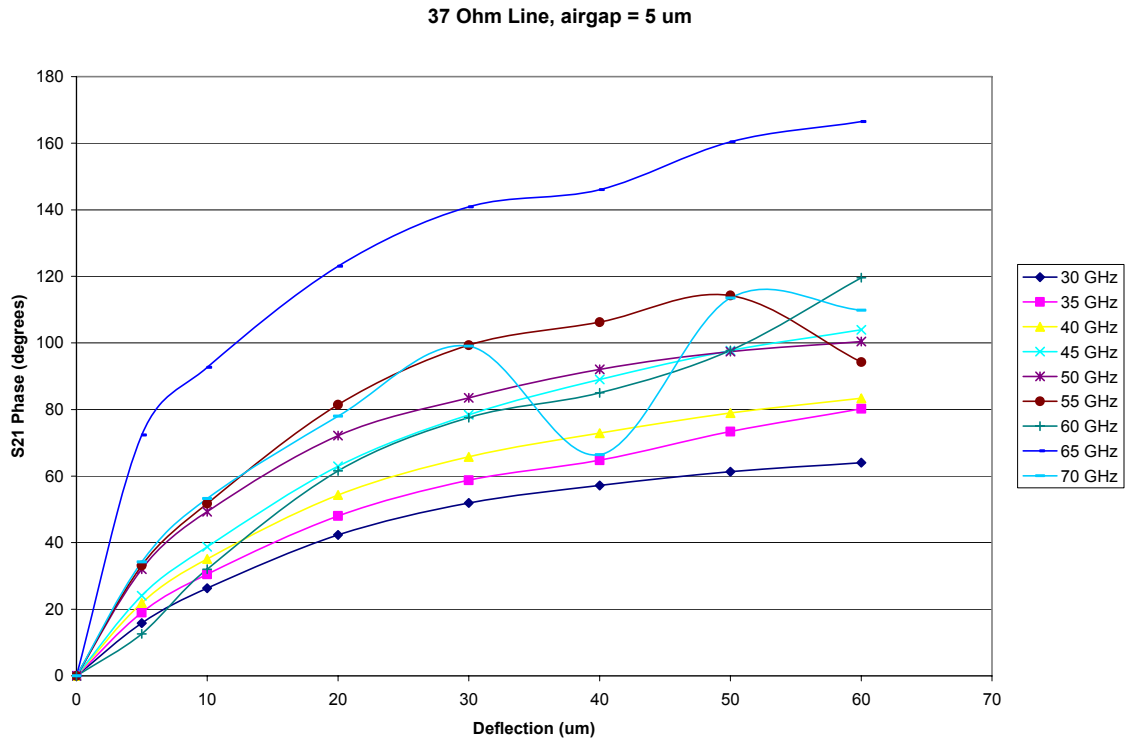


Fig. D.7: Simulated S_{21} differential phase for an initial air gap of 5 μm for different frequencies vs. deflection

APPENDIX E – PHASE SHIFT MEASUREMENT DATA

The following figures are screen shots from the measurements taken on the two different sets of 20 μm wide micro-ribbons.

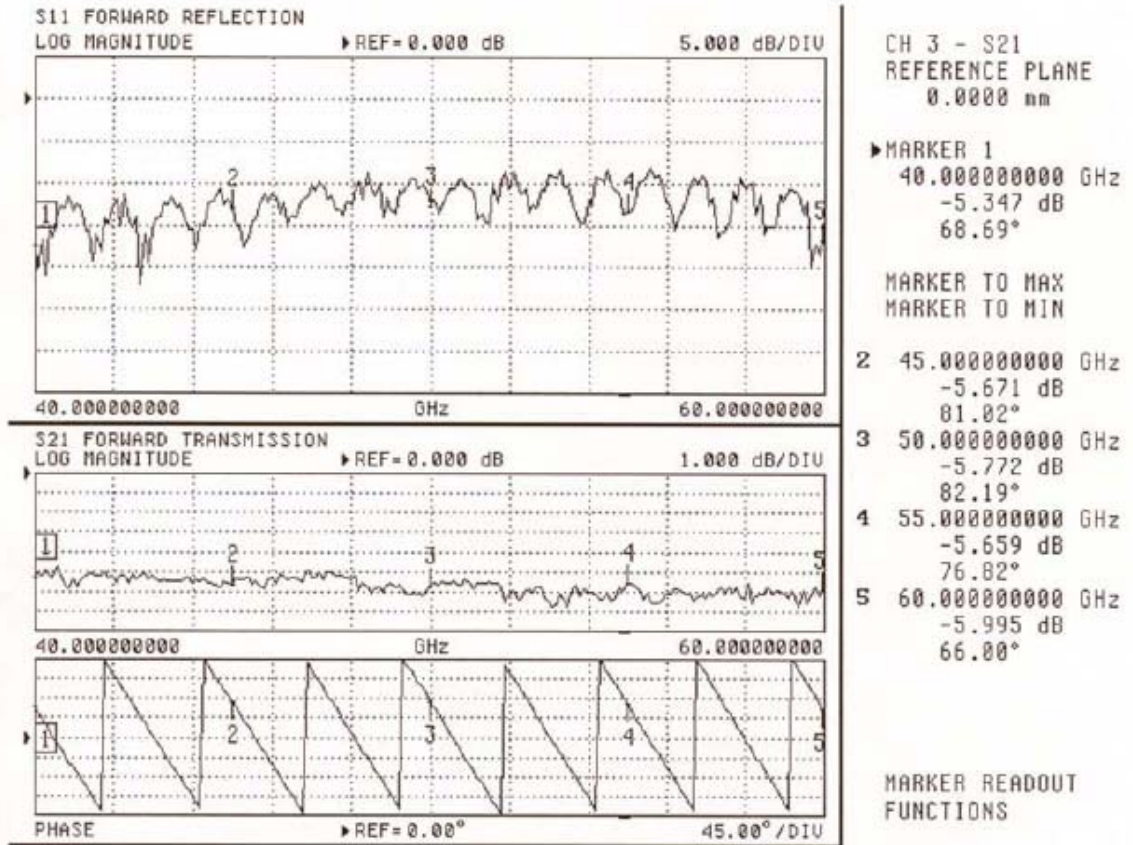
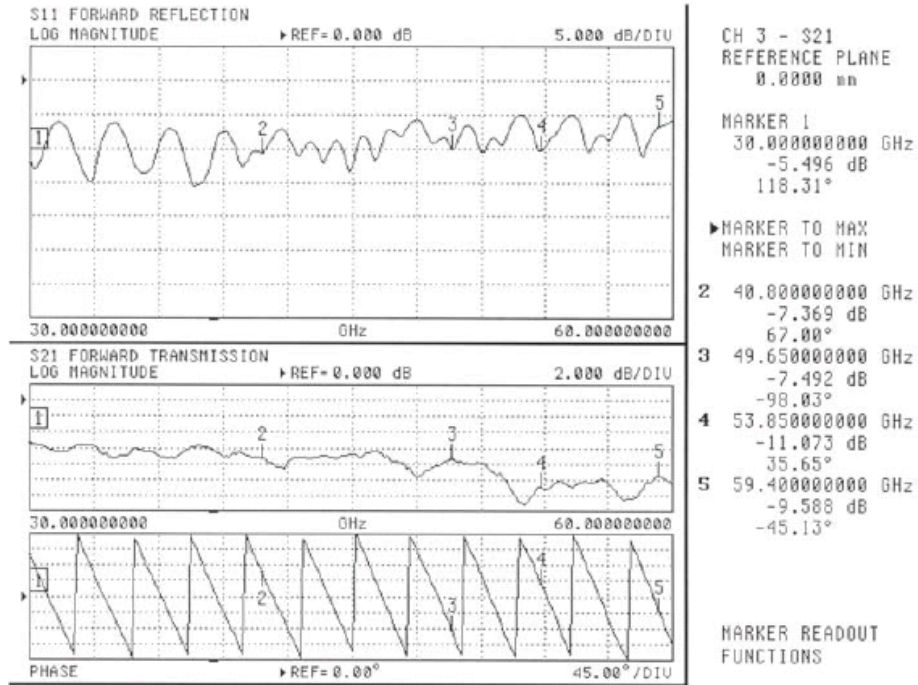
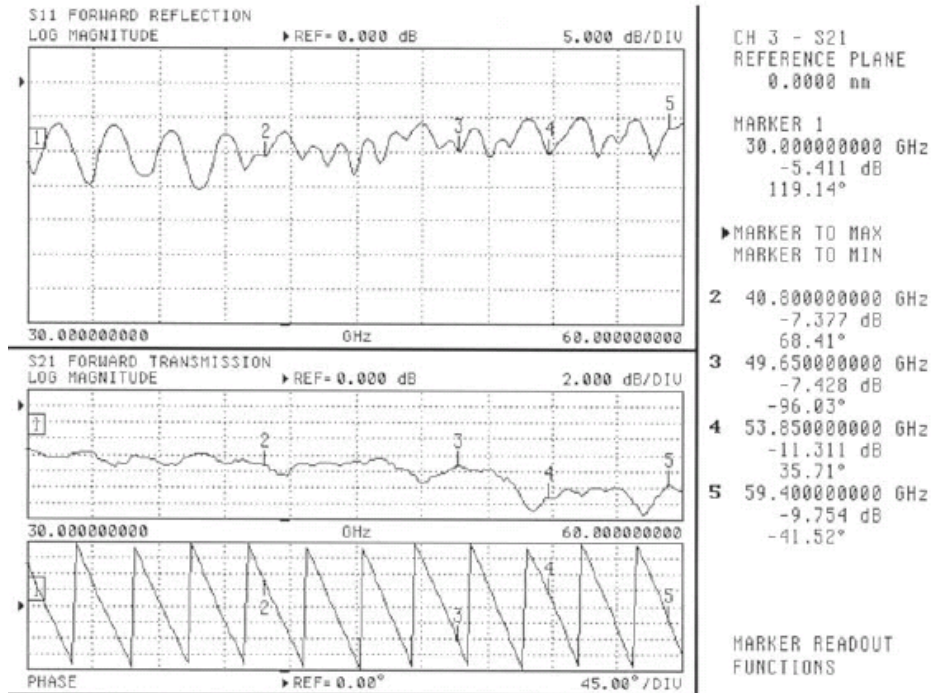


Fig. E.1: Measured return loss (S_{11}), insertion loss (S_{21}) for a reference transmission line with no micro-ribbon array.

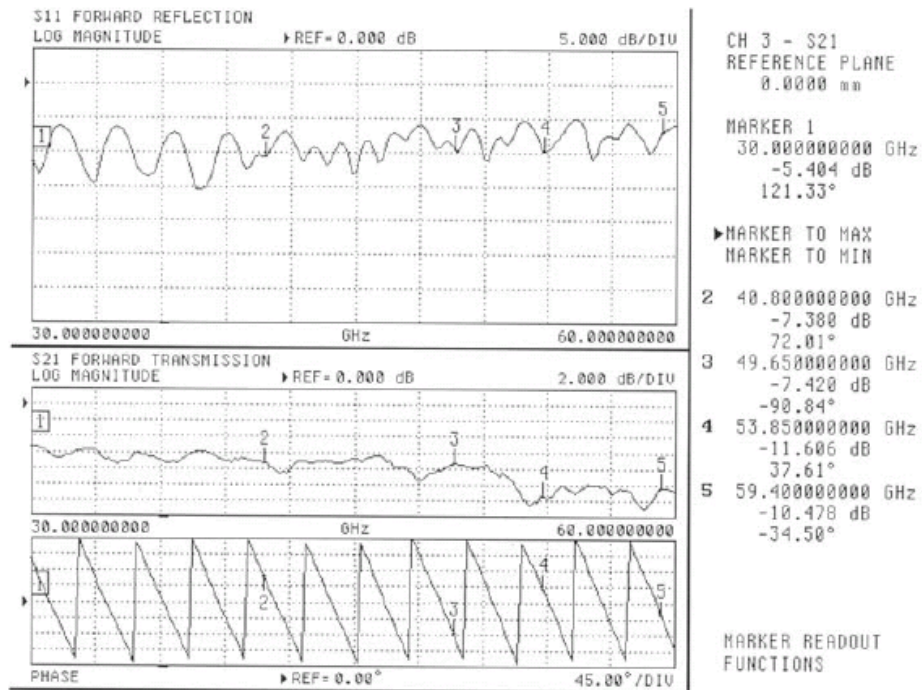
Set 1:



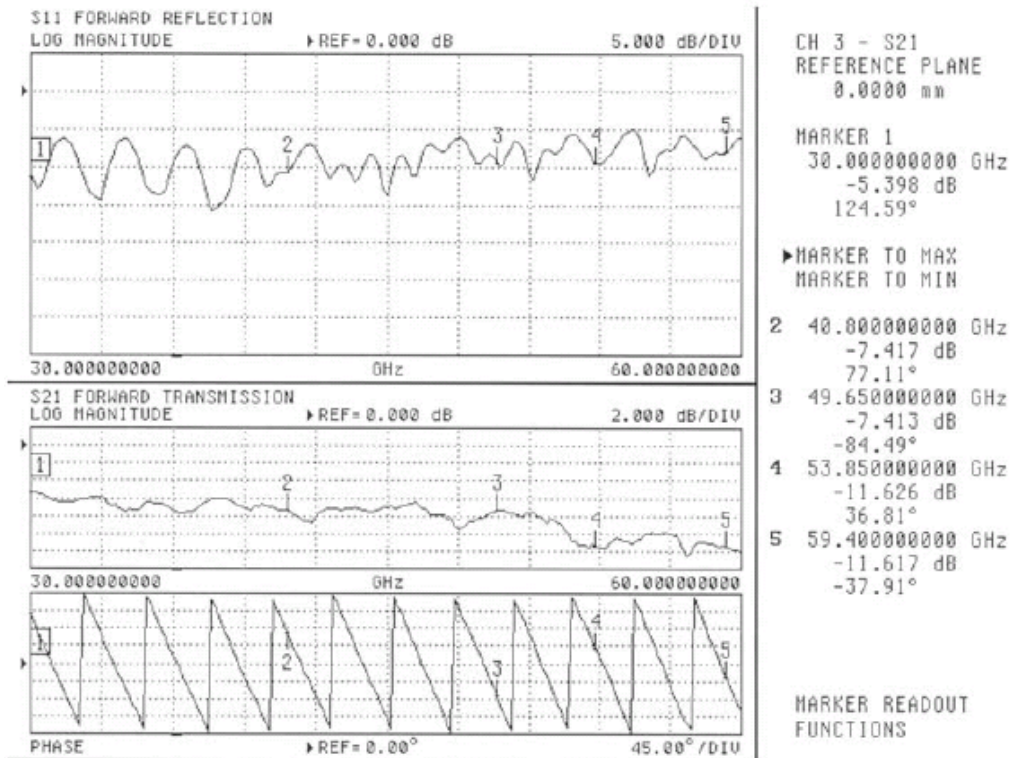
(a) 0 Volt



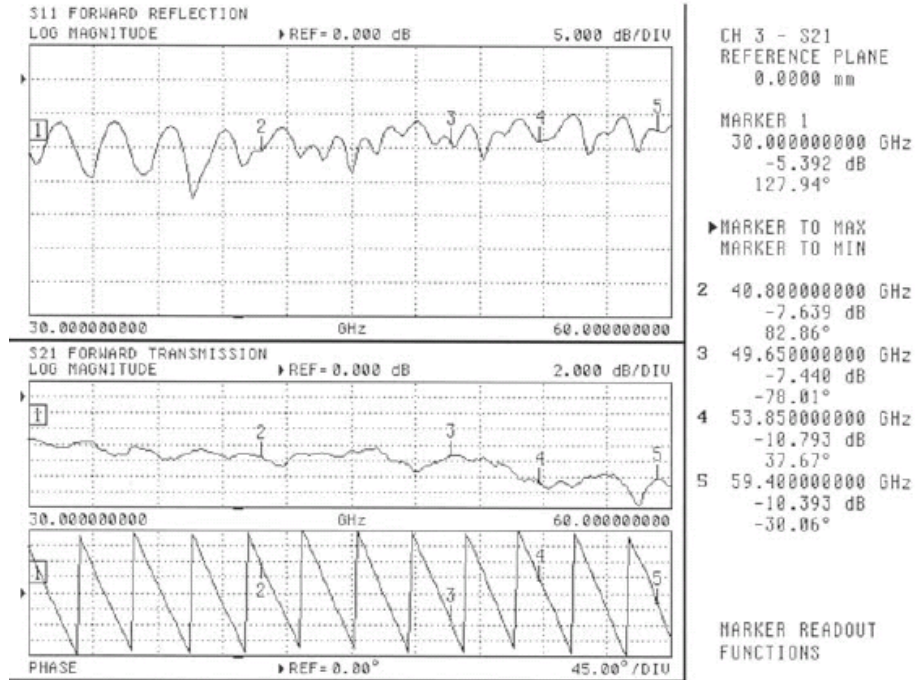
(b) 30 Volt



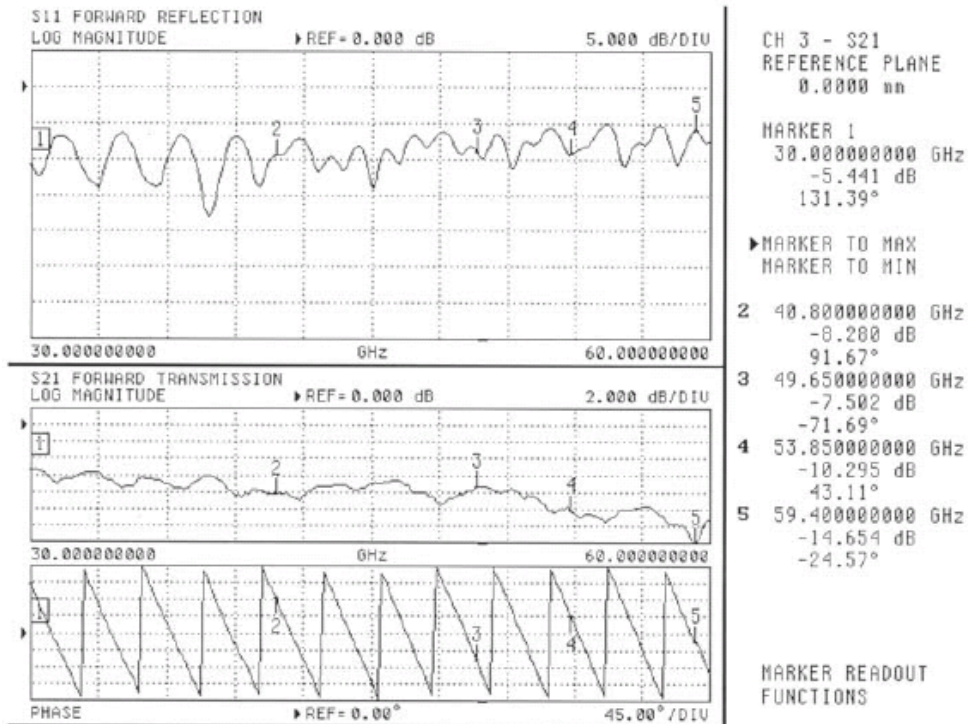
(c) 40 Volt



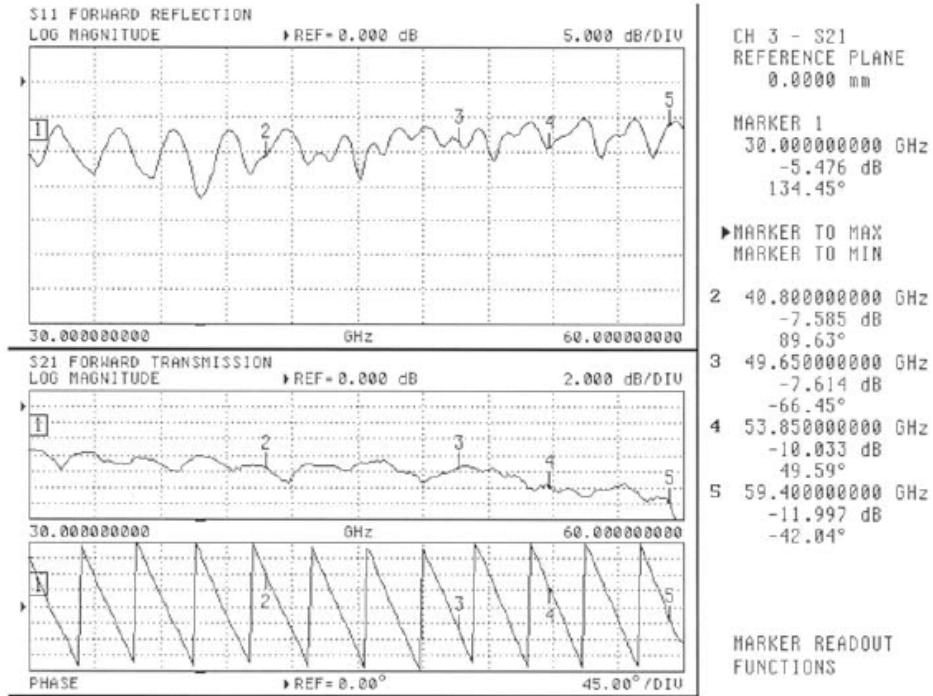
(d) 50 Volt



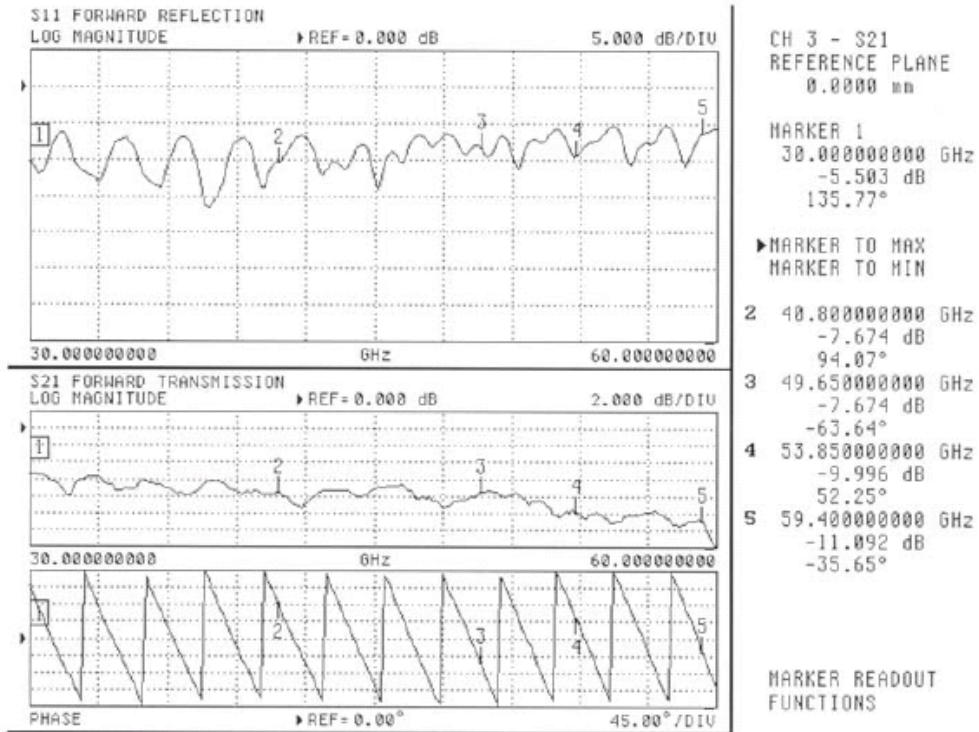
(e) 60 Volt



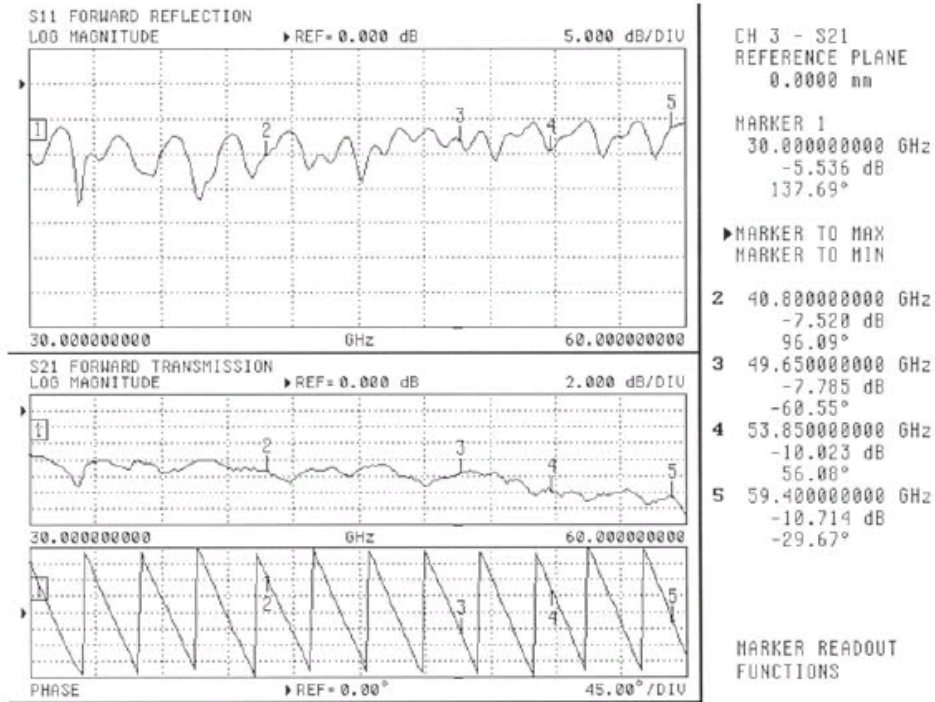
(f) 70 Volt



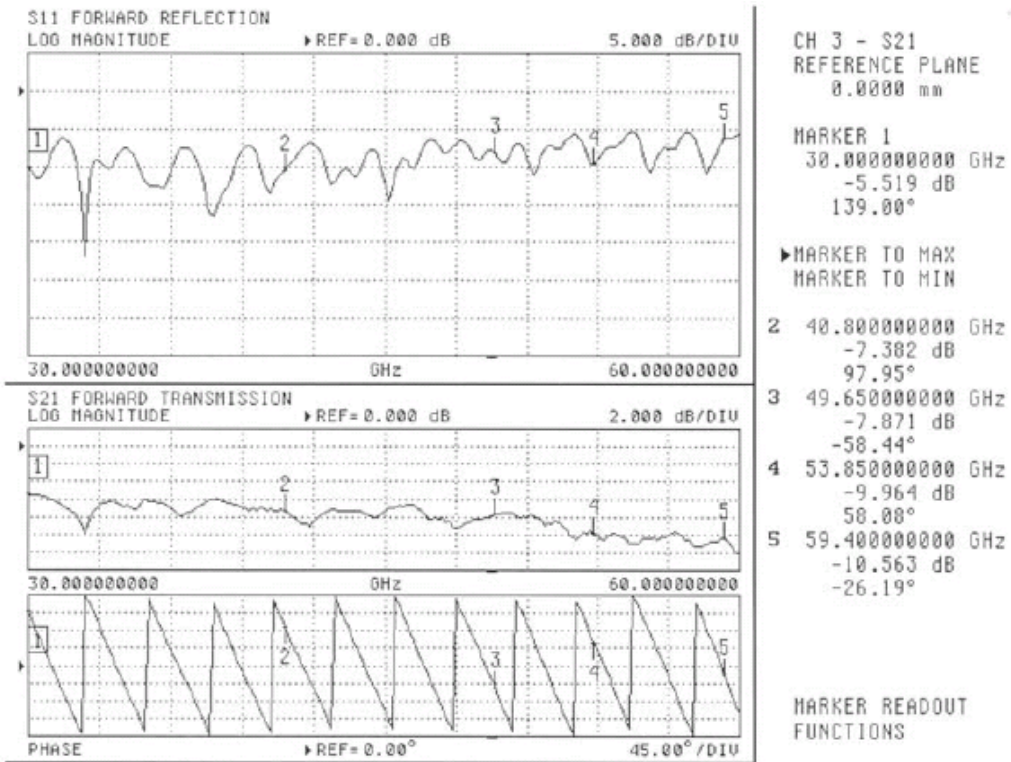
(g) 80 Volt



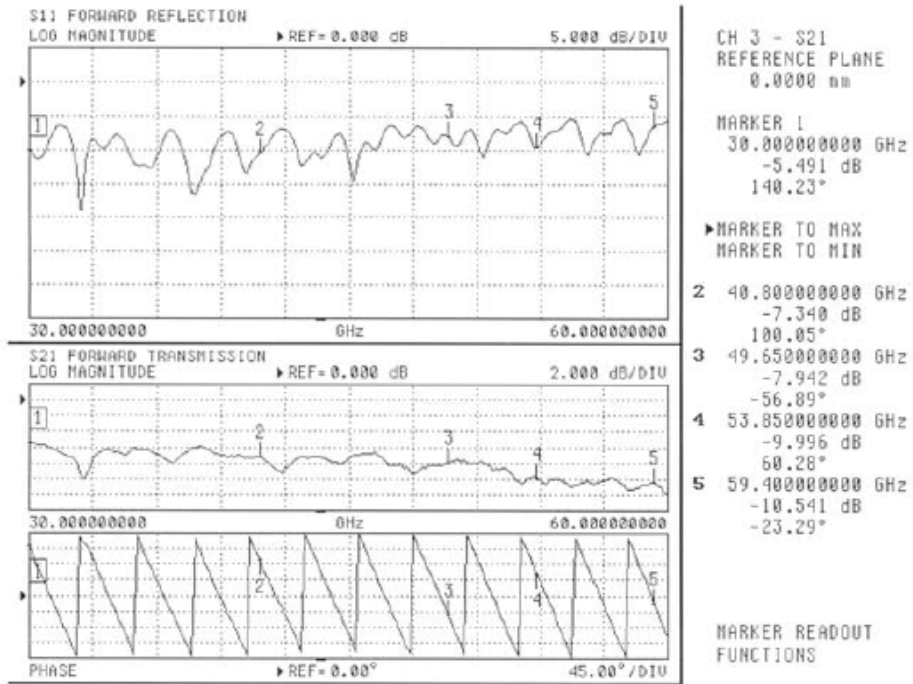
(h) 90 Volt



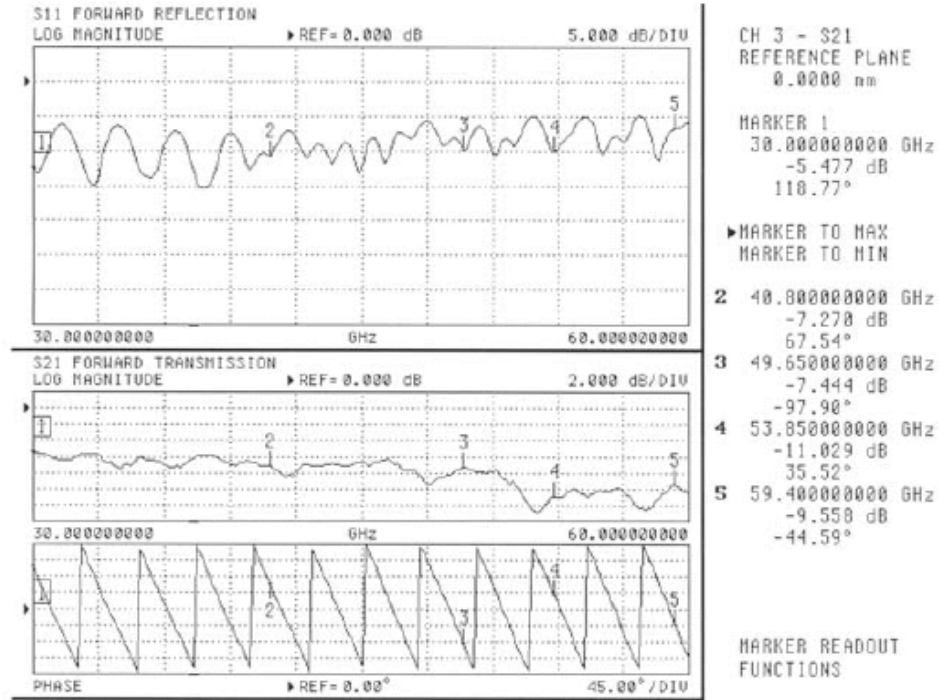
(i) 100 Volt



(j) 110 Volt



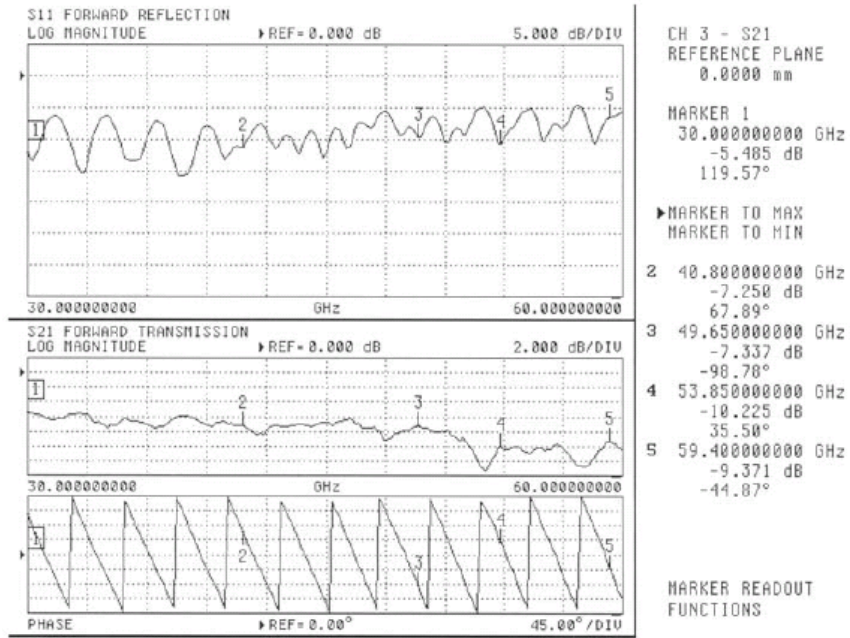
(k) 120 Volt



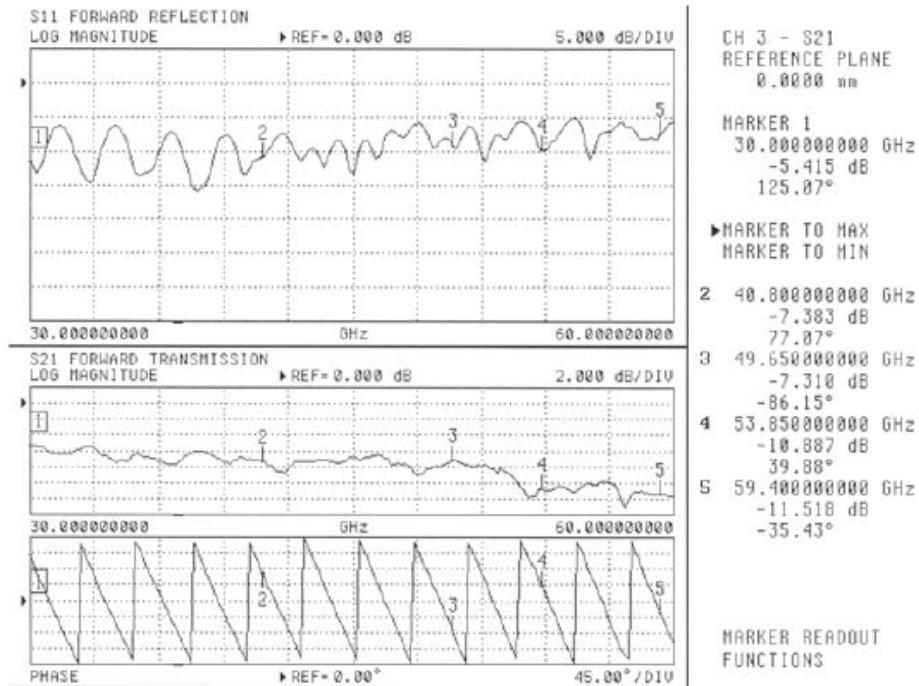
(l) Reversed to 0 Volt

Fig. E.2: Set1 - The measured return loss (S_{11}), insertion loss (S_{21}) and insertion phase (S_{21}) of the single membrane phase shifter with the electrostatic actuation at the electrode from (a) 0 V, (b) 30 V, (c) 40 V, (d) 50 V, (e) 60 V, (f) 70 V, (g) 80 V, (h) 90 V, (i) 100 V, (j) 110 V, (k) 120 v, and (l) Reversed 0 V cases.

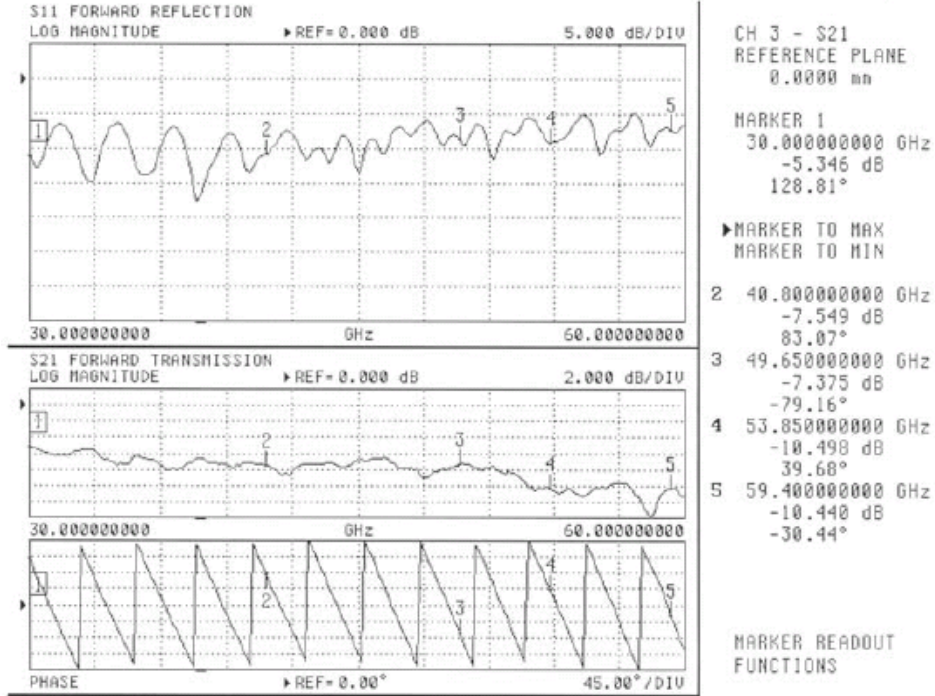
Set 2:



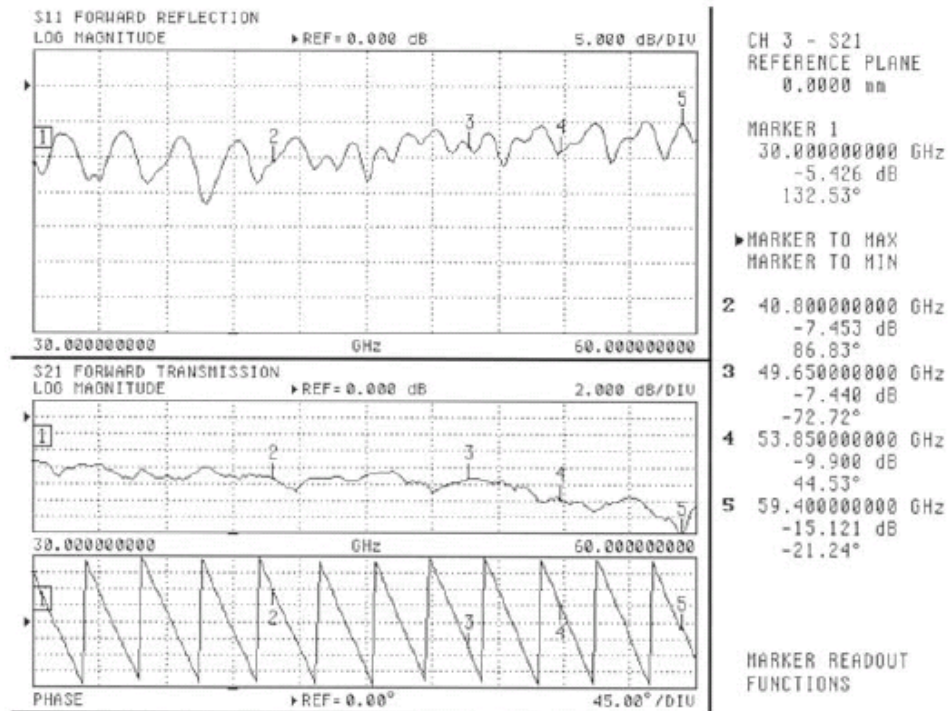
(a) 0 Volt



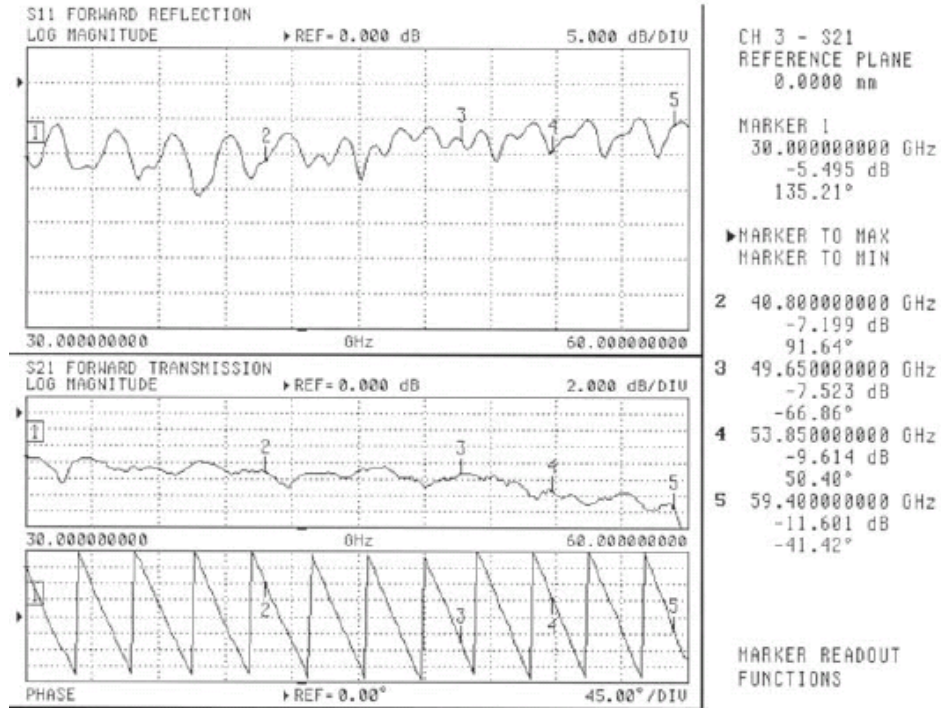
(b) 50 Volt



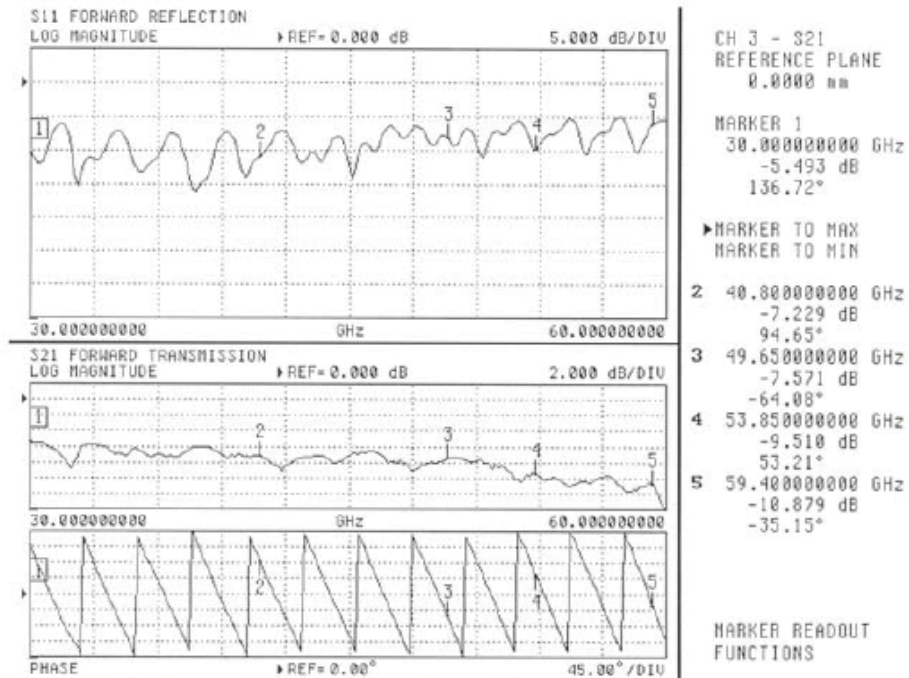
(c) 60 Volt



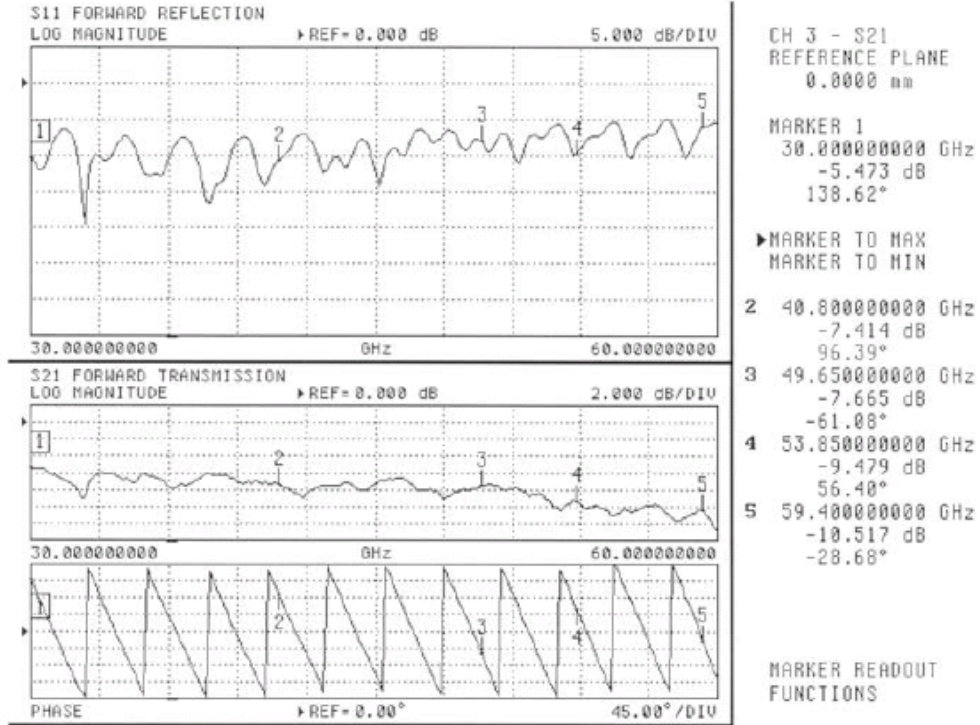
(d) 70 Volt



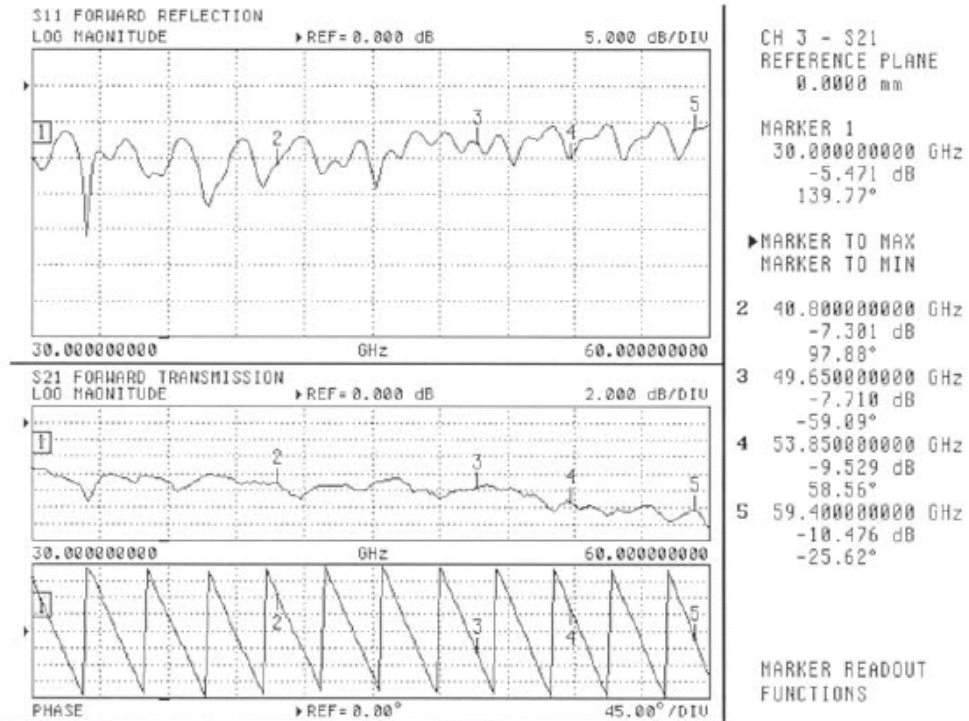
(e) 80 Volt



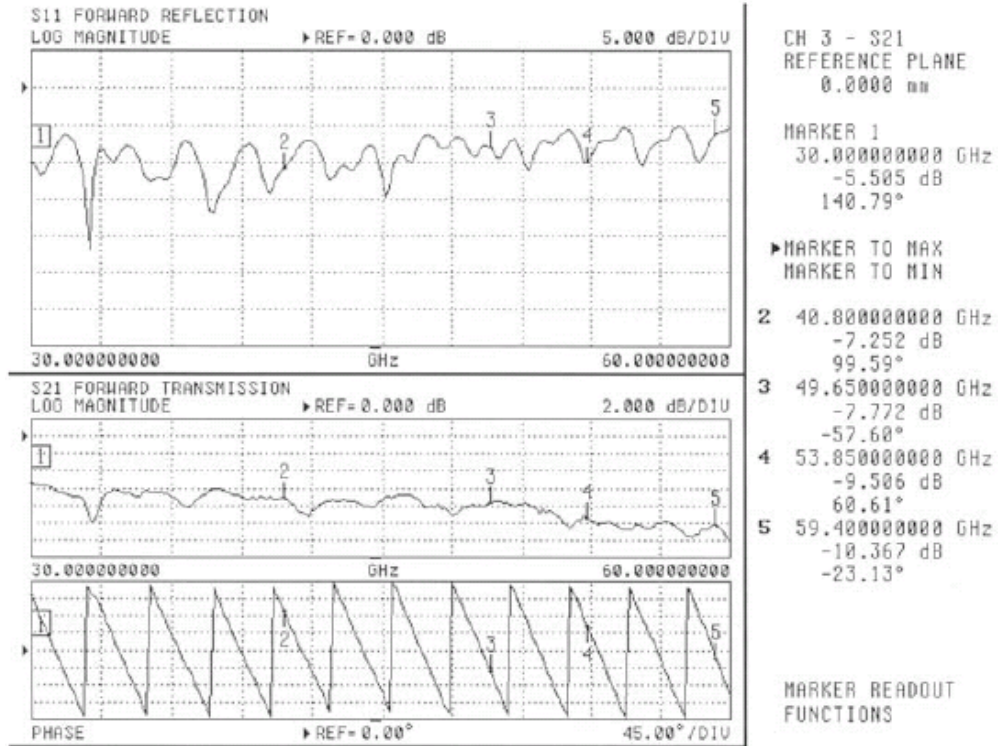
(f) 90 Volt



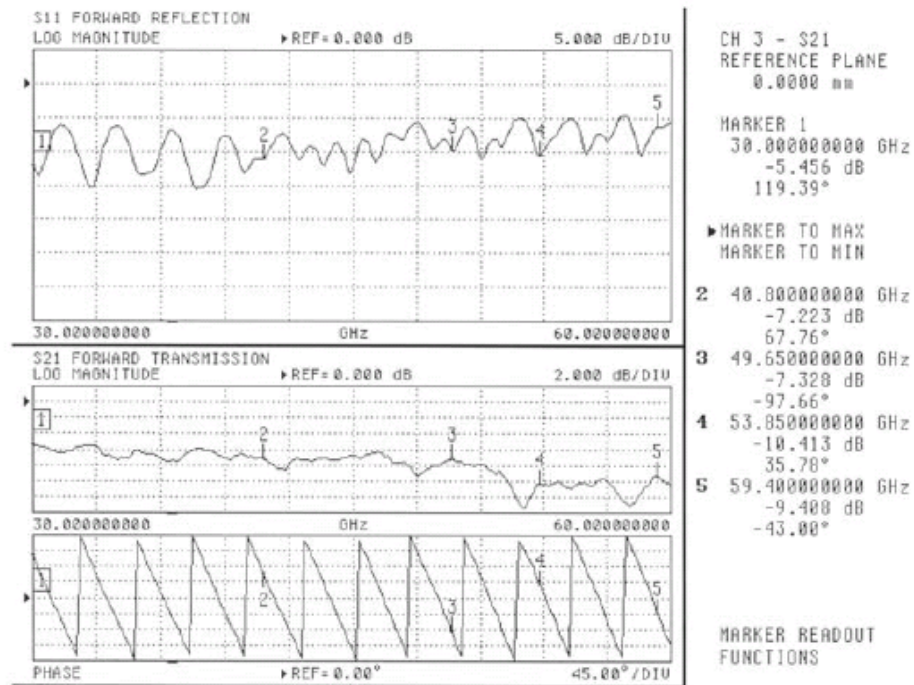
(g) 100 Volt



(h) 110 Volt



(i) 120 Volt



(j) Reversed to 0 Volt

Fig. E.3: Set2 - The measured return loss (S_{11}), insertion loss (S_{21}) and insertion phase (S_{21}) of the single membrane phase shifter with the electrostatic actuation at the electrode from (a) 0 V, (b) 30 V, (c) 40 V, (d) 50 V, (e) 60 V, (f) 70 V, (g) 80 V, (h) 90 V, (i) 100 V, (j) 110 V, (k) 120 v, and (l) Reversed 0 V cases.